

Naval Surface Warfare Center Carderock Division

West Bethesda, MD 20817-5700

NSWCCD-50-TR-2006/031 December 2006

Hydromechanics Department Report

Hydrodynamic Performance of a Dual-Slotted Circulation Control Wing of Low-Aspect Ratio

by

Martin J. Donnelly

J. Michael Cutbirth

Ernest O. Rogers

Stuart D. Jessup

Joel T. Park



Approved for public release. Distribution unlimited.

REPORT DOCUMENTATION PAGE			Form Approved OMB No. 0704-0188	
Public reporting burden for this collection of information is estimated to average 1 hour per response, including the time for reviewing instructions, searching existing data sources, gathering and maintaining the data needed, and completing and reviewing this collection of information. Send comments regarding this burden estimate or any other aspect of this collection of information, including suggestions for reducing this burden to Department of Defense, Washington Headquarters Services, Directorate for Information Operations and Reports (0704-0188), 1215 Jefferson Davis Highway, Suite 1204, Arlington, VA 22202-4302. Respondents should be aware that notwithstanding any other provision of law, no person shall be subject to any penalty for failing to comply with a collection of information if it does not display a currently valid OMB control number. PLEASE DO NOT RETURN YOUR FORM TO THE ABOVE ADDRESS.				
1. REPORT DATE (DD-MM-YYYY) 30-Dec-2006		2. REPORT TYPE Final		3. DATES COVERED (From - To) 1-Oct-2000 - 30-Sep-2002
4. TITLE AND SUBTITLE Hydrodynamic Performance of a Dual-Slotted Circulation Control Wing of Low-Aspect Ratio			5a. CONTRACT NUMBER 01C5S00009	
			5b. GRANT NUMBER	
			5c. PROGRAM ELEMENT NUMBER 0602121N	
6. AUTHOR(S) Martin J. Donnelly, J. Michael Cutbirth, Ernest O. Rogers, Stuart D. Jessup, and Joel T. Park			5d. PROJECT NUMBER 01-1-5400-131, 02-1-5400-141	
			5e. TASK NUMBER	
			5f. WORK UNIT NUMBER	
7. PERFORMING ORGANIZATION NAME(S) AND ADDRESS(ES) AND ADDRESS(ES) Naval Surface Warfare Center Carderock Division 9500 Macarthur Boulevard West Bethesda, MD 20817-5700 USA			8. PERFORMING ORGANIZATION REPORT NUMBER NSWCCD-50-TR-2006/031	
9. SPONSORING / MONITORING AGENCY NAME(S) AND ADDRESS(ES) Office of Naval Research (ONR) Attn: Dr. Ron Joslin 875 North Randolph Street Arlington, VA 22203-1995 USA			10. SPONSOR/MONITOR'S ACRONYM(S)	
			11. SPONSOR/MONITOR'S REPORT NUMBER(S)	
12. DISTRIBUTION / AVAILABILITY STATEMENT Approved for public release. Distribution unlimited.				
13. SUPPLEMENTARY NOTES				
14. ABSTRACT An extensive experimental effort was undertaken to document the performance of a low-aspect ratio hydrofoil with trailing edge blowing across a Coanda surface in a large water tunnel facility. This facility was the William B. Morgan Large Cavitation Channel in Memphis, TN. The hydrofoil model with a taper ratio of 0.76 was mounted through a load balance. A reflection plane provided for an effective aspect ratio of 2. The dual-slot configuration allowed for an investigation of thrust vectoring, and also presented an unexpected opportunity to offset the negative impact of excessive turning of the wall jet onto the underside of the foil. This report serves to document the experimental details of that effort for future experiments and document the types of data collected for validation of computational fluid dynamics (CFD) codes. The performance of the selected hydrofoil section shape is documented with six-component load measurements and detailed laser Doppler velocimetry measurements (LDV) taken in the wake of the foil.				
15. SUBJECT TERMS circulation control, low aspect ratio hydrofoil				
16. SECURITY CLASSIFICATION OF:			17. LIMITATION OF ABSTRACT	18. NUMBER OF PAGES
a. REPORT UNCLASSIFIED	b. ABSTRACT UNCLASSIFIED	c. THIS PAGE UNCLASSIFIED	SAR	0
				19a. NAME OF RESPONSIBLE PERSON Stuart D. Jessup
				19b. TELEPHONE NUMBER (include area code) 301-227-5080

This page intentionally left blank.

Contents

	<i>Page</i>
Nomenclature	vi
Greek	vii
Subscripts	vii
Abbreviations	viii
Abstract	1
Administrative Information	1
Acknowledgements	1
Introduction	2
History	2
Objectives	2
Experimental Apparatus	3
Water Tunnel	3
Model Design and Construction	3
Model Installation	4
Model Instrumentation	4
Slot Flow Measurement	4
Force and Moment Measurements	6
Pressure Measurements	6
Laser Doppler Velocimetry (LDV)	7
Velocity Measurement Arrangement	7
LDV System	7
Measurement Locations	8
Uncertainty Analysis	8
Experimental Results	11
Model Loads	11
Slots with No Flow	11
Upper Slot Flow	11
Lower Slot Flow	12
Second Slot Bleed	13

Wake Filling.....	13
LDV Results.....	14
Slots with No Flow	14
Wake Filling.....	15
Upper Slot Flow	17
Cavitation.....	20
Conclusions.....	21
References.....	69

Figures

	<i>Page</i>
Figure 1. CC Hydrofoil Drawing	22
Figure 2. Detail Drawing of Trailing Edge	23
Figure 3. Photograph of Brass Plate with Stainless Steel End-Plates and Screen.....	24
Figure 4. Close-Up View of Screen	24
Figure 5. Photograph of Assembled CC Hydrofoil Model without End-Plates	25
Figure 6. Cross-Sectional View of LCC Test Section Installation.....	26
Figure 7. Exploded View of CC Hydrofoil LCC Installation.....	26
Figure 8. Empty Test Section Velocity Contours for LCC	27
Figure 9. Turbulent Boundary Layer Growth in LCC Test Section.....	28
Figure 10. Photograph of CC Hydrofoil Installation in LCC Test Section from Trailing Edge View.....	29
Figure 11. Photograph of CC Hydrofoil with View from Trailing Edge	29
Figure 12. Griswold R2GH15 centrifugal pump.....	30
Figure 13. Reliance SP600 motor controller and power junction box	30
Figure 14. Inlet to the pump (Elbow#4) LCC Upstream Vertical Leg.....	31
Figure 15. Flow Measurement layout showing Hoffer turbine flowmeter.....	31
Figure 16. Photograph of External Installation in Test Section	32
Figure 17. Turbine Meter Calibration for Slot Flow	32
Figure 18. Uncertainty Estimates for Volumetric Flowrate of Turbine Meter	33
Figure 19. AMTI Force/Torque Cell Calibration.....	35
Figure 20. Pressure Transducer Calibrations for CC Foil Plenum Chamber	36
Figure 21. LDV Measurement Locations	37
Figure 22. Relative Uncertainty in LDV Calibration with Spinning Disk at 100- mm Radius	38
Figure 23. Relative Uncertainty in LDV Calibration for Varying Radial Distances	38
Figure 24. Residual Plot for Calibration of Axial Velocity	39
Figure 25. Force Coefficients with No Slot Flow	39
Figure 26. Force Coefficients with Upper Slot Flow at $\alpha = 0^\circ$	40
Figure 27. Force Coefficients with Upper Slot Flow at $\alpha = 0^\circ$ and 2 Re	40
Figure 28. Force Coefficients for Faired Slot and Modified Tip-Plate at $\alpha = 0^\circ$	41

Figure 29. Force Coefficients with Upper Slot Flow at $\alpha = -20^\circ$	41
Figure 30. Force Coefficients with Upper Slot Flow at $\alpha = -5^\circ$	42
Figure 31. Force Coefficients with Upper Slot Flow at $\alpha = +5^\circ$	42
Figure 32. Force Coefficients with Upper Slot Flow at $\alpha = +10^\circ$ with Repeat Run	43
Figure 33. Force Coefficients with Upper Slot Flow at $\alpha = +20^\circ$	43
Figure 34. Force Coefficients with Upper Slot Flow at $\alpha = +30^\circ$	44
Figure 35. Force Coefficients with Upper Slot Flow at $\alpha = +40^\circ$	44
Figure 36. Force Coefficients with Upper Slot Flow at $\alpha = +90^\circ$	45
Figure 37. Force Coefficients with Upper Slot Flow at Maximum Lift.....	45
Figure 38. Modified Tip-Plate as Trailing Edge Flow Fence.....	46
Figure 39. Force Coefficients with Lower Slot Flow at $\alpha = 0^\circ$	46
Figure 40. Force Coefficients with Lower Slot Flow at $\alpha = 0^\circ$ and 2 Re.....	47
Figure 41. Force Coefficients with Lower Slot Flow at $\alpha = +10^\circ$	47
Figure 42. Force Coefficients with Lower Slot Flow at $\alpha = +30^\circ$	48
Figure 43. Force Coefficients with Lower Slot Flow at $\alpha = +40^\circ$	48
Figure 44. Force Coefficients with Upper Slot Flow at $\alpha = 0^\circ$ with Wake Fill	49
Figure 45. Force Coefficients with Upper Slot Flow at $\alpha = 10^\circ$ with 2 Wake Fills.....	49
Figure 46. Force Coefficients with Upper Slot Flow, $\alpha = 10^\circ$, Wake Fill, and 2 Re	50
Figure 47. Force Coefficients with Upper Slot Flow at $\alpha = 20^\circ$ with Wake Fill	50
Figure 48. Force Coefficients with Upper Slot Flow at $\alpha = 30^\circ$ with Wake Fill	51
Figure 49. Drag Coefficient at $\alpha = 0^\circ$ with Equal Slot Flows	51
Figure 50. Spanwise Velocity Profile $x/c = -0.083$ Upstream of CCfoil.....	52
Figure 51. Wake Velocity Profiles with No Slot Flow and $Re = 2.2 \times 10^6$	52
Figure 52. Wake Velocity Profiles with No Slot Flow and $Re = 5.5 \times 10^6$	53
Figure 53. Wake Filling for “Zero Thrust” at $y/s = -0.5$ at $Re = 2.2 \times 10^6$	53
Figure 54. Axial Variation of Wake Profiles for “Positive Thrust” at $y/s = -0.25$	54
Figure 55. Wake Profiles for Various Slot Flows at $x/c = 1.083$ and $y/s = -0.5$	54
Figure 56. Spanwise Uniformity of Wake Profiles for Zero Thrust, $Re = 5.5 \times 10^6$	55
Figure 57. Spanwise Uniformity of Wake Profiles, $C_{\mu Tot} = 0.059$, $Re = 2.2 \times 10^6$	56
Figure 58. Velocity Contours at Various Spanwise Locations for $C_{\mu U} = 0.07$ and $C_{\mu L} = 0.00$ at $Re = 2.2 \times 10^6$	56
Figure 59. Relative Turbulence Contours Indicating Jet Location at various Spanwise Locations for $C_{\mu U} = 0.07$ and $C_{\mu L} = 0.00$ at $Re = 2.2 \times 10^6$	57
Figure 60. Velocity Contours at Various Spanwise Locations for $C_{\mu U} = 0.15$ and $C_{\mu L} = 0.0035$ at $Re = 2.1 \times 10^6$	57
Figure 61. Relative Turbulence Contours Indicating Jet Location at Various Spanwise Locations for $C_{\mu U} = 0.15$ and $C_{\mu L} = 0.0035$ at $Re = 2.1 \times 10^6$	58
Figure 62. Axial Velocity Contours for Various Slot Flows at $x/c = 1.083$ and Re $= 2.2 \times 10^6$	58
Figure 63. Vertical Velocity Contours for Various Slot Flows at $x/c = 1.083$ and $Re = 2.2 \times 10^6$	59
Figure 64. Relative Turbulence Levels at Various Axial Locations for $C_{\mu U} = 0.07$ and $C_{\mu L} = 0.00$ with $Re = 2.2 \times 10^6$	59
Figure 65. Velocity and Turbulence Contours at $x/c = 1.271$ for $C_{\mu U} = 0.07$ and $C_{\mu L} = 0.00$ with $Re = 2.2 \times 10^6$	60

Figure 66. Relative Turbulence Levels for Various Slot Flows at $x/c = 1.083$ and $Re = 2.2 \times 10^6$	60
Figure 67. Relative Turbulence Levels for Various Angles of Attack at $x/c = 1.083$ for $C_{\mu U} = 0.07$ and $C_{\mu L} = 0.00$ with $Re = 2.2 \times 10^6$	61
Figure 68. Vortex cavitation, tip and lightning vortex at 80% span	61
Figure 69. Cavitation on CCfoil, upper slot blowing, Coanda surface, tip vortex, and lightning vortex at 80% span shown.	62
Figure 70. Surface cavitation on Coanda Surface, close-up of the slot flow, inception behind slot lip face.	62
Figure 71. Surface Cavitation on Coanda Surface, lower slot blowing.	63
Figure 72. Lift response to cavitation development on the Coanda surface	63
Figure 73. Cavitation inception diagram at 0 degrees AOA	64
Figure 74. Impact of endplate on vortex cavitation inception.....	64

Tables

	<i>Page</i>
Table 1. Channel List for Data Acquisition System	65
Table 2. Completed Test Matrix of LDV Measurements	66
Table 3. Optical Parameters for CCfoil Tests	67
Table 4. Uncertainty Estimates of Elemental Variables	67
Table 5. Uncertainty Estimates of CCfoil Test Parameters	67
Table 6. Force Measurements Coincident with LDV Measurements.....	68

Nomenclature

c	Mean CCfoil Chord, 609.6 mm (24 inch)
C_D	Drag coefficient, $D/(qcs)$
C_L	Lift coefficient, $L/(qcs)$
C_m	Pitching moment coefficient, $M/(qc^2s)$
C_μ	Slot momentum coefficient, $(\rho QU_{jet})/(qcs)$
D	Drag force
D_{e-2}	Beam diameter of the LDV fiber optic probes
d_f	Fringe spacing within the LDV probe volume
d_{LDV}	Beam spacing of the LDV fiber optic probes
d_m	LDV probe volume diameter
f	Turbine meter rotational frequency
f_D	Doppler frequency measured by the LDV
f_L	Focal length of LDV fiber optic probes

K	Turbine meter factor
L	Lift force
l_m	LDV probe volume length
M	Pitching moment or expansion ratio of the LDV fiber optic probes
Q	Volumetric flowrate
p	Pressure
p_v	Vapor pressure of water
q	Dynamic pressure, $\rho(U_{up})^2/2$
Re	Reynolds number, cU_{up}/ν
r_s	Distance from the center of the spinning disk for LDV calibration
s	CCFoil span, 609.6 mm (24 inch)
U	Uncertainty
U_{up}	Tunnel reference velocity measured at inlet of test section
U_{jet}	Calculated CCFoil jet velocity
U_x, U_z	LDV measured axial and vertical velocity components
u_x', u_z'	RMS velocities of the axial and vertical velocity components
t_{95}	Inverse student t probability at the 95% confidence level
Tu	Relative turbulence level
V	Velocity, generic variable
x, y, z	Axial, transverse, and vertical coordinates

Greek

α	Angle of attack of CCFoil or angle between LDV beam pairs
λ	Wavelength of LDV beams
μ	Absolute viscosity
ν	Kinematic viscosity, μ/ρ
ρ	Density
σ_i	Cavitation index, $(p - p_v)/q$
σ_x	Standard deviation in x
ω	Rate of rotation of the spinning calibration disk

Subscripts

A	Type A uncertainty
B	Type B uncertainty
L	Lower slot
U	Upper Slot

Abbreviations

CCFoil	Circulation Control Hydrofoil
CCM	Central Command Module
LCC	Large Cavitation Channel
LDV	Laser Doppler Velocimetry

Abstract

An extensive experimental effort was undertaken to document the performance of a low-aspect ratio hydrofoil with trailing edge blowing across a Coanda surface in a large water tunnel facility. This facility was the William B. Morgan Large Cavitation Channel in Memphis, TN. The hydrofoil model with a taper ratio of 0.76 was mounted through a load balance. A reflection plane provided for an effective aspect ratio of 2. The dual-slot configuration allowed for an investigation of thrust vectoring, and also presented an unexpected opportunity to offset the negative impact of excessive turning of the wall jet onto the underside of the foil. This report serves to document the experimental details of that effort for future experiments and document the types of data collected for validation of computational fluid dynamics (CFD) codes. The performance of the selected hydrofoil section shape is documented with six-component load measurements and detailed laser Doppler velocimetry measurements (LDV) taken in the wake of the foil.

Administrative Information

The work described in this report was performed by the Propulsion and Fluid Systems Division (Code 54) of the Hydromechanics Department at the Naval Surface Warfare Center, Carderock Division (NSWCCD). The work was funded by the Office of Naval Research, Code 334 as part of the FY01 and FY02 6.2 Surface Ship Hull, Mechanical and Electrical Technology Program (Program Element 0602121N).

Acknowledgements

The author's would like to thank the LCC management and support staff for their assistance in the completion of this experimental effort, Mr. David Schwarzenberg and Mr. Fred Behnaz for their work in experimental design and fabrication of both the circulation control hydrofoil and the interface hardware, and Mr. David Burroughs for his work in setting up the experimental hardware and instrumentation and keeping the test running. The sponsoring agency was the Office of Naval Research under the supportive cognizance of Dr. P. Purtell, and Dr. R. Joslin. Their patience in the completion of this report has been greatly appreciated.

Introduction

An experimental investigation was conducted in a water tunnel on the performance a low-aspect ratio wing with circulation control (CC) via application of the Coanda effect. The CC hydrofoil is equipped with dual slots for tangential wall jets flowing over a circular tailing edge for bi-directional force generation. The cross-section is elliptical. The design is representative of control appendages for a submarine. The CC hydrofoil will provide significant lift at low speeds where conventional control surfaces will not function. The experiments were performed in the U. S. Navy William B. Morgan Large Cavitation Channel (LCC) in Memphis, TN. Some results were previously reported by Rogers and Donnelly [1]. The purpose of this report is documentation of the experimental details for future experiments and validation of computational fluid dynamics (CFD) codes.

History

Reattaching jet flows belong to a general class of flows usually named the Coanda effect after the Rumanian-born French inventor Henri-Marie Coanda. The Coanda effect was reported by earlier researchers such as T. Young in 1800 and O. Reynolds in 1870. The effect occurs in two-dimensions, for example, when a sufficiently long plate is brought near a plane parallel jet. As the plate approaches near the jet the velocity between the plate and jet increases. The jet will curve and attach to the plate. Consequently, the pressure drops due to the Bernoulli effect. The jet curves and attaches to the plate. The stability of this effect is maintained by a balance of the pressure in the trapped bubble and the centrifugal force in the curved jet. Additional details on the phenomenon and research prior to 1975 are summarized in Duvvuri and Park [2]. Subsequent research through 1983 is summarized in a bibliography by Englar and Applegate [3].

In the research prior to 1975, most of the theory on the Coanda effect concerned reattachment of plane jets to a flat plate. Duvvuri and Park [2] was one of the early attempts in the development of analytical model for reattachment to a curved surface. The present research concerns attachment of a tangential jet to a curved surface. Chang, et al. [4] have recently developed a CFD model of the flow for the CC hydrofoil described in this report. Although their model successfully describes most of the flow physics, the lift is under-predicted.

Objectives

The CC hydrofoil for these experiments is typical of control devices for underwater applications such as rudders, bow-planes, stern-planes, anti-roll fins, and sails. As a control device, the CC hydrofoil will provide relatively high lift at low speed where conventional control surfaces will not function. The primary objectives of these experiments were as follows:

1. Prediction of performance at low-aspect ratio
2. Cavitation properties of the trailing-edge Coanda wall jet
3. Attributes of dual slots, including wake filling.

Experimental Apparatus

Water Tunnel

These experiments were performed during August and September 2002 in the U. S. Navy William B. Morgan Large Cavitation Channel (LCC), world's largest water tunnel located in Memphis, TN. The tunnel walls are manufactured from 304 stainless steel. The test section is 13.1 m (43 ft) long at the test top opening with a 3 m (10 ft) square cross-section. The tunnel has a variable pressure control for cavitation studies with a pressure range of 0.03 to 4 atm (0.5 to 60 psia) at the test-section top. Its speed is highly stable between 0.5 to 18 m/s (1.6 and 59 m/s) with a long term velocity stability of ± 0.15 % at the 95 % confidence level. The longitudinal relative turbulence intensity in the test section is between 0.2 and 0.5 % depending on the speed. Additional details of the tunnel and its performance are described in Park, et al. [5], [6].

Model Design and Construction

The hydrofoil section for the model is an ellipse with a thickness to chord ratio, $t/c = 0.20$. The CCfoil was tapered with a leading edge sweep of 15° . The root chord was 689.4 mm (27.143 in) while the tip was 528.9 mm (20.823 in). The resulting average chord was then 609.2 mm (23.983 in). The span of the CCfoil is 609.6 mm (24.00 in) which results in an aspect ratio of 1.00 or with a reflective plane an effective aspect ratio of 2. Drawings of the wing are presented in Figure 1. In this figure, the root and tip sections have the same scale.

Details of the slot and trailing edge are shown in Figure 2. The slot is designed as a 2-dimensional converging nozzle for flow of a tangential wall-jet over a cylindrical surface. The average gap size is 0.0019c and is adjustable with 7 pairs of push-pull screws. The estimated uncertainty in gap height is 38 μm (0.0015 in.). Throughout the test, gap height remained constant. Gap expansion at the peak internal pressure of 2.3 atm (34 psig) was about 8 % as determined by dial gage, which compared favorably with structural analysis.

The CCfoil was fabricated in three sections: (1) Internal flow section manufactured from brass, (2) Leading edge section of anodized aluminum, and (3) Trailing edge section of stainless steel. The internal construction of the CCfoil with stainless endplates is shown in Figure 3. The view is from the root section of the wing with the leading edge to the viewer's right. The holes, 50.8 mm (2.000 in) in diameter, for the water flow to the upper and lower slots for the wall jet are evident in this photograph. These are the 2 holes also shown in the drawing of Figure 1b. The wood near the leading edge of the model is not part of the model. As the photograph indicates, the brass plate includes 5 airfoil sections for directing the flow internally. A stainless perforated plate with 30 % open area was added to the upstream side of the small airfoil section for the production of flow uniformity. The inlet velocity to the perforated plate was estimated to be 6 % of the slot exit velocity. Normally for avoidance of flow instability, the open area ratio for a screen should be greater than 50 % from Laws and Livesey [7]. From flow testing, the only effect on flow uniformity appears to be from the adjustment screws. Figure 4 is a close-up photograph of the screen.

A photograph of the assembled model with the end-plates removed is shown in Figure 5. Figure 5a is a view from the root section, while Figure 5b is a view from the trailing-edge and tip with the trailing-edge cover removed.

Model Installation

A drawing of the model installation in the LCC test section is presented in Figure 6 where the dimensions are in inches. This cross-sectional view of the test section is toward the exit of the test section. Figure 7 is a 3-dimensional exploded view of the various components added to the test section.

The velocity contours from Park, et al. [5] are shown overlaid in Figure 8 onto the test section drawing in Figure 6. In this case, the view is toward the test section entrance. As Figure 8a indicates, the wall stand-off plate or ground board is located outside the tunnel wall boundary layer so that the ground board also functions as a reflection plane. The stand-off distance for the ground board was determined by the measured boundary layer growth in test section from unpublished LDV (laser Doppler velocimeter) measurements by Park and Cutbirth¹ **Error! Reference source not found.** shown in Figure 9. The turbulent boundary thickness is presented as a Reynolds number based upon momentum thickness, Re_θ . The length Reynolds number, Re_x , is computed from the distance from the virtual origin, which is referenced to an upstream location from the center of window 2 in bay 1 of the LCC test section.

From the figure for the vertical velocity component, Figure 8b, large coherent structures are located near the sidewall of the tunnel. These structures predominantly retain size, magnitude, and location regardless of tunnel speed. The exception would be for the structure nearest the sidewall that is influenced slightly with increased thickness of the sidewall boundary layer. These structures within the empty test section may be of concern during evaluation of results for all LCC obtained data.

A photograph of the CCfoil and ground board installation is shown in Figure 10. The view is toward the test section entrance. A close-up of the installed CCfoil is presented in Figure 11 as seen from the trailing-edge. The external fixture with the angle of attack adjustment and plumbing for the slot flow is indicated in Figure 16.

Model Instrumentation

Data for the CCfoil model were collected with a National Instruments system, which consisted of a 16-bit data acquisition card and LabVIEW software. A total of 23 channels of data were collected. The data channels are summarized in Table 1. Included in this table is a list of the instrumentation by manufacturer, model number, serial number, measurement range, and estimated uncertainty of the measurement at the 95 % confidence limit by the Type B method per the ISO Uncertainty Guide [8]. Most the uncertainties in this table were determined from instrument calibration. Additional details are described in the following sections.

Slot Flow Measurement

Flow for the slots is provided by an electrically driven pump. The pump was a Griswold R2GH15 centrifugal pump with end suction, shown in Figure 12. Flow control was provided by a Reliance SP600 motor controller, shown in Figure 13. The inlet to the pump was connected to the entrance turning section (Elbow #4) at the main floor level, shown in Figure 14. The output of the pump was connected by a flexible hose to a 2-inch (50.8 mm) Turbine Meter by Hoffer

¹ Park, Joel T. and Cutbirth, J. Michael, 2001. Unpublished results.

Flow Controls located at the test platform near the external connection to the CCfoil. The piping just upstream of the turbine meter was a copper pipe with a length of 3.854 ft (23.125 D). An RTD, Omega RTD-NPT-72-E, was located downstream of the turbine meter at 24 in (12 D). The downstream end of the flowmeter was connected to a stainless steel 2-inch Y. The length of straight pipe between the turbine meter the Y was 20 in (10 D). This layout is shown in Figure 15. The ends of the Y were then connected to the CCfoil as indicated by the photograph in Figure 16.

The upstream piping is critical for the accuracy of the turbine meter. According to Baker [9], both velocity profile shape and swirl will adversely affect the accuracy of a turbine meter. Industry standards (API, ASME, and ISO) and manufacturer's specifications recommend installation of a tube bundle upstream of the turbine meter for the elimination of swirl. Hoffer Flow recommends an upstream meter tube with a length of 10 D, and a tube bundle located at 5 D upstream of the meter. Industry standards specify a tube bundle of 19 tubes with a length of 10 d, where d is the inside diameter of one of the tubes. Due to the long length of

The volumetric flowrate for a turbine meter is given by the following equation:

$$Q = f / K \quad (1)$$

where f is the frequency output of the meter (i. e. rotational rate) and K is the meter factor determined by meter calibration. From factory calibration, $K = 144.06 \pm 2.75$ pulses/gal ($\pm 1.91\%$) for the range of 5 to 275 gal/min. The calibration data are presented in Figure 17. This curve is typical for turbine meters where the meter factor rolls off at low flowrates. Improved uncertainty at low flowrates would require additional calibration points between 5 and 15 gpm and application of a non-linear curve. Hoffer Flow recommends a flowrate range of 15 to 275 gpm for this meter. In that case, $K = 144.49 \pm 0.65$ pulses/gal ($\pm 0.45\%$). For this test, the factory reported value of 144.06 pulses/gal was applied in the data processing. The uncertainty in the post processed data could be improved for flows over 15 gpm with a correction of the data by the meter factor with the lower uncertainty.

From Equation (1), the combined uncertainty in volumetric flowrate for the turbine meter is given by

$$U_Q = \sqrt{(U_f / K)^2 + (f U_K / K^2)^2} \quad (2a)$$

or the relative uncertainty is

$$U_Q / Q = \sqrt{(U_f / f)^2 + (U_K / K)^2} \quad (2b)$$

The frequency information for calculation of the flowrate was provided by a Hoffer Flow Controls Intelligent Transmitter Model HIT-1B. The rated accuracy is $\pm 0.02\%$ for a full-scale range or 3500 Hz or an uncertainty of ± 0.7 Hz. From this estimate and the meter-factor calibration uncertainty, the first term in Equation (2a) is constant while the second term in Equation (2b) is constant. The results for these two equations are plotted in Figure 18 for the meter range of 15 to 275 gpm at the lower uncertainty in meter factor. As the figures indicate, the uncertainty asymptotes to the uncertainty in the meter factor at $\pm 0.45\%$ at 275 gpm. At the lower flowrates, the uncertainty is dominated by the transmitter where the uncertainty is $\pm 1.99\%$ at 15 gpm. For the calibration factor from the factory applied in this test over the range of 5 to

275 gpm, the uncertainty at 5 gpm is $\pm 6.1\%$, but the uncertainty in flowrate approaches that of the meter factor of $\pm 1.91\%$ at 275 gpm.

For future tests, the uncertainty contribution from the frequency, f , can be essentially reduced to zero by counting pulses and measuring time. For example at the lowest flowrate of 5 gpm, the nominal frequency is 12 Hz. At this frequency, 1000 pulses could be counted in 83 s. With the assumption that the count could be off by one pulse, the uncertainty in frequency would then be $\pm 0.1\%$ of reading. At the maximum flowrate, the nominal frequency is 660 Hz for a collection time of 1.5 s. The pulse counting method could be implemented with a National Instruments counter card, and the pulse count gated by the time interval of sampling for the AD card.

Force and Moment Measurements

Model forces and moments were measured with a 6-component dynamometer from Advanced Technology, Inc. (AMTI). The unit was an MC5 series force/torque cell. The 6-components measured were drag (F_x), lift (F_y), side-force (F_z), rolling moment (M_x), yawing moment (M_y), and pitching moment (M_z). The device is cylindrical with the z-axis along the centerline. Prior to use the dynamometer was calibrated by Modern Machine and Tool of Newport News, Virginia.

The calibration results are summarized in Table 1, and the details for lift, drag, and pitching moment are presented in Figure 19. All 6-components of the AMTI dynamometer were calibrated in a single pass with a total of 168 calibration loads. Consequently, most of the measurements were at zero load and resulted from cross-talk from the component being loaded. The uncertainty estimate was computed as twice the standard deviation of the difference between the applied and measured loads for all 168 loads; consequently, the uncertainty is dominated by the values at zero applied load. Inclusion of the points from zero is probably reasonable since similar cross-talk likely exists at other load conditions.

Additionally under load conditions, the loads were increased incrementally and then decreased so that each load condition was repeated. For F_x (drag), this process was repeated so that the load was repeated 4 times as indicated in Figure 19a. Strain-gage type of load cells are well known for their hysteresis. Hysteresis is only evident in the pitching moment in Figure 19c. Per ASTM E 74-02 [10], the loading should be random. However, such loading may be cost prohibitive. The uncertainty results from an independent calibration laboratory are within the manufacturer's specification of an uncertainty of nominally $\pm 0.2\%$ full-scale.

Pressure Measurements

From Table 1, a total of 13 pressure transducers were employed for this test. The functions of these transducers were as follows:

- PSIA: Absolute pressure of the test section for cavitation computations
- PSID: Contraction section pressure differential for computation of test section velocity
- Upper Plenum Pressure: Pressure for computation of the upper jet exit velocity for four ranges of pressure, 5, 10, 25, and 100 psi.

- Lower Plenum Pressure: Pressure for computation of the lower jet exit velocity for four ranges of pressure, 5, 10, 25, and 100 psi.
- Kiel Probe: Kiel probe for measurement of feed system head pressure
- DP: Differential pressure measurement of mid-chord and mid-span pressure taps on the upper and lower surface of CCfoil for 2 ranges of pressure 5 and 10 psi.

The estimated uncertainties of these pressure measurements are summarized in Table 1.

The reference pressure for all pressure transducers was a Paroscientific Model 740-100A Portable Laboratory Standard, which has an uncertainty in pressure of ± 0.01 psi. The Type B uncertainty in Table 1 is the combined uncertainty of this reference and $2 \times \text{SEE}$ (standard error of estimate) from the calibration. As the table indicates, the uncertainty of the 5, 10, and 25 psi transducers are all essentially the same. Residual plots of a 5 psi and 25 psi transducers are shown in Figure 20 for comparison. The error bars in the figures are the uncertainty in reference pressure of 0.01 psi. The dashed line is the uncertainty in the linear curve fit from calibration theory. Calibration theory yields a slightly higher uncertainty than $2 \times \text{SEE}$. As the figures indicate, most of the uncertainty is from the linear curve fit. Additionally, the 25 psi transducer has a systematic variation where the uncertainty in the curve fit could be reduced with a second-order polynomial or some other non-linear curve fit.

From manufacturer's specifications, the transducers for the plenum measurements have ranges of 5, 10, 25, and 100 psi with nominal uncertainties of 0.005, 0.015, 0.038, and 0.15 psi, respectively, in comparison to the reference uncertainty of 0.01 psi. Clearly, the Viatran 10, 25, and 100 psi transducers meet or exceed manufacturer's specifications, but the Sensotec 5 psi transducer does not. However, the reference standard uncertainty is insufficient for calibration at the rated uncertainty by Sensotec. In summary, the 25 and 100 psi transducers were sufficient for measurement of the anticipated pressures in the CCfoil plenum chambers.

Laser Doppler Velocimetry (LDV)

Velocity Measurement Arrangement

The velocity downstream of the CCfoil was measured with a 2-component LDV. The wake velocity was measured through the downstream window indicated in Figure 21. The vertical and axial components of velocity were measured. The measurements for the LDV surveys were primarily performed at a constant freestream velocity of 3.05 m/s (10 ft/s). The tunnel velocity was monitored with a second LDV near the test section entrance. The tunnel pressure was maintained at 172.3 kPa (25 psia) at the vertical centerline of the model for all LDV models. Additional details of the LCC LDV system are described in Park, et al. [5]. The entire test matrix for the LDV portion of the CCfoil program is given in Table 2.

LDV System

The LDV system for the CCfoil test consisted of 3 Dantec BSA 57N11 signal processors, 2 fiber optic probes, Spectra Physics 6 Watt Argon-Ion lasers (models 2016 and 2017), a Dantec 3-D traverse with remote control, and Dantec Flow software. The probe for measurement of the wake velocity was a Dantec 112-mm probe with a 1600-mm lens, capable of two velocity components with wavelengths of 514.5 and 488 nm. The probe for tunnel velocity was a single component Dantec 85-mm probe with an 800-mm lens and operated at a wavelength of 476.5

nm. The traverse has a range (in air) of 1.2 m in the y and z directions and 1.3 m in the x direction where x is in the direction of flow, y is the transverse direction, and z is in the vertical direction. The stepper motors for the traversing system have a resolution of $\pm 5 \mu\text{m}$ (0.0002 in). The travel in air for the y -direction translates to 1.6 m travel in water from a nominal refractive index of 1.33. The optical parameters for the LDV fiber optic probes used in the CCfoil testing are provided in Table 3.

Silicon carbide particles with a mean diameter of approximately $3 \mu\text{m}$, were used to seed the flow for the LDV measurements. Measurements were taken via backscatter in random mode. The output variables included the mean and rms velocities in the axial, x , and vertical, z , directions. Because of the time constraints for the LDV surveys, sampling was forced to be a sample sizes of $N = 1500$ for the linear profiles and $N = 2500$ for the planar profiles. The sampling rate was dependent on the location of the measurement with typically slower data rates near the centerline of the test section and higher data rates near the ground board. Nominal sample times were on the order of 5 ~ 10 seconds.

Measurement Locations

The LDV measurements within the CCfoil test program can be separated into two categories: wake filling and single-sided lift augmentation. For the wake filling portion of the test program, vertical LDV surveys were performed at discrete axial ($x/c = 1.02, 1.083, 1.273, 3.20$) and transverse ($y/s = -0.25, -0.50, -0.75$) locations. For the single sided lift augmentation, both chordwise and spanwise measurement planes of LDV data were obtained. The spanwise planes were located at $x/c = 1.083, 1.150, 1.215$, and 1.273 , as depicted in Figure 21a. The chordwise planes consisted of planes located at $y/s = -0.2, -0.6, -0.8$, and -0.9 , as shown in Figure 21b.

Uncertainty Analysis

All of the LDV results presented be categorized as a velocity ratio, axial velocity measurement, or relative turbulence level. The independent variables associated with these parameters are provided in Table 4. In addition to these parameters, spatial coordinates are provided for each measurement point presented in this report to allow for evaluation of flow features. The uncertainties of these spatial coordinates are shown in Table 5 with the uncertainties of the test parameters.

Uncertainty estimates by the Type A method from the ISO Uncertainty Guide [8], defined by Equation (1), are computed only from a time series. The Type A uncertainty depicts the uncertainty that varies for each measurement within a given LDV survey's measurement grid. All other uncertainties are Type B. All uncertainties that are presented in this section are based on a 95% confidence level. The Type B uncertainty estimates for the velocity are conservative due to the use of manufacturer's specifications on the calibration device. In practice, the precision of the calibration device out-performs the manufacturer's specifications.

All of the transverse spatial coordinates given for the LDV data have been non-dimensioned with the CCfoil's span, 609.6 mm (24 in). The mean CCfoil chord, 609.6 mm (24 in), was used to non-dimension the vertical and axial reference locations of the measurements. Therefore, the total uncertainty of the spatial location of these measurements is a combination of the uncertainty of the local coordinate value and the uncertainty of the model's characteristic

lengths. The Type A and Type B uncertainties for the spatial location of the measurements are given in Table 5. The uncertainties in the CCfoil length characteristics are dictated by the measurement device.

The origin of the axial coordinate was determined by the LDV probe volume as it intersects with the trailing edge of the model at its root. The zero point was then defined by one chord length upstream of this intersection. From this method, the Type B uncertainty in the axial coordinate is $\frac{1}{2}$ of the probe volume diameter, as shown in Table 3. An additional Type B uncertainty is caused by the step-size of the stepper motor on the LDV traverse.

For the transverse coordinate, y , the Type B uncertainty is due to the uncertainty of the $y/z = 0.0$ measurement. This measurement was determined from the LDV probe volume as it crosses the ground board window insert and mainstream flow interface. The uncertainty of this method is based on the probe volume length, the length in which all four beams have portions of the beam intersecting, as shown in Table 3. An additional uncertainty is based on the step-size of the stepper motor, for the LDV traverse, adjusted for the refraction index of water.

As with the transverse coordinate, the uncertainty in the vertical direction is from the uncertainty of the origin. The z/c measurements were determined using the top/bottom of the acrylic windows as pseudo knife-edges in combination with the horizontal LDV beams. The arithmetic mean between the z/c measurements for the top and bottom of the window was designated as the z/c origin. The uncertainty is determined as $\frac{1}{2}$ the probe volume diameter. As with the axial measurement, an additional uncertainty is caused by the stepper motor on the LDV traverse.

The turbulent velocity fluctuation, u_x' , measurement is defined as the standard deviation of the mean velocity measurement, σ_x . The uncertainty analysis methods of Coleman and Steele [11] do not apply to rms and higher-order statistics. However, the uncertainty of the turbulence measurement is dominated by the uncertainty in finding the variance of a distribution with a finite sample size. From Equation (1), where t_{95} is the inverse student t at the 95% confidence limit and σ_x is the standard deviation in x , with a sample sizes of $N = 2500$ and 1500 , respectively, and a corresponding inverse student t of $t_{95} = 1.96$ for a very large sample size, the uncertainty is $U_x = 0.039\sigma_x$ and $U_x = 0.051\sigma_x$, respectively. LDV measurements have an inherent noise floor near which the turbulence level cannot be accurately measured. For the LCC LDV, this noise floor is between $u_x'/U_m = 0.005$ and $u_x'/U_m = 0.010$.

$$U_x = t_{95}\sigma_x / \sqrt{N} \quad (3)$$

The LDV velocity is calibrated directly with a spinning disk. The spinning disk/CompuMoter system incorporates a disk 9 inches (228.6 mm) in diameter and covered with 60-grit emery paper. A precision blind hole is located at the center of the disk with a diameter of 0.040 inch (1.02 mm). The disk is driven by a CompuMotor Model SM233BE-NTQN motor with a CompuMotor TQ10X Servo-Controller. The maximum velocity is rated at 200 rps, but typically the unit is operated at a maximum of 30 rps. The manufacturer's stated accuracy is ± 0.04 rps.

The magnitude of the velocity on the rotating disk is given by Equation (4), where V is a generic velocity in m/s, r_s is the distance from the center of the disk, in meters, and ω is the rotational rate of the disk in revolutions per second, rps.

$$V = 2\pi \cdot r_s \cdot \omega \quad (4)$$

The uncertainty estimates were performed in accordance with the methods of Coleman and Steele [11] and the ISO Uncertainty Guide [8]. The relative uncertainty in V is then given by Equation (5), where U_x is the uncertainty in x at the 95% confidence level.

$$U_V / V = \sqrt{(U_r / r_s)^2 + (U_\omega / \omega)^2} \quad (5)$$

The major contributing factor for the uncertainty in the radial distance, r_s , is assumed to be in the location of the center of the disk. Repeated measurements were taken in centering the LDV probe volume in the machined hole at the center of the disk. For the combined uncertainty, the student t is applied as the coverage factor rather than 2 as in the ISO Uncertainty Guide [8]. Thus, the uncertainty in the mean value of x and z for N measurements is provided in Equation (3) where t_{95} is the inverse student t at the 95% confidence limit and σ_x is the standard deviation in x .

The relative uncertainty in velocity from rotational speed decreases with increasing velocity. That is at the lower speed, uncertainty in rotational speed is the dominant term while at the higher speed the contribution in the uncertainty of r_s becomes more important. A typical result for the relative uncertainty in axial velocity for a radius of 100 mm is presented in Figure 22. The contribution of r_s in the uncertainty can be reduced by using a radius of 50 mm, due to the increased rotational rate needed for a given velocity. Current practice uses a maximum rotational rate for the spinning disk of 30 rps. Therefore for higher velocities, a radius of 100 mm is necessary, while a radius of 50 mm is used to decrease the uncertainties for the lower velocities. The result of this practice is shown by the total bias error for the LDV calibration in Figure 23.

The estimated uncertainty during calibration consists of three elements as indicated in Figure 23: the rotational speed, position, and noise from the LDV. The uncertainty in velocity from rotational speed and position was computed from Equation (3). The estimates from rotational speed and position were evaluated by Type B methods via the ISO Uncertainty Guide [8], and contribute to the bias error for the velocity, V . The LDV noise is a third contribution, which was computed by Type A evaluation, and contributes to the precision error of the velocity, V . In this case, Equation (1) was applied.

The total uncertainty of the velocity calibration, shown in Table 5, includes the uncertainty from both the Type A and Type B methods in the measurement of the mean velocity. The Type A uncertainty of the velocity measurement is attributed to the local velocity component fluctuations (turbulence intensity) and sample size. Thus for the local axial and vertical velocity, the standard deviation for this measurement is applied to Equation (1) with sample size variation of 1500 to 2500 samples. The higher values of the uncertainty by Type A for the velocity ratios illustrated in Table 5 correspond to the large levels of fluctuating velocity within the CCfoil jet flow. Outside of the jet flow, the uncertainty of the velocity ratio is typified by the lower end of the uncertainty range.

For the model reference velocity, a fixed sample size of $N = 1000$ and nominal standard deviation of $\sigma_m = 0.01U_m$ were applied in the Type A estimate. For the non-dimensional velocities, a time averaged model reference velocity was employed. Therefore, the uncertainty of the non-dimensional velocity includes the total uncertainty of the model reference velocity

and the local velocity component. The Type A uncertainty for the non-dimensional velocity is comprised solely of the Type A uncertainty of the local velocity component.

A summary of the uncertainties for the independent variables and test parameters are given in Table 4 and Table 5, respectively. A typical calibration residual plot is given in Figure 24. The error bars are from the uncertainty in velocity from the spinning disk, while the dashed line is from the uncertainty in the linear curve fit from the calibration theory [12], [13]. A full description of the calibration technique and the uncertainty calculation for the velocity measurements is provided by Park, et al. [5].

Experimental Results

Model Loads

Slots with No Flow

For these tests, data were acquired over a range of angle of attack with no flow through either slot in order to document the baseline performance of the hydrofoil with no lift augmentation. As these spots were taken at the start of each configuration, they do not have a single associated Run #. Traditional force coefficient curves were then produced from the various runs at the no flow condition. The results from the consolidation of these runs are shown in Figure 25 as a function of the angle of attack. As the figure indicates, the lift curve slope is linear over the range of $\pm 20^\circ$ with a value of 0.0462 per degree. In another test, the angle of attack was varied in the near stall region. The maximum lift coefficient was measured as 1.20 at 31.5° . Stall and loss of lift occur for angles of 27.5° and greater. The maximum lift just before stall was 1.04 at 26.5° .

The nominal chord Reynolds number for most of the tests was 2.1×10^6 . The tunnel speed was set at a fixed pump shaft speed with nominal velocity of 3.05 m/s (10 ft/s). Small variations in Reynolds number occurred due to changes in the water temperature. Additionally, a systematic drop in tunnel velocity occurred at high slot flows with a maximum decrease of 0.1 m/s (0.3 ft/s) or 3 %.

Upper Slot Flow

Force data were acquired for 8 angles and flow through the upper and lower slots at the following angles: -20° , -5° , 0° , $+5^\circ$, $+10^\circ$, $+20^\circ$, $+30^\circ$, $+40^\circ$, and $+90^\circ$. The force coefficient results are shown in Figure 26 through Figure 37 for upper slot flow. At $C_\mu = 0.17$, the lift coefficient exhibited hysteresis. As the flow through the slot is increased, the lift coefficient attains a maximum. After lift is lost, the lift coefficient maintains almost a constant value as the flow is decreased until lift is recovered as indicated in Figure 26 for zero degrees angle of attack. This effect was attributed to excessive turning of the wall jet onto the lower surface generating a reduced pressure on the underside of the model. This effect has been referred to as “trailing edge pressure drawdown.”

As Figure 26 indicates, the data were quite reproducible per ISO definition [8]. Run 10 was conducted near the beginning of the test sequence while Run 44 occurred near the end of the test eight days later. A total of four runs, Runs 10, 14, 43, and 44, were conducted at the same test conditions with similar results.

The influence of a higher flow velocity was also examined. Data at a second Reynolds number of 3.1×10^6 were collected, and the results are presented in Figure 27. Again the reproducibility of the results is quite good. The results are also a validation of the proper non-dimensional representation of the data.

The effect of minor geometric changes was also evaluated with the results in Figure 28 relative to the normal test configuration in Figure 26. The influence of the open slot was checked by fairing the lower slot with aluminum tape for Run 34. Over most of the slot flow range, the results are virtually identical up to a momentum coefficient of 0.125 where the “trailing edge pressure drawdown” phenomenon is encountered. In this region, the lift coefficient has a lower value than for the previous tests and does not follow the higher values with increasing flow; however, the pitching moment coefficient values are essentially the same throughout the slot flow range. This fairing of the lower slot reduces the resistance of the jet to turning onto the underside of the model exacerbating the loss of lift at earlier flow coefficients.

The most dramatic change in lift coefficient occurred with a modified tip-plate as a trailing edge flow fence shown in Figure 38 relative to originally designed tip-plate. The lift coefficient increased significantly from a maximum of 1.83 to 2.07 or 13 % increase in Figure 28. Additionally, the modified tip plate suppresses the turning of the jet onto the underside of the foil so that no lift drop-off is observed for the higher flow rates.. Slight improvement in maximum lift was also observed at 20° in Figure 33. In this case, maximum lift coefficient increased from 2.38 to 2.46 or 3.6 %. However, loss of lift does occur due to the “trailing edge pressure drawdown” at a momentum coefficient of 0.13.

A composite of all of the maximum lift coefficient data for upper slot flow is shown in Figure 37 as a function of angle of attack. The momentum coefficient for these results is nearly constant with a value of 0.15. Throughout the range of angles, the lift coefficient is larger than the maximum lift coefficient at stall without slot flow with the exception of -20° where the coefficient is only slightly lower at 0.92. The maximum lift coefficient for all angles occurred at 20° with a value of 2.38, which is about twice the maximum lift without slot flow. The lift curve is quite linear over the angle of attack range between -20° and $+10^\circ$, this linear fit is shown in Figure 37 as a dashed red line, where lift curve slope is 0.043, which is slightly lower than that without slot flow. The lift curve linear range without flow is shown in the figure for reference.

Lower Slot Flow

The symmetry and repeatability of the data are also indicated by flow through the lower slot. For demonstration in the symmetry of the data, the negative values of the lift and pitching moment coefficients are presented in the figures for the lower slot flow. A comparison of the data at 0° is shown in Figure 39. The agreement between the lift and pitching moments is very good. However, some difference exists in the drag coefficient. The cause is unknown. Similar results are observed for the other cases of symmetry in Figure 29 and Figure 33 for $+20^\circ$ and -20° and Figure 30 and Figure 31 for $+5^\circ$ and -5° .

A modest improvement in lift was also observed with lower slot flow at $+20^\circ$ for the modified tip-plate in Figure 29. In this case, the maximum negative lift coefficient increased from 0.98 to 1.04 or 5.8%.

The effect of higher velocity on the force coefficients at 0° are shown in Figure 40. Again the agreement at two flow rates in the lower slot is very good. Results of lower slot flow for $+10^\circ$, $+30^\circ$, and $+40^\circ$ are presented in Figure 41, Figure 42, and Figure 43, respectively.

Second Slot Bleed

Some additional benefit in lift performance is obtained for upper slot flow with flow at the lower slot of a few percent. It was determined that the “trailing edge pressure drawdown” effect could be offset by bleeding flow through the non-blown slot. The amount of flow required from the non-blown slot to force separation of the jet from the upper slot was determined to be less than 5% of the total flow rate into the model. This counter-flow would cause the upper slot flow jet to lift off earlier not allowing it to penetrate to the underside of the model. The effect on the force coefficients is shown in Figure 44 through Figure 48. The flowrate in these figures is referenced to the upper slot. In general, the lift coefficient increases with increasing flow without stall. At 0° angle of attack in Figure 44, the maximum lift coefficient increases from 1.81 at stall to 1.94 or an increase in lift of 7 % with a lower slot flow of 1.4 % of the upper slot flow. The average lower slot flow for the data in the figure is 1.6 %. For reference, the data without lower slot flow are included from Figure 26.

Similar results are presented in Figure 45 and Figure 46 for 10° . In Figure 45, the effect of two lower slot flow rates is compared to the case with no lower slot flow at the same Reynolds number. For reference, the case for no lower slot flow is included from Figure 32. For no lower slot flow, the results are very reproducible for data that were taken nine days apart. The maximum lift coefficient for upper slot flow was increased from 2.18 to 2.16 or 20 % with a lower slot flow of 4.4 %.

In Figure 46, the effect of lower slot flow is presented for similar flow rates at two Reynolds numbers. In Run 52, the Reynolds number is about half that of Runs 12 and 53. At the lower Reynolds number, the maximum lift coefficient attained was 3.00 at a lower slot flow rate of 4.8 % in comparison to 2.18 without lower slot flow or an increase of 37 %. The good agreement in the data the two different Reynolds number is also an indication of proper non-dimensional scaling of the data.

The results for wake filling at 20° angle of attack are presented in Figure 47. For reference, the data with no lower slot flow are included from Figure 33. Again the data are very reproducible, and the lift coefficient is increased from 2.38 to 2.66 or 12 % with a lower slot flow of 4.2 %.

At 30° angle of attack, no additional benefit occurred with the addition of lower slot flow of 5.2 % over the range of the test. However, the data does indicate excellent reproducibility of data that were taken 7 days apart. The data for no lower slot flow is included from Figure 34.

Wake Filling

The effect of equal flow rates from the two slots is presented in Figure 49. In this case, high flow rates from the two slots produces thrust or a negative drag coefficient. The thrust linearly increases with flow. Wake filling results taken during the LDV measurements discussed in the next section are included in this figure. Nominally, zero drag was set at an upper slot momentum coefficient of 0.0093 with a measured drag coefficient of 0.00036 at a chord

Reynolds number of 5.27×10^6 . The drag coefficient at no flow is 0.017 to 0.018 at a Reynolds number of 2.2×10^6 .

LDV Results

Slots with No Flow

The baseline condition for the LDV measurements is defined as no flow, $C_{\mu U} = 0.0$ and $C_{\mu L} = 0.0$, with an angle of attack of $\alpha = 0^\circ$. The force coefficients associated with all of the LDV measurements are summarized in Table 6. The uncertainty in the table for the measurements is the Type A uncertainty as computed from the standard deviation from repeat runs. The inverse student t at the 95 % confidence level is applied in the expanded uncertainty. The N in the table is the number of repeat runs.

Figure 50 presents the spanwise velocity profiles immediately upstream of the CCfoil representing the inflow into the test region. The profiles encompass a region from the root, $y/s = 0.0$, to the tip, $y/s = -1.0$, of the CCfoil and have been non-dimensionalized with the upstream tunnel velocity, U_{up} , located at $x/c = -8.864$. From the axial velocity and relative turbulence profiles, the boundary layer thickness of the ground board is approximately $y/s = -0.04$. The other important aspect of the upstream profiles is the influence of the 15° swept angle of the CCfoil. The potential flow caused by the closer proximity of the CCfoil near the root, for the $z/c = 0.0$ profile, results in a velocity gradient of the axial velocity in the transverse coordinate, dU_x/dy . This velocity gradient is reduced as the location of the profile is lowered by $z/c = 0.246$.

Figure 51 and Figure 52 present the wake profiles at various spanwise locations for the baseline flow condition at $Re = 2.2 \times 10^6$ ($U_{up} = 3.04 \text{ m/s}$ or 10 ft/s) and $Re = 5.5 \times 10^6$ ($U_{up} = 7.35 \text{ m/s}$ or 24 ft/s), respectively. Figure 51 indicates good uniformity for the three span locations, $y/s = -0.25$, -0.5 , and -0.75 , for an upstream velocity condition of $U_{up} = 3.04 \text{ m/s}$. A wake deficit between 70% and 80% is observed at an axial location of $x/c = 1.083$ (0.083c downstream of the trailing edge of the CCfoil). The relative turbulence level in the axial coordinate is typical of a wake profile behind a blunt body with a double peak representing the shear layers between the mainstream flow and the wake behind the body. The maximum level of turbulence is 24% in the axial direction and 30% in the vertical direction. These aspects of the wake flow have diminished to 5% wake deficit and 5~6% turbulence level by two chord lengths downstream of the trailing edge ($x/c = 3.20$). The average axial velocity at $x/c = 3.2$ is approximately $1.05U_{up}$ as opposed to the freestream value of $1.02U_{up}$ at $x/c = 1.083$. This 3% increase is caused by the favorable axial pressure gradient within the LCC test section due to a constant cross-section and boundary layer growth. The potential flow of the CCfoil dominates the vertical velocity component at $x/c = 1.083$, which results in a symmetrical profile about $U_z = 0.0$ and $z/c = 0.0$. However, an average downward flow is noticeable at $x/c = 3.2$. This downward flow, $U_z/U_{up} = -0.03$, may be a function of the tunnel, CCfoil, or an influence of the flow downstream of the ground board and its corresponding supports.

In contrast to the similarity shown for $U_{up} = 3.04 \text{ m/s}$ between the various span locations, the velocity profile for the $y/s = -0.25$ position is significantly altered from the $y/s = -0.5$ and $y/s = -0.75$ profiles for the $U_{up} = 7.35 \text{ m/s}$ inlet condition. The axial velocity profile for the $y/s = -0.25$ location indicates reverse flow at an axial location of $x/c = 1.083$. This reverse flow is typical of a separated flow condition about the hydrofoil. The occurrence only at $y/s = -0.25$ at an inlet condition of $U_{up} = 7.35$ is due to the increased chord length at the root as compared to

the tip. By an axial position of $x/c = 3.20$, the flow has become similar for all three axial positions.

These two inlet conditions, $Re = 2.2 \times 10^6$ ($U_{up} = 3.04$ m/s) and $Re = 5.5 \times 10^6$ ($U_{up} = 7.35$ m/s), represent the inlet conditions of all of the LDV surveys. Additionally, the force measurements reported in the previous sections were performed at $Re = 2.2 \times 10^6$. Furthermore for the single-sided slot flow, all of the LDV surveys used the inlet condition of $U_{up} = 3.04$ m/s. The following sections detail the LDV results for the wake filling experiments, consisting of profiles in the vertical, z/c , direction at various y/s and x/c positions, and upper slot flow experiments, planar profiles oriented in both the x-z and y-z planes.

Wake Filling

The wake filling experiments are defined by flows from both the upper and lower slots. The purpose was to minimize flow disturbances and the wake deficit with corresponding flow features behind a hydrofoil. Practical need for wake filling would be for reduction of the wake effects from appendages upstream on the propulsor. For these results, the flow is defined as the total amount of the flow from the slots with the flow from each slot as half of the total for the equal flow case. These flow conditions are the total amount of flow within each slot over the entire span. The local flow conditions between the upper and lower jets may not be equal. The resulting force coefficients are summarized in Table 6. The wake filling case where the lower slot flow is a few percent of the upper slot flow are described in the next section on upper slot flow.

Figure 53 presents the wake profile, axial mean and fluctuating velocities, for the baseline and “Zero Thrust” conditions at axial locations of $x/c = 1.083$ and $x/c = 3.20$. The “Zero Thrust” condition is defined by the amount of flow necessary for the thrust from the slotted jets to balance the drag about the CCfoil. The amount of flow for this condition is dependent on the inlet velocity. For an inlet condition of $U_{up} = 3.04$, the necessary flow is approximately $C_{\mu Tot} = 0.02$. From the figure, the wake deficit at $y/s = -0.5$ has been reduced from 80% to 30% with the jet flow at $x/c = 1.083$. By two chord lengths downstream of the trailing edge, $x/c = 3.20$, the wake deficit has been reduced from 5% to a negligible effect. The relative turbulence has been reduced from 25% to 10% at $x/c = 1.083$ and from 7% to 3% at $x/c = 3.20$.

While the “Zero Thrust” condition adequately filled the wake by two chord lengths downstream of the CCfoil a 30% wake deficit still exists at $x/c = 1.083$. Therefore, a “Positive Thrust” condition was tested with a flow condition of $C_{\mu Tot} = 0.059$ at $U_{up} = 3.04$. The results for this condition are presented in Figure 54 for the mean and fluctuating axial velocity at axial locations $x/c = 1.020$, 1.083 , and 1.271 .

For this condition the ratio of the slotted jet to the upstream velocity is $U_{jet}/U_{up} = 2.8$. The width of this high velocity jet is just ~10% of the entire width of the wake behind the CCfoil. This results in a superimposed “free” jet with the baseline wake condition immediately downstream of the CCfoil, $x/c = 1.02$. This jet is quickly diffused with the wake flow, such that the maximum deficit at $x/c = 1.083$ is 20%. This is compared to 80% for the baseline condition and 30% for the “Zero Thrust” condition. However, a jet flow is still in existence by $x/c = 1.271$ (at which point no velocity deficit compared to freestream flow is apparent). At two chord lengths downstream the axial velocity profile is similar to the “Zero Thrust” condition. The relative turbulence levels for this condition are similar to the baseline conditions.

The comparison between the two thrust conditions and the baseline is better shown in Figure 55. This figure presents the axial and vertical mean and fluctuating velocity profiles for the two baseline conditions as well as the “Zero Thrust” and “Positive Thrust” conditions at $x/c = 1.083$. The axial velocity profiles are similar for all conditions outside of the slotted jet flow created by the CCfoil. Within the jet region the differences are as described above. The relative turbulence in the axial direction is dependent on the shear layer between the mainstream flow and jet/wake behind the CCfoil. Therefore, the similarity between the mainstream flow and baseline wake with the mainstream flow and jet magnitude for the “Positive Thrust” condition results in similar axial turbulence levels. The reduction of the velocity gradient within the “Zero Thrust” flow results in the lower axial turbulence levels noted in Figure 53.

The vertical velocity component for the three flow conditions is also shown in Figure 55. The magnitude of the vertical component of the velocity has been reduced for the “Positive Thrust” condition. This is expected as the mainstream flow is not dispersing into a velocity defect for the “Positive Thrust” condition as much as the baseline condition. This reduction in the velocity gradient results in a lower relative turbulence in the vertical direction for the “Positive Thrust” condition. A similar profile is seen for the “Zero Thrust” condition. However, an overall shift of the profile exists such that the average vertical velocity is slightly negative. This corresponds to the slight shift of the axial velocity profile from the $z/c = 0$ centerline of the CCfoil. The cause of this shift is probably due to a slight difference in flow conditions between the lower and upper jets at this spanwise location.

This slight shift in the wake profile from the vertical centerline at $y/s = -0.5$ for the “Zero Thrust” condition suggests a lack of uniformity about the span of the CCfoil. Figure 56 and Figure 57 address the issue of similarity between the various spanwise locations for the “Zero Thrust” and “Positive Thrust” conditions, respectively. Figure 56 presents the velocity profiles for the “Zero Thrust” at $x/c = 1.083$ and $x/c = 3.20$ and spanwise locations of $y/s = -0.25, -0.5$, and -0.75 . The shift of the wake profile from the centerline is not apparent for the $y/s = -0.25$ or $y/s = -0.75$ positions. However, deviations of the magnitude of the wake deficit of 10% occur between the spanwise locations. These deviations have become negligible by $x/c = 3.2$. The one exception is a 5% deviation in the $y/s = -0.25$ location at a location of $z/c = -0.12$ which may be caused by the support structure of the ground board.

Figure 56 indicates that the wake flow has a significant vertical component and local deviations even at $x/c = 3.2$. A $0.1U_{up}$ change in the vertical velocity is noticeable over the velocity profile. This is compared to the baseline condition presented in Figure 51 and Figure 52 that indicated a slight downward flow of $0.03U_{up}$ with local deviations from the averaged downward flow of $\pm 1\%$. The $0.1U_{up}$ variation in the vertical velocity is a reduction from the $0.5U_{up}$ variation at $x/c = 1.083$.

The spanwise variations in the wake velocity profiles for the “Positive Thrust” condition at $x/c = 3.20$ are given in Figure 57. The LCC side wall window allows the expanded z/c range for the $x/c = 3.2$ location in comparison to the previous figures, which has a smaller visual aperture for the window inserts in the ground board and CCfoil side wall insert from the photographs in Figure 10 and Figure 11. Also, only the $y/s = -0.5$ location is included for the baseline condition with the exception of the axial mean velocity. This is for clarity within the figures. For the baseline condition, the variation between spanwise locations is small, and the $y/s = -0.5$ location is assumed to be typical for the baseline condition.

For the “Positive Thrust” condition, the $y/s = -0.25$ and $y/s = -0.75$ are similar for the axial mean velocity, and both depict wake deficits of 2% while the variation within $y/s = -0.5$ profile is less than the uncertainty of the measurement. Furthermore, the $y/s = -0.25$ and $y/s = -0.75$ profiles are similar in appearance for the vertical velocity component although the $y/s = -0.25$ profile is greater in magnitude. Both of the profiles contain regions of downward flow with respect to the baseline condition. These profiles differ from the $y/s = -0.5$ profile, which is similar to the baseline condition. These variations are probably caused by slight differences in the local flow conditions between the upper and lower slots about the span. While noticeable differences in the relative turbulence are apparent between the various span locations and the baseline, the maximum deviations between all of the profiles are within 1-2%.

Upper Slot Flow

Although the section is entitled single sided flow, it may be better presented as lift augmentation. These are the LDV results during the phase of the CCfoil experiments that evaluated the effects of flow from the trailing edge of a low aspect ratio hydrofoil on augmentation of lift. For all of the LDV results, the upper slot is used as the sole or primary jet. For the “assisted lift” condition, $C_{\mu U} = 0.15$ and $C_{\mu L} = 0.0035$ or $C_{\mu L}/C_{\mu U} = 2.3 \%$, a small flow from the lower jet is used to prevent excessive turning of the wall jet enabling significantly higher lift augmentation as previously shown in Figure 44 through Figure 46. The four conditions tested are summarized by Table 2 and the related force coefficient data in Table 6 and consists of the following: “Slight Flow”, “Moderate Flow”, “Maximum Flow”, and “Assisted Lift”. The “Slight Flow” condition, $C_{\mu U} = 0.07$ and $C_{\mu L} = 0.0$, is within the region in which the no discernable benefit is observed with the use of dual jets. The “Moderate Flow” condition, $C_{\mu U} = 0.13$ and $C_{\mu L} = 0.0$, is representative of the flow value in which the “trailing edge pressure drawdown” begins to influence the lift augmentation for this symmetrical design. The “Maximum Flow” condition, $C_{\mu U} = 0.18$ and $C_{\mu L} = 0.0$, is representative of a flow value beyond the transition phase of the lift breakdown region. These labels are not indicative of all possible flow conditions, but solely used to differentiate the various LDV surveys. For simplicity, these labels will be used henceforth to describe the various flow conditions. The corresponding force coefficient data with upper slot flow only are shown in Figure 26, Figure 32, and Figure 33 for $\alpha = 0^\circ$, 10° , and 20° , respectively.

Figure 58 presents the velocity contours with streamlines for the $y/s = -0.2$, -0.6 , -0.8 , and -0.9 spanwise locations for the “Slight Flow” condition, $C_{\mu U} = 0.07$ and $C_{\mu L} = 0.00$. The areas within the measurement region lacking data are caused by the blockage of LDV beams, for the area just downstream of the CCfoil, or the blockage of the traverse by the CCfoil support structure for the area between $-0.39 < z/c < -0.17$ and $x/c < 1.02$. The overall measurement region is bordered by the window edge on the bottom, top, and downstream edges and by the CCfoil support structure for the upstream edge. For these measurements, the LDV probe head has a downward tilt of 3° above the CCfoil and downstream of the CCfoil and an upward tilt of 3° below the CCfoil. This downward tilt for the majority of the profile results in the shift of the measurement region as LDV is traversed from near the root, $y/s = -0.2$, towards the tip, $y/s = -0.9$. The velocity contours shown in Figure 58 are a combination of U_x and U_z , as U_y is not measured. The span positions were chosen as near the root, near the center-span, and near the tip. An addition span location, $y/s = -0.8$, was chosen due to the identification of a three-dimensional flow structure at this location during the cavitation tests.

The calculated jet velocity for the “Slight Flow” condition is $U_{jet}/U_{\infty} = 4.3$ for the mean slot width. As shown in Figure 58 with maximum local velocities of $U_{jet}/U_{up} < 3.0$, the jet becomes quickly dispersed as it travels around the Coanda surface and turned downstream. The jet becomes further dispersed downstream as the only location with a velocity ratio above $U_{jet}/U_{up} > 2.0$ is immediately exiting the CCfoil. Another feature is the similarity between the velocity contours between the $y/s = -0.6$ and $y/s = -0.8$ locations, with small regions of separated flow on the bottom surface of the CCfoil as the exiting jet essentially blocks the mainstream flow. The $y/s = -0.2$ location is similar to the mid-span locations in that the exiting jet essentially blocks the mainstream flow such that a separated flow region exists, however, the Coanda effect is more noticeable with the upper jet remaining attached to the hydrofoil beyond the centerline of the hydrofoil. This results in a distinctly different jet trajectory for $y/s = -0.2$ than for the $y/s = -0.6, -0.8$ locations. Additionally, the effect of the blockage of the mainstream flow by the exiting jet on the boundary layer of the ground board is seen by $x/c = 1.15$. For the $y/s = -0.9$ location, the tip has a noticeable effect on the orientation of the exiting jet. For this span location, flow structures within the mainstream flow influences the trajectory of the jet towards downstream instead of being blocked.

The actual location of the CCfoil planar jet is better defined by the relative turbulence contours. Figure 59 presents the relative turbulence levels in the vertical direction with superimposed streamlines defined by the velocity components for the “Slight Flow” condition. The figure indicates clearly a defined jet surrounded by low turbulence flow for the $y/s = -0.6$ and $y/s = -0.8$ span locations. The orientation of the jet leaving the CCfoil is 90° with respect to the mainstream flow. This is in contrast to the orientation of the jet for the $y/s = -0.2$ location in which the jet is oriented slightly back upstream. Also noticeable for the $y/s = -0.2$ location is the increased turbulence downstream of the CCfoil related to the proximity of the ground board and the induced flow field from the exiting jet. For the $y/s = -0.9$ location, the orientation of the exiting jet is about 30° with respect to the mainstream flow with an increased turbulence level caused by the tip vortex above the jet location. The shift of the orientation of the jet for the $y/s = -0.9$ location is either caused by a variance in the magnitude of the jet flow rate near the tip or by the influence of the tip vortex located above the exiting jet.

A greater variation in the flow field about the span is seen for the “Assisted Lift” flow condition, shown in Figure 60, defined by $C_{\mu U} = 0.15$ and $C_{\mu L} = 0.0035$. In short, all of the non-uniformities described for Figure 58 for the “Slight Flow” condition are magnified for the “Assisted Lift” condition. One variation is the lack of reverse flow on the lower side of the CCfoil, for the $y/s = -0.6$ and $y/s = -0.8$ locations, due to the presence of a non-zero lower jet. The increased turning of the CCfoil jet for the $y/s = -0.2$ location compared to the mid-span location has magnified with the increase in flow.

For the $y/s = -0.2$ location, a distinct blockage of the mainstream is noticeable with the jet orientation similar to that of the “Slight Flow” condition. The flow disturbances caused by the ground board/jet interaction blocks the flow from the top surface of the foil. This results in a large region of velocity defect downstream of the CCfoil. For the $y/s = -0.6$ position, the jet is oriented 90° to the mainstream flow with some blockage of the mainstream flow. However, without the influence of the ground board, the flow over the top of foil “fills” this region of blocked mainstream flow. For the $y/s = -0.8$ and $y/s = -0.9$ span locations, the jet orientation remains 90° to the mainstream flow at the trailing edge of the CCfoil, but other flow features at

these span locations influence the jet. These flow features are better identified using the relative turbulence level shown in Figure 61.

From the relative turbulence level, the only spanwise location that is free of influence from other flow structures is $y/s = -0.6$. For this location, the jet retains a significant downward orientation within the measurement region as compared to the “Slight Flow” condition. This pristine flow is not observed for the other spanwise locations. For the $y/s = -0.2$ location, a transition between low turbulence mainstream and higher turbulence secondary flow is seen at $z/c \approx 0.0$. This transition suggests that the interaction is between the ground board and the exiting jet as opposed to the ground board and CCfoil.

For the $y/s = -0.8$ span location, two secondary flow structures are apparent within the measurement region. The first, located at $x/c > 1.2$, has minimal influence on the exiting jet. However, a second flow structure is noticeable upstream of the jet below the CCfoil. This flow structure does not alter the orientation of the jet, but acts more like a superimposed jet with a more streamwise orientation and a much larger region high turbulence. The $y/s = -0.9$ span location exhibits little similarity with the pristine flow field shown at $y/s = -0.6$. The jet is turned immediately downstream and is influenced by two secondary flow structures. The first is oriented above the exiting jet and probably corresponds to the tip vortex. A second flow structure is located below the jet, but the origin of this flow structure is not clearly evident. However during the cavitation experiments, a vortex originating at the $y/s = -0.8$ spanwise location couples with the tip vortex under certain flow/tunnel condition.

These figures allude to significant spanwise non-uniformity for the single sided flow conditions. At the exit of the Coanda jet, the velocity magnitude is similar about the span for both the “Slight Flow” and “Assisted Lift” conditions. This indicates that the non-uniformity about the span is caused by interactions with flow structures and not with a non-uniform jet. Figure 62 and Figure 63 address the uniformity of the flow field about the span for the axial and vertical mean velocity, respectively. These figures present the flow field for the various flow conditions at an axial location $x/c = 1.083$ and $U_{up} = 3.04 \text{ m/s}$. For interpretation of these figures, neither the regions of downward flow nor the regions of low axial flow directly correspond to the CCfoil jet. However, these regions are influenced by the magnitude and location of the CCfoil jet. For the quasi-zero or reverse axial flow, these regions typify either vortices or flow that has been stagnated by the CCfoil jet. Regions of accelerated axial flow are typical of either potential flow effects about the CCfoil and vortical structures, or indicative of the CCfoil jet. Regions for non-zero vertical velocity are caused by potential effects about the CCfoil, by vortices, or by mainstream flow “filling” the regions the flow field that have been “blocked” by the CCfoil jet.

As shown in Figure 62, a velocity deficit exists at the root for all of the flow conditions. In addition, the tip vortex is apparent for all of the flow conditions with the exception of the “Maximum Flow”, $C_{\mu U} = 0.18$ and $C_{\mu L} = 0.00$. However, if the “Slight Flow” and “Moderate Flow” conditions are examined in Figure 63, the location of the tip vortex is progressing further from the root. Therefore, the tip vortex for the “Maximum Flow” is likely beyond the measurement region for this $x/c = 1.083$ location.

As for the uniformity, for all of the flow conditions except the “Maximum Flow” condition, two-dimensionality exists somewhat over the middle 50% of the span ($-0.25 < y/s < -0.75$) at this $x/c = 1.083$ location. A flow anomaly is prevalent at the span location of $y/s = -0.75 \sim -0.8$,

particularly visible from the vertical component of the flow in Figure 63. This flow anomaly could correspond to the vortex identified at $y/s = -0.8$ during the cavitation experiments. Additionally, comparing the axial velocity contours for these flow conditions with the streamlines shown in Figure 58 and Figure 60, the regions of accelerated flow located between $y/s = -0.9$ and $y/s = -1.0$ are indicative of the CCfoil jet turned parallel with the flow.

For the “Maximum Flow” condition, the region of two-dimensionality is decreased to about 15 % of the span ($-0.4 < y/s < -0.55$). This flow condition is at the level in which degraded performance for C_L is expected for the single slot configuration. This flow condition has a large region of reverse flow between $y/s = -0.25$ and $y/s = -0.65$. At this vertical location, $0.0 > z/c > -0.25$, the CCfoil jet would be located upstream of the axial location, $x/c = 1.083$, given in Figure 63. Therefore, the cause of this reverse flow is that the CCfoil jet stays attached to the foil well beyond 90° similar to the $y/s = -0.2$ location for Figure 60.

As previously mentioned, the mean vertical and axial velocities yield insight to the uniformity of the flow field and the identification of three-dimensional flow structures. Yet, identification of the location of the CCfoil jet is difficult. However with the exception of the three-dimensional flow structures and the CCfoil jet, the mainstream consists of low turbulence flow. Therefore from the relative turbulence contours, the location of the CCfoil jet can be identified.

The propagation of the jet location downstream is shown in Figure 64 for the “Slight Flow” condition. The tip vortex is located near $y/s = -0.95$ and $z/c = 0.0$ and influences the jet between $y/s = -0.75$ and the tip. The flow structure caused by the presence of the ground board influences the jet between the root and $y/s = -0.25$. These flow structures are consistent in location between $x/c = 1.083$ and $x/c = 1.271$. The jet is located at $z/c = -0.2$ and $x/c = 1.083$ and progresses slightly downward with increasing x/c . Also evident is the varying location of the jet between the $y/s = -0.9$ spanwise location and the $y/s = -0.6, -0.8$ spanwise locations previously discussed with Figure 58. At $x/c = 1.271$, the jet is located at $z/c \approx -0.2$ at $y/s = -0.9$ as opposed to $z/c \approx -0.3$ for the $y/s = -0.6, -0.8$ spanwise locations. The variation of the jet position can be explained with the orientation of the tip vortex highlighted by the vertical velocity component in Figure 65. The reduction of the area unaffected by the tip vortex and by the flow structures caused by the ground board and jet interaction as the flow rate is increased is shown in Figure 66 from the axial relative turbulence at $x/c = 1.083$.

For the sake of completeness, Figure 67 presents the effect of varying the angle of attack on the flow field at $x/c = 1.083$ for the “Slight Flow” condition. As with other test configurations, the location of the jet is not contained within the measurement plane allowed by the window apertures. By comparison of Figure 67 with the “Slight Flow” condition presented in Figure 66, one observation is that the shape and relative location of the CCfoil jet to the trailing edge of the CCfoil ($z/c = 0.0$ for $\alpha = 0^\circ$ and $z/c = -0.8$ for $\alpha = 10^\circ$) is consistent between $\alpha = 0^\circ$ and $\alpha = 10^\circ$. The second observation is that the flow structure near the root remains attached to the trailing edge of the CCfoil, which confirms the theory that the flow structure is a ground board/jet interaction as opposed to a ground board/foil interaction.

Cavitation

One of the research objectives was to determine the cavitation inception location on the circulation control hydrofoil and the impact of subsequent cavitation on the ability of the jet to

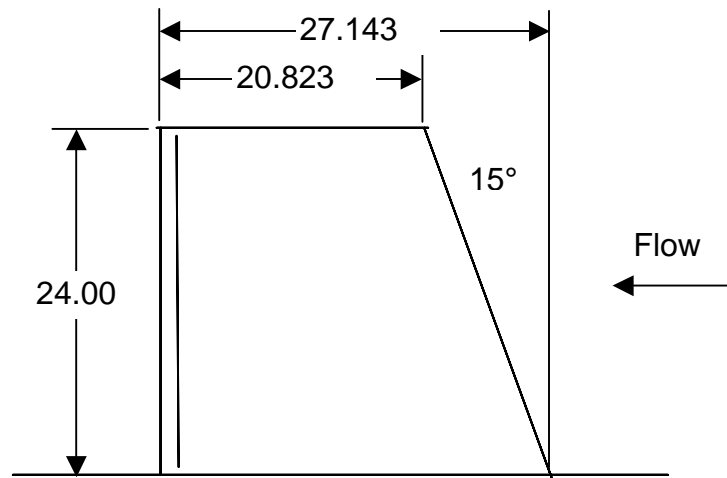
produce circulatory lift. Due to load limitations on the model and force balance this effort was accomplished by dropping pressure then gradually increasing slot flow to increase lift. Photographs of the types of cavitation observed are shown in Figure 68 through Figure 71. As expected tip vortex cavitation is first to incept. With the objective of a nearly constant spanwise C_{μ} and no effort to taper the gap to reduce the tip loading it was expected a strong tip vortex would develop at augmented lift conditions. This onset of tip vortex cavitation is shown in Figure 68 prior to the inception of any Coanda surface cavitation. Also shown in Figure 68 is the presence of a lightning vortex originating inboard from the tip at 70-80% of the span. These localized flashes of cavitation are presumably due to vortical structures within the jet getting rolled up into the tip vortex. This early onset of tip vortex cavitation could be mitigated through the addition of a tip cover plate as shown in Figure 38. The delay in vortex cavitation inception through the addition of this plate is shown in Figure 74. This figure plots the cavitation number at inception versus the lift coefficient. The lift coefficient (C_L) and blowing coefficient (C_{μ}) are analogous for a fixed angle of attack. The tip plate is shown to delay inception for a given sigma to a C_L of three times the simple cover plate configuration. As the pressure in the tunnel is decreased the onset of Coanda surface cavitation is observed behind the slot lip face. An overall view of this type of cavitation is shown in Figure 69 and a close-up in Figure 70. The non-uniform spanwise distribution is because this picture was taken just past inception where small differences in slot lip finish or gap setting could result in uneven onset. What is noted is that the onset of cavitation does not correspond to the locations of push/pull screws used to set the slot gap height. Lower slot blowing at a lower test section pressure is shown in Figure 71. A more uniform distribution of cavitation is observed progressing towards the root and tip of the foil.

The impact on lift was investigated by running through a range of blowing coefficients at three tunnel static pressures, corresponding to cavitation number of 13.5, 10.23, and 6.57. As the extent of cavitation increases the lift gradually rolls off as shown in Figure 72. At no time did the jet detach from the Coanda surface due to the presence of cavitation. No increase in unsteady loading was observed in the load balance signals at the lowest pressures tested.

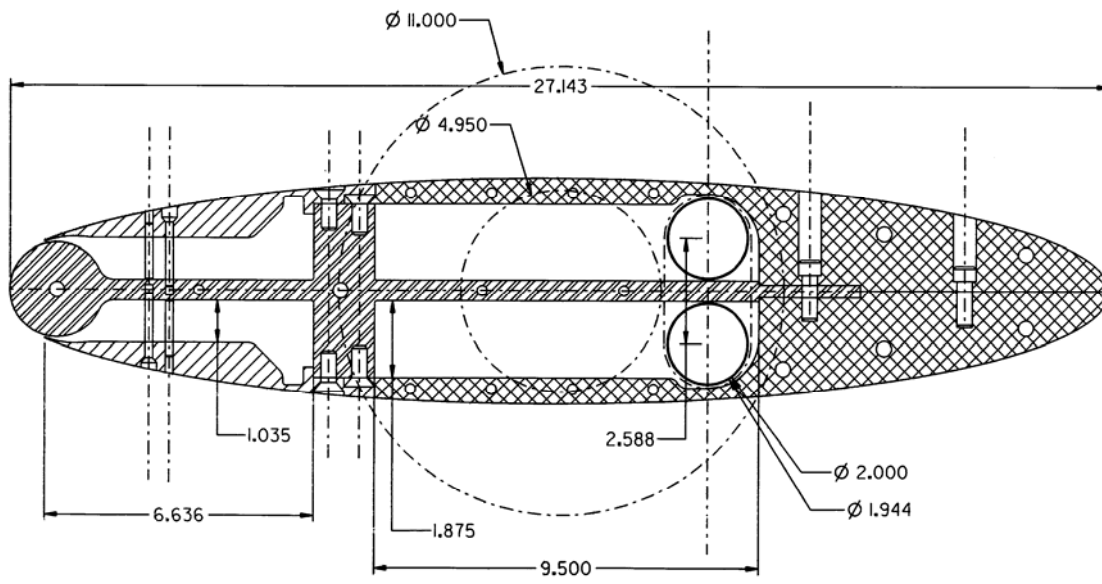
A summary of cavitation inception is shown in Figure 73. Types of cavitation called include tip vortex, lightning type vortices at 70% and 80% span, and Coanda surface cavitation. Also investigated was the impact of the lower slot bleed technique used to offset the early loss of lift from excessive turning of the jet. It was determined that lower slot flow had no impact on cavitation inception. There is also good symmetry between Coanda surface inception between upper and lower slot blowing. It should be noted that attempts to initiate cavitation at other than the trailing edge by pitching the model were unsuccessful. In terms of practical applications the conditions of speed and depth at which loss of lift was observed due to Coanda surface cavitation are outside the proposed operating regime of an underwater vehicle.

Conclusions

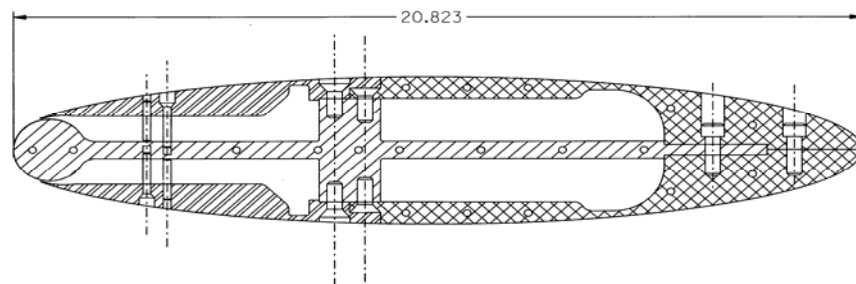
Performance of the CCfoil as a prospective control surface appendage on a marine vehicle exceeded expectations primarily due to the discovery of the second slot flow technique of offsetting the “trailing edge pressure drawdown.” This extensive documentation of loads due to AOA, slot flow blowing, and cavitation impact, along with detailed flow field measurements should serve as a database against which CFD can be benchmarked. Additional details regarding this data set or requests for data contained within should be addressed to Martin Donnelly, martin.donnelly@navy.mil.



a. Planform

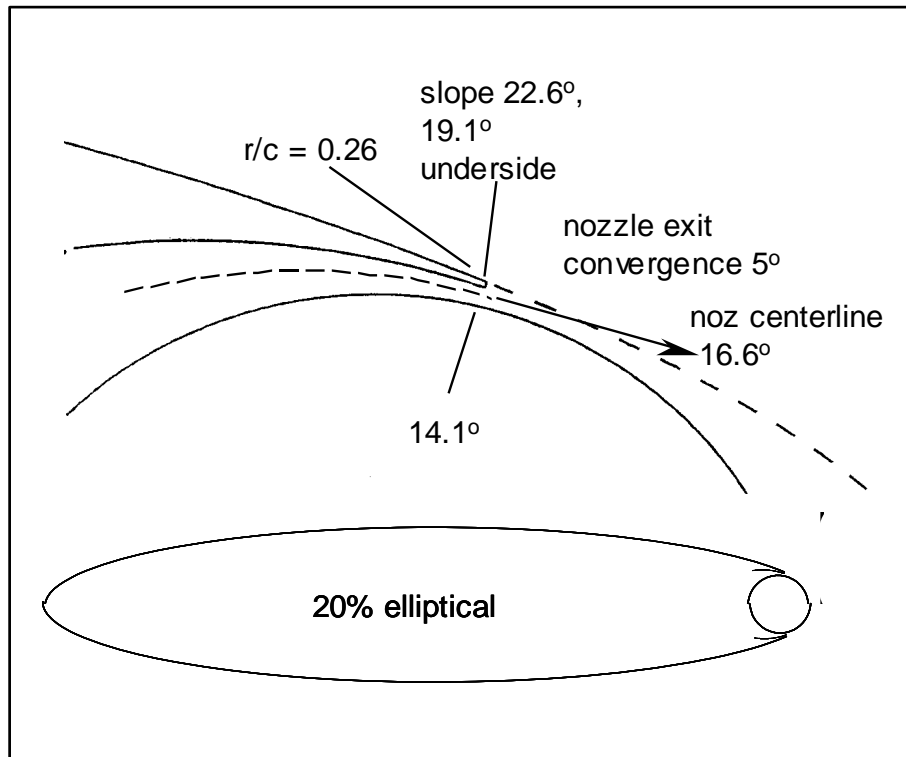


b. Root Section

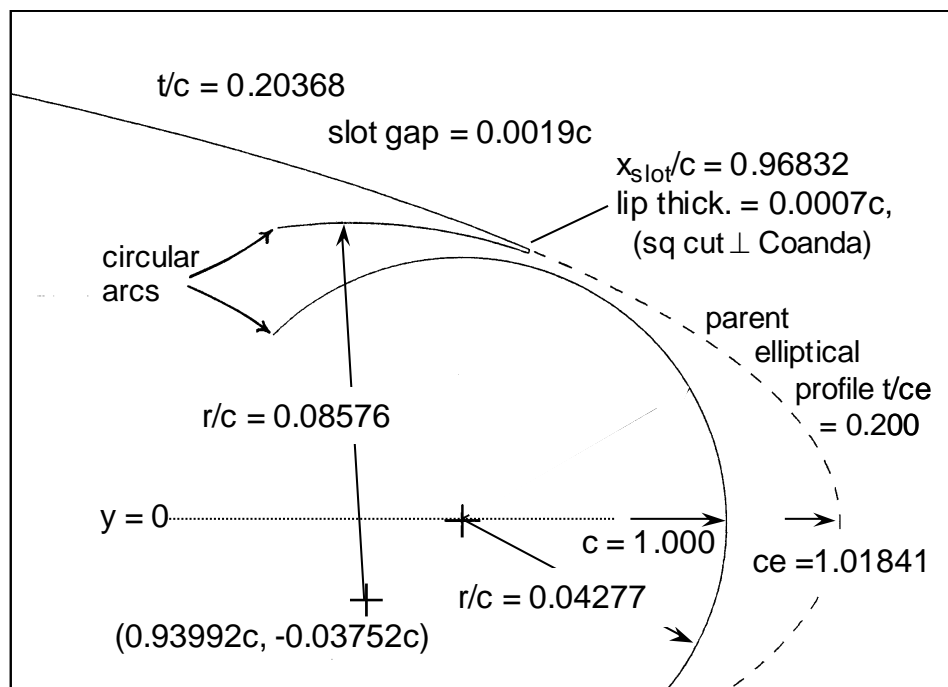


c. Tip Section

Figure 1. CC Hydrofoil Drawing



a. Slot Detail



b. Trailing Edge

Figure 2. Detail Drawing of Trailing Edge



Figure 3. Photograph of Brass Plate with Stainless Steel End-Plates and Screen

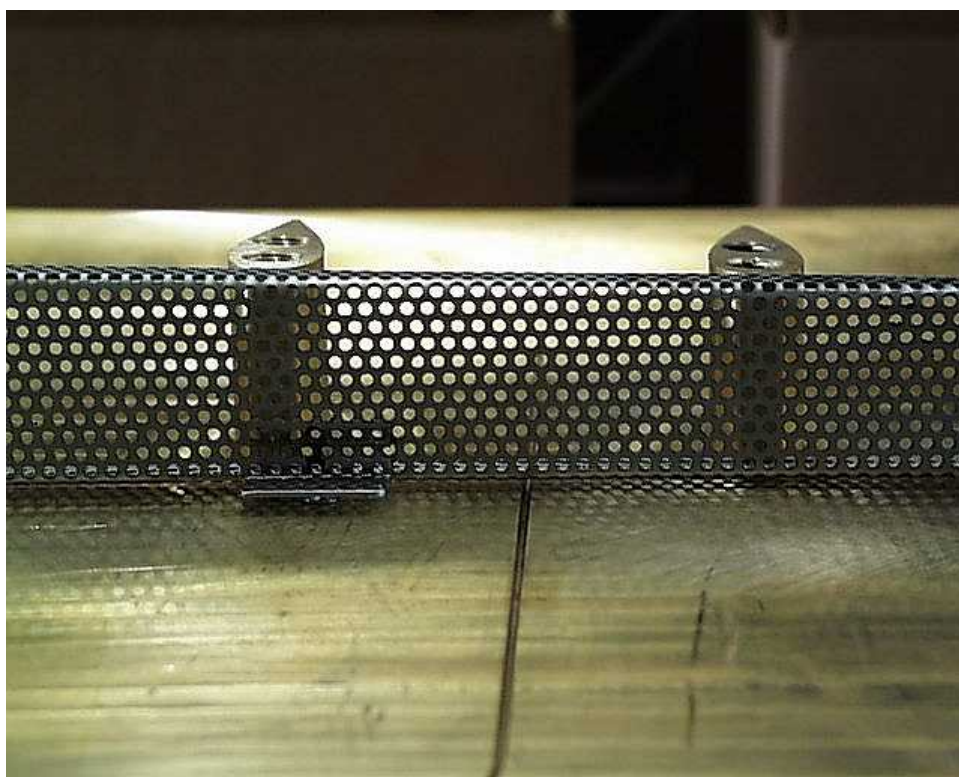
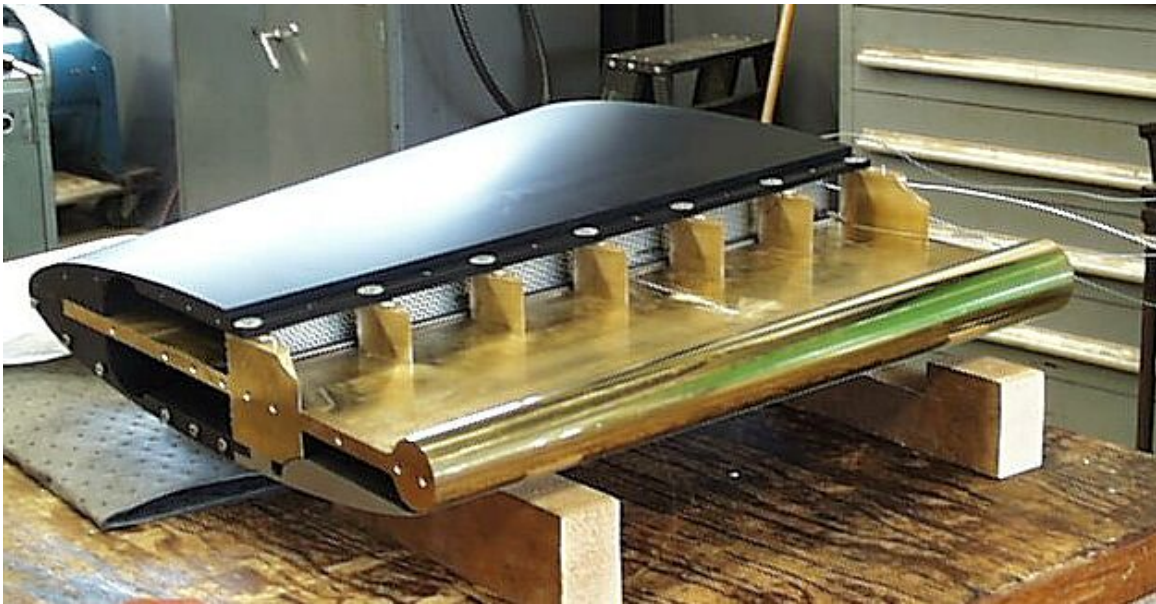


Figure 4. Close-Up View of Screen



a. View from Root



b. View from Tip with Tailing-Edge Cover Removed

Figure 5. Photograph of Assembled CC Hydrofoil Model without End-Plates

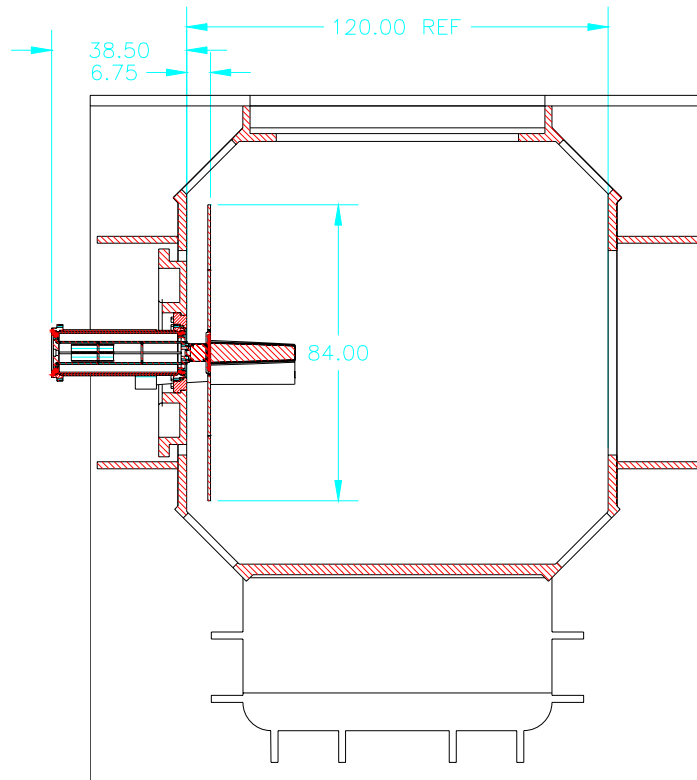


Figure 6. Cross-Sectional View of LCC Test Section Installation

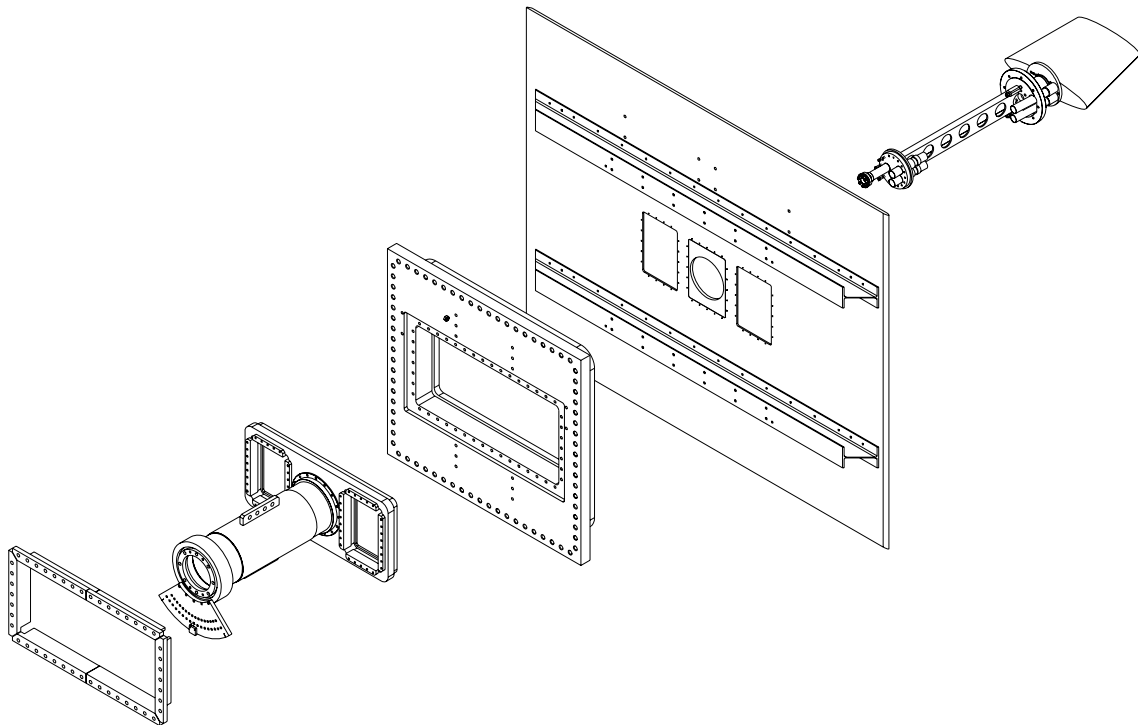
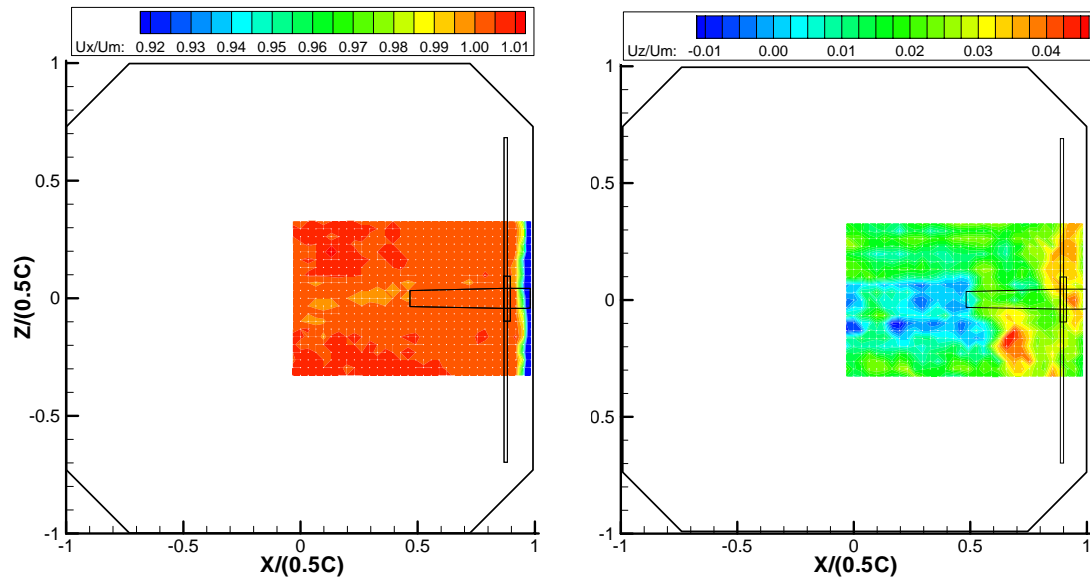


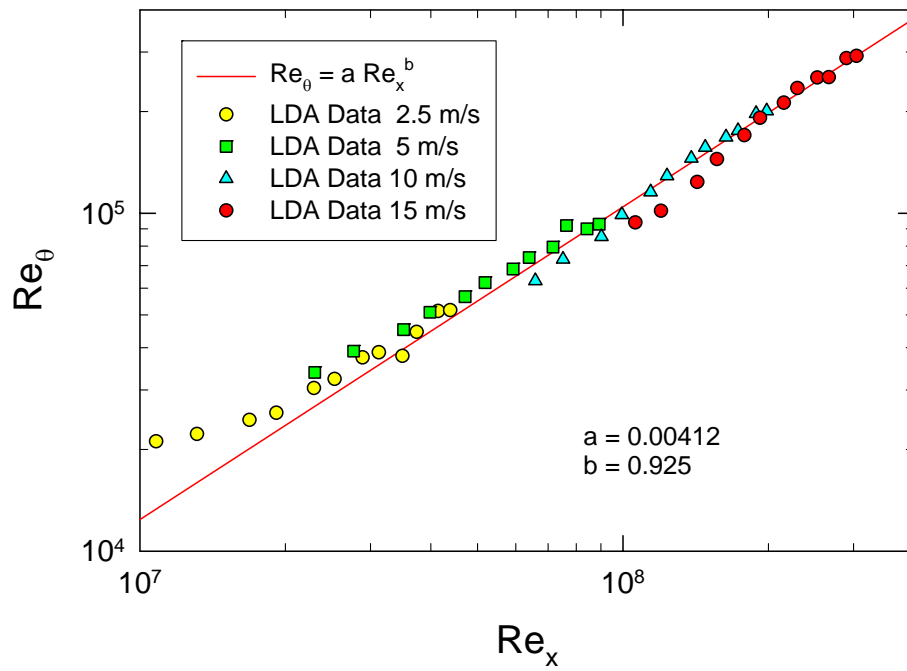
Figure 7. Exploded View of CC Hydroil LCC Installation



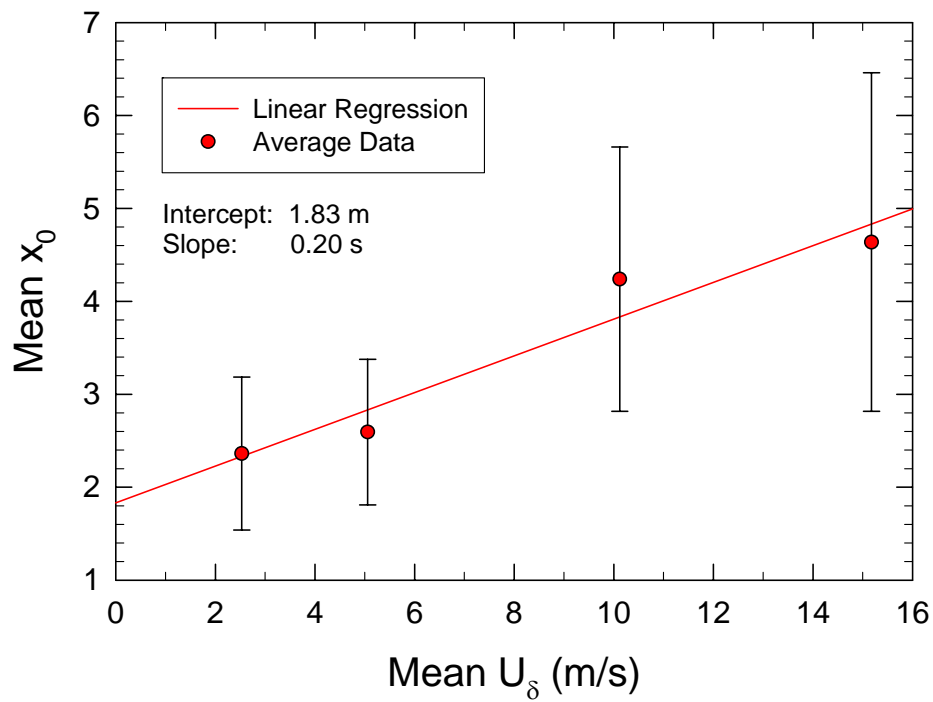
a. Axial Velocity

b. Vertical Velocity

Figure 8. Empty Test Section Velocity Contours for LCC



a. Reynolds Number from Momentum Thickness



b. Virtual Origin Relative to Center of Window 2 in Bay 1

Figure 9. Turbulent Boundary Layer Growth in LCC Test Section



Figure 10. Photograph of CC Hydrofoil Installation in LCC Test Section from Trailing Edge View

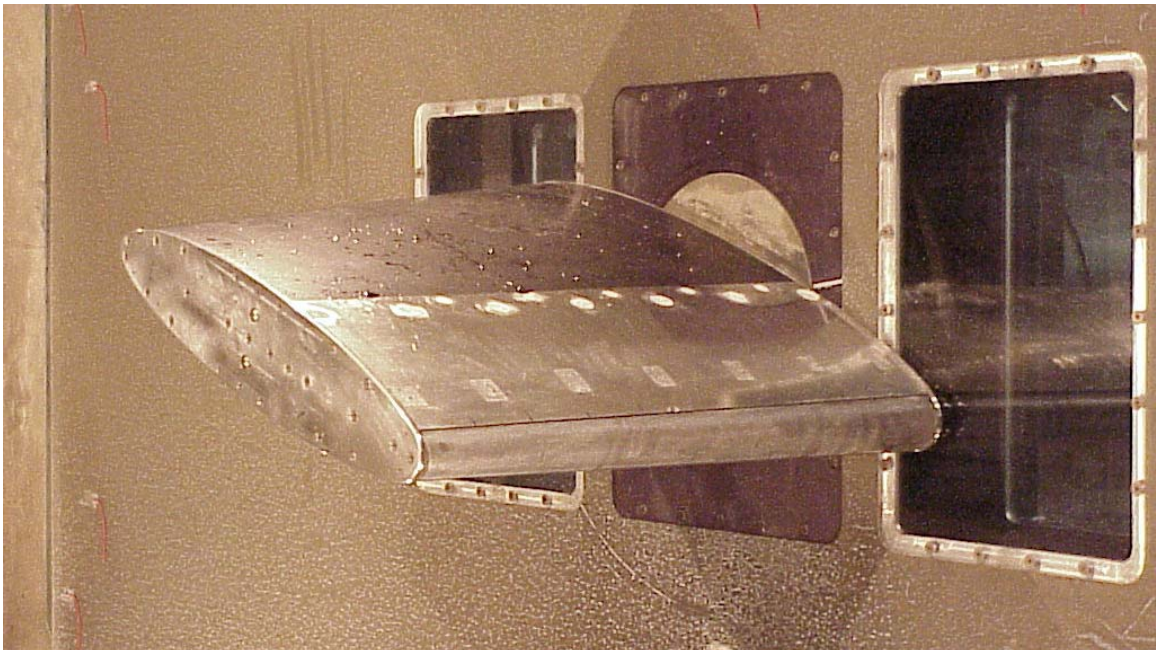


Figure 11. Photograph of CC Hydrofoil with View from Trailing Edge



Figure 12. Griswold R2GH15 centrifugal pump



Figure 13. Reliance SP600 motor controller and power junction box



Figure 14. Inlet to the pump (Elbow#4) LCC Upstream Vertical Leg



Figure 15. Flow Measurement layout showing Hoffer turbine flowmeter

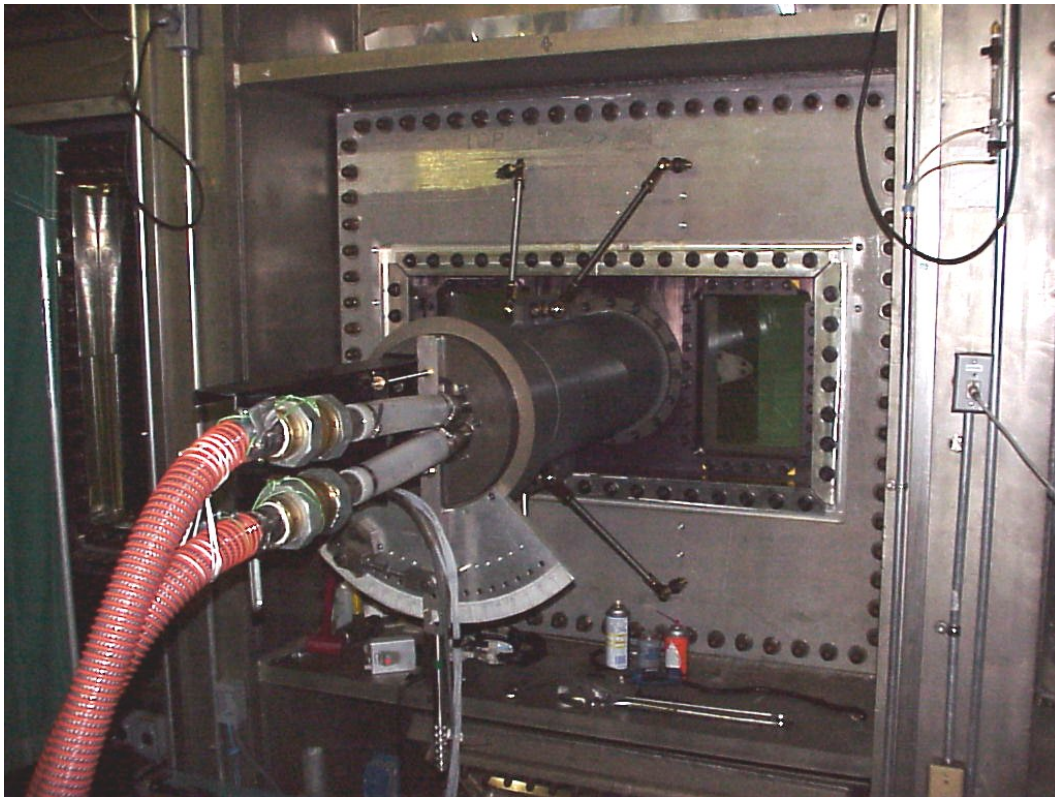


Figure 16. Photograph of External Installation in Test Section

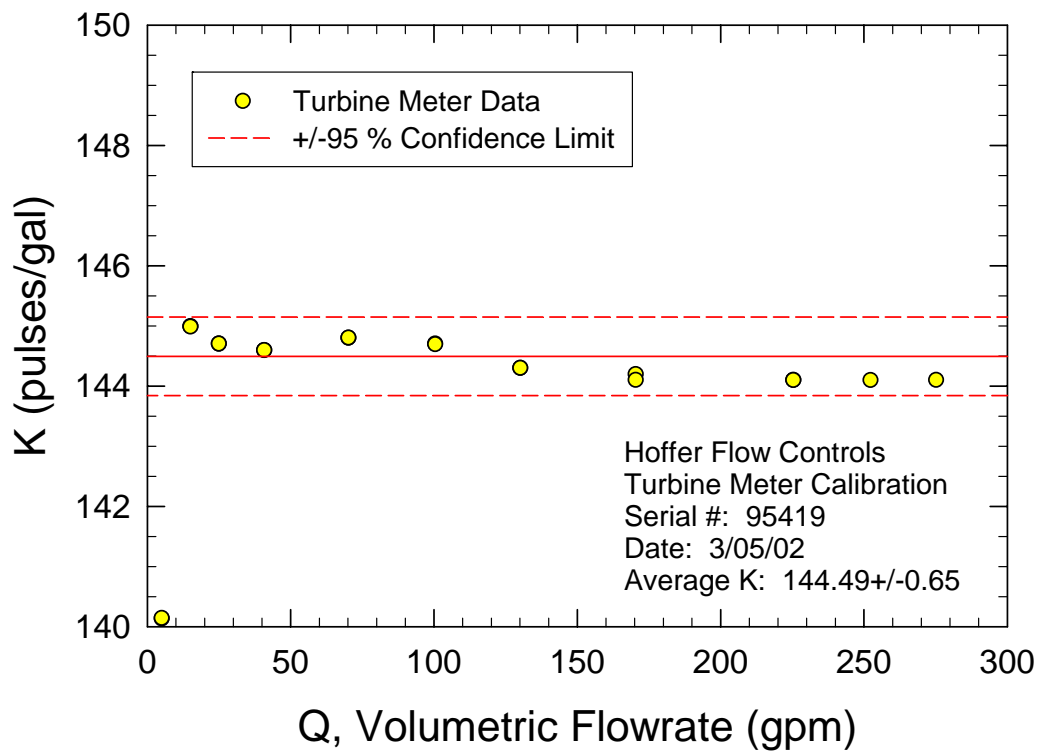
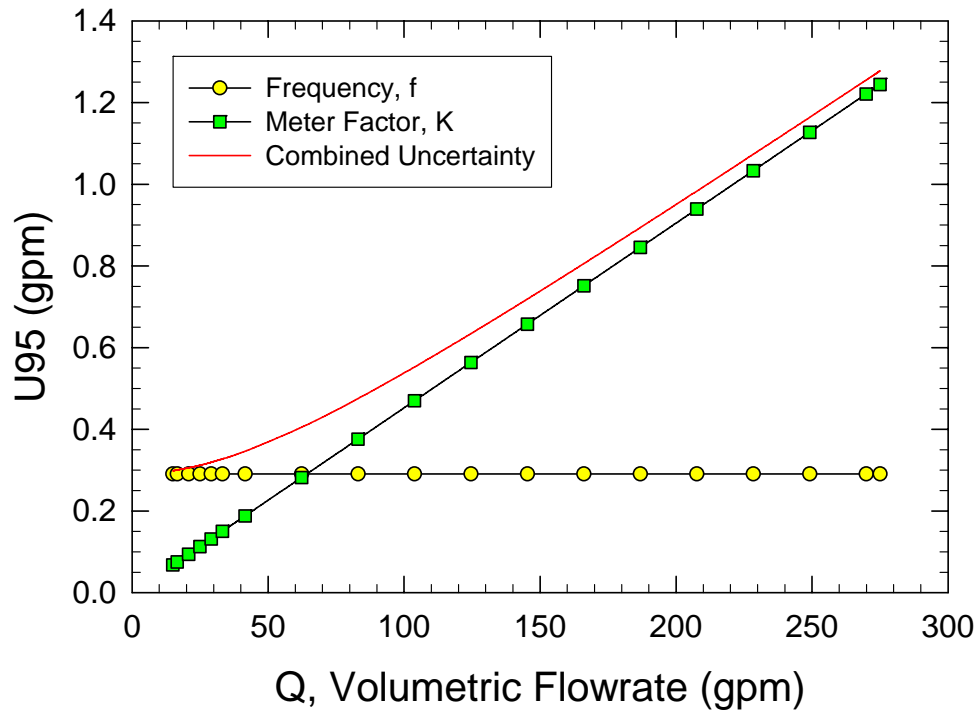
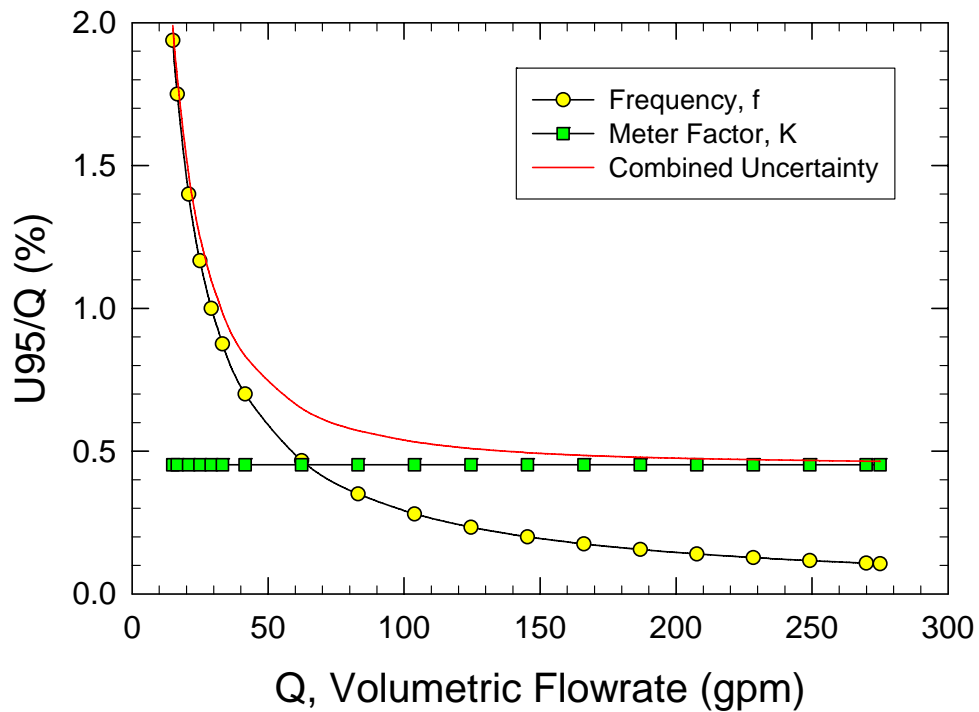


Figure 17. Turbine Meter Calibration for Slot Flow

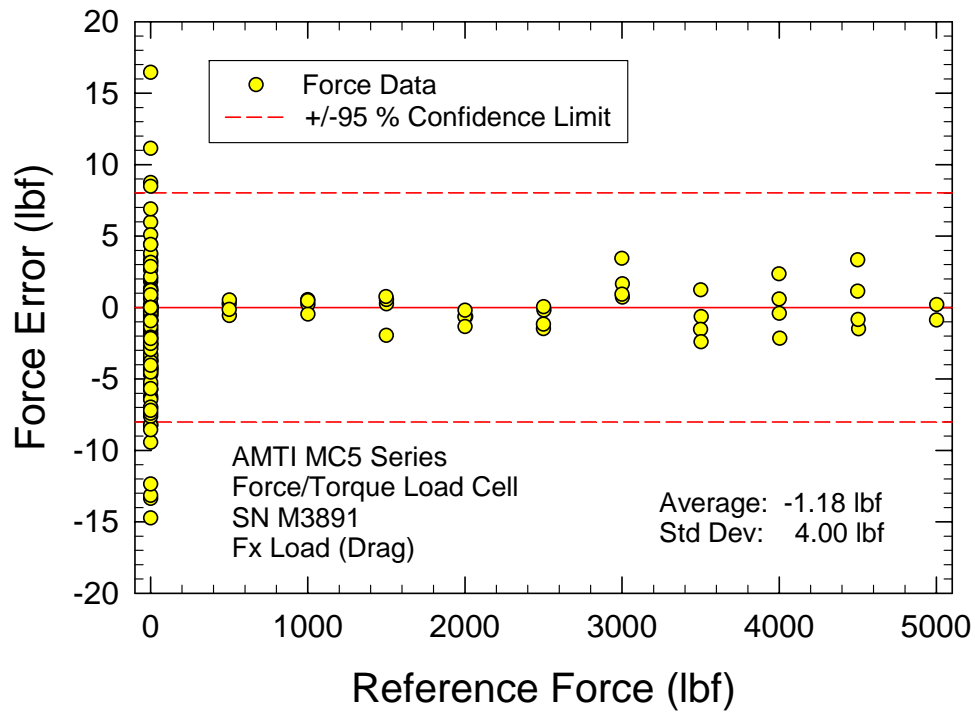


a. Absolute Uncertainty

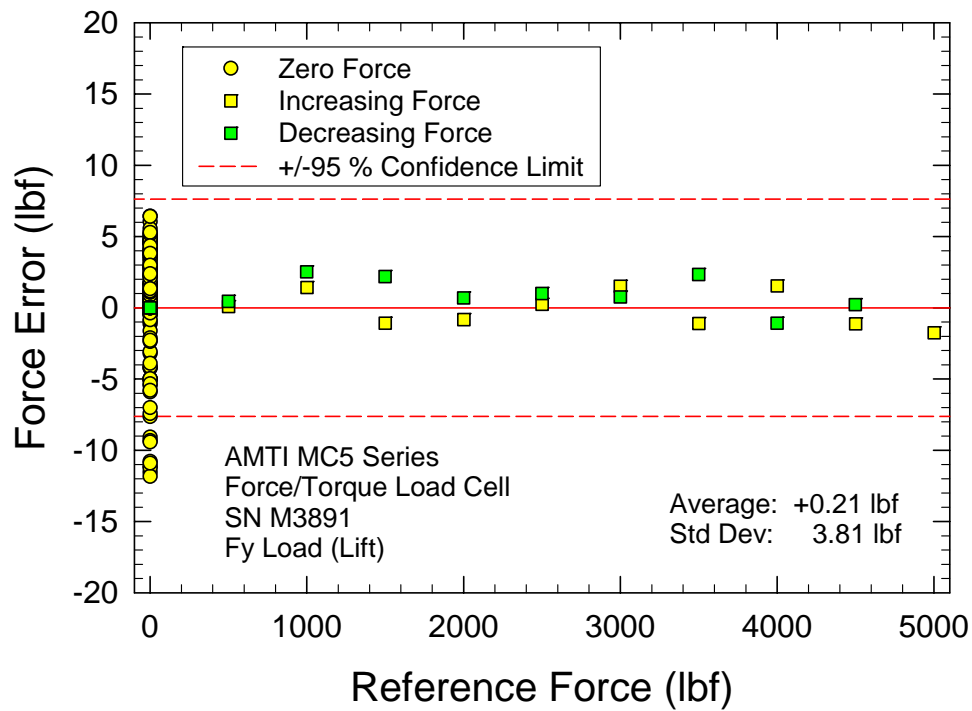


b. Relative Uncertainty

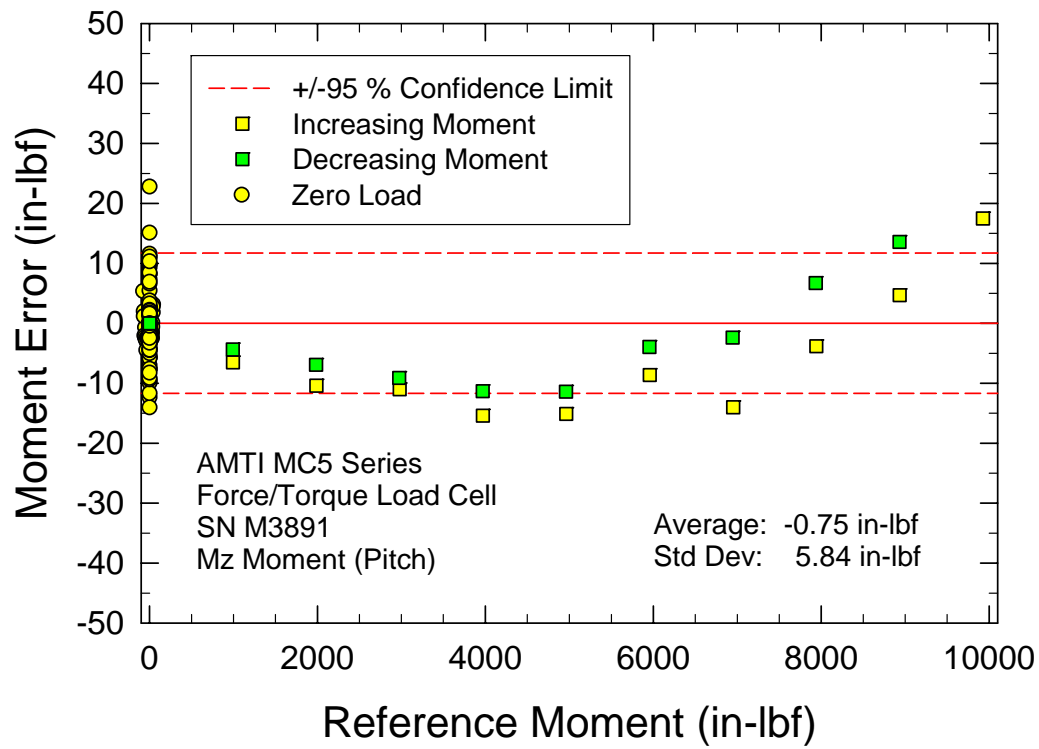
Figure 18. Uncertainty Estimates for Volumetric Flowrate of Turbine Meter



a. Fx Calibration (Drag)

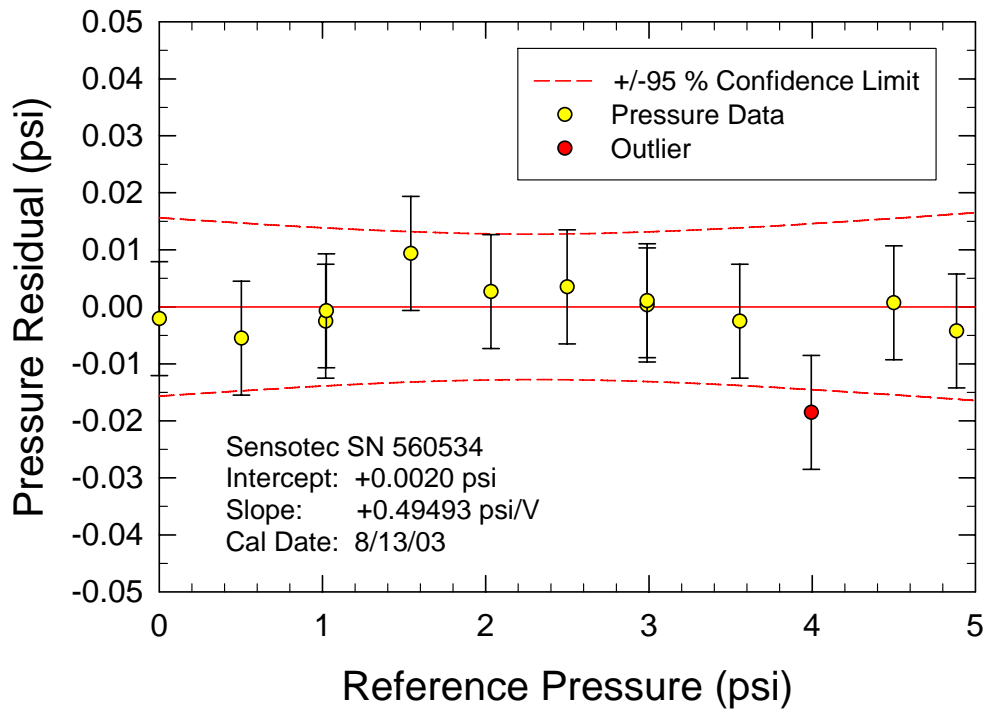


b. Fy Calibration (Lift)

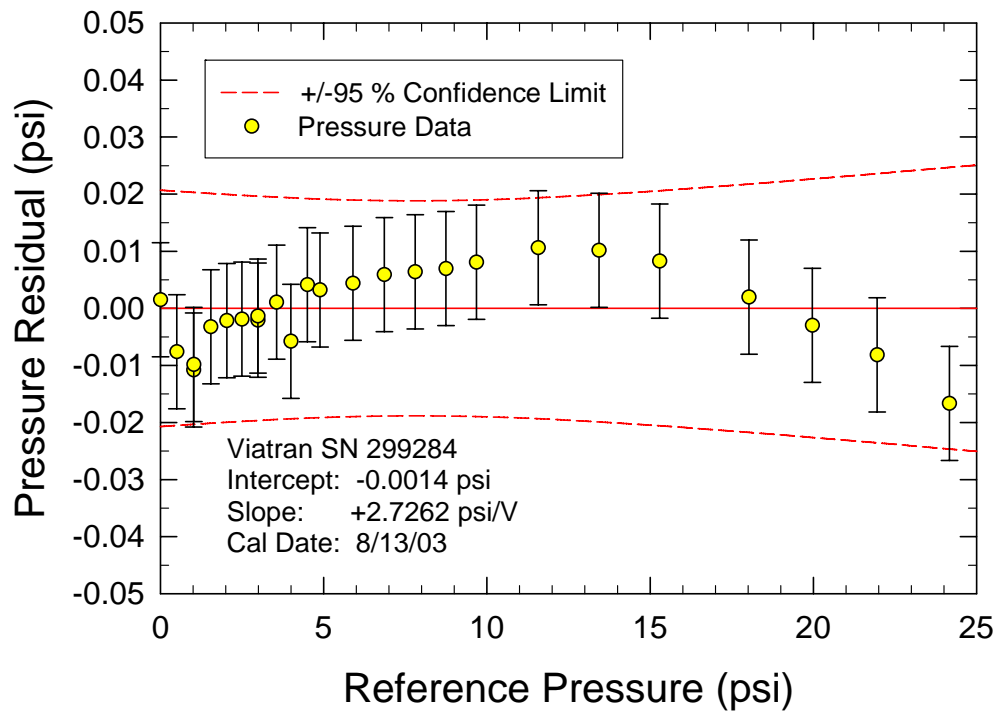


c. Mz Calibration (Pitch)

Figure 19. AMTI Force/Torque Cell Calibration

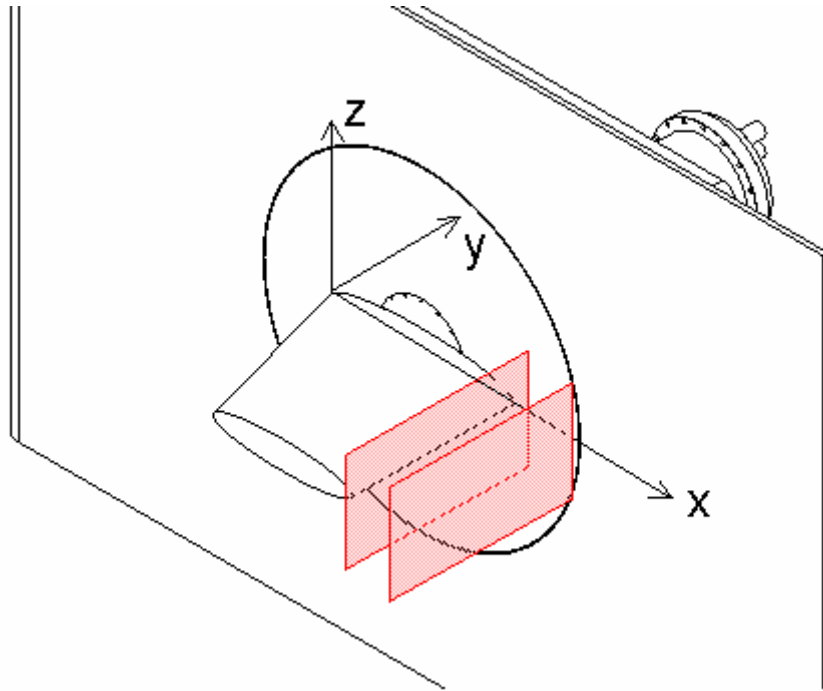


a. Sensotec 5 psig Range Transducer

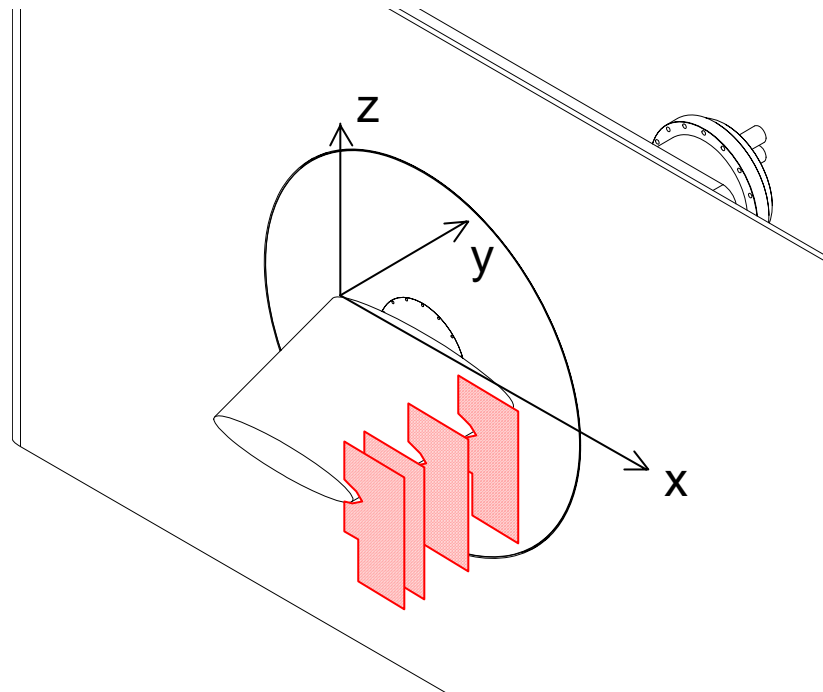


b. Viatran 25 psig Range Transducer

Figure 20. Pressure Transducer Calibrations for CCFoil Plenum Chamber



a. Spanwise Planes



b. Chordwise Planes

Figure 21. LDV Measurement Locations

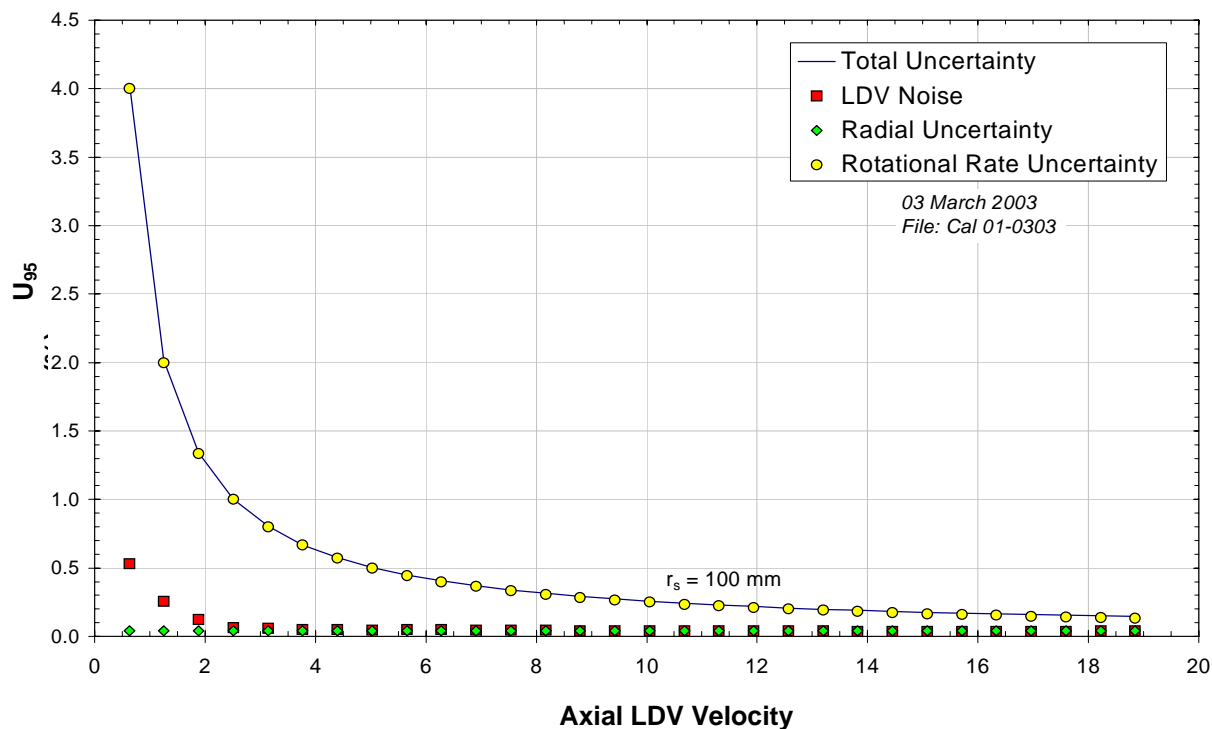


Figure 22. Relative Uncertainty in LDV Calibration with Spinning Disk at 100-mm Radius

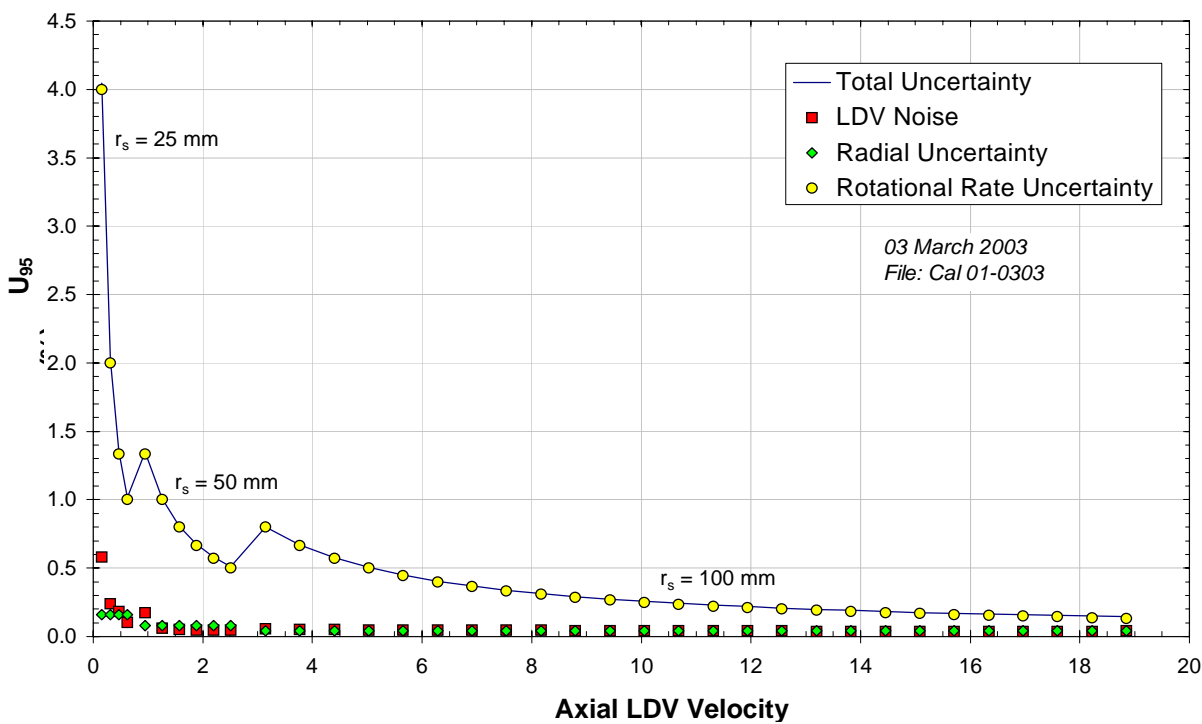


Figure 23. Relative Uncertainty in LDV Calibration for Varying Radial Distances

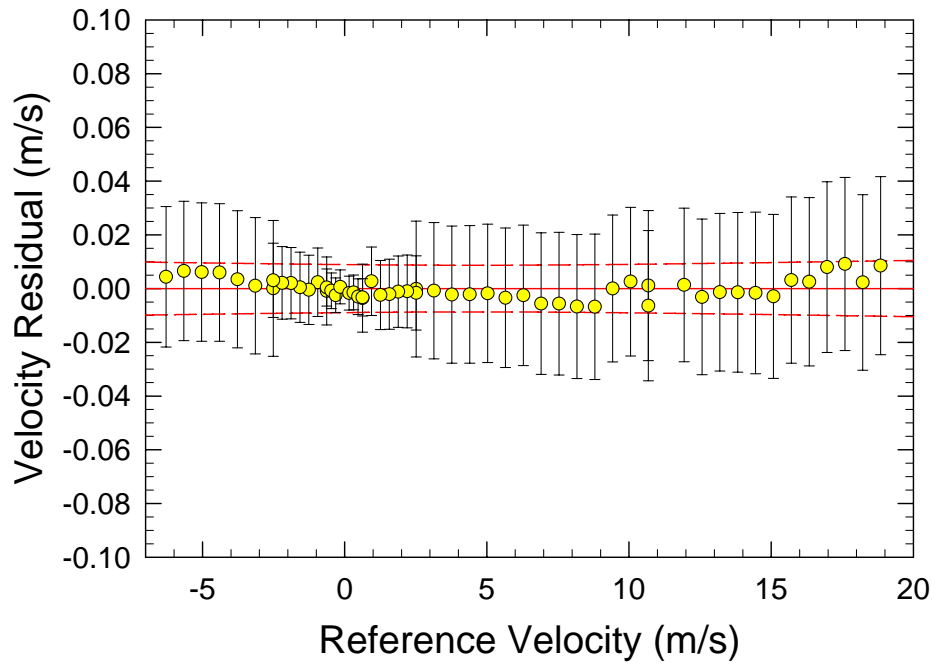


Figure 24. Residual Plot for Calibration of Axial Velocity

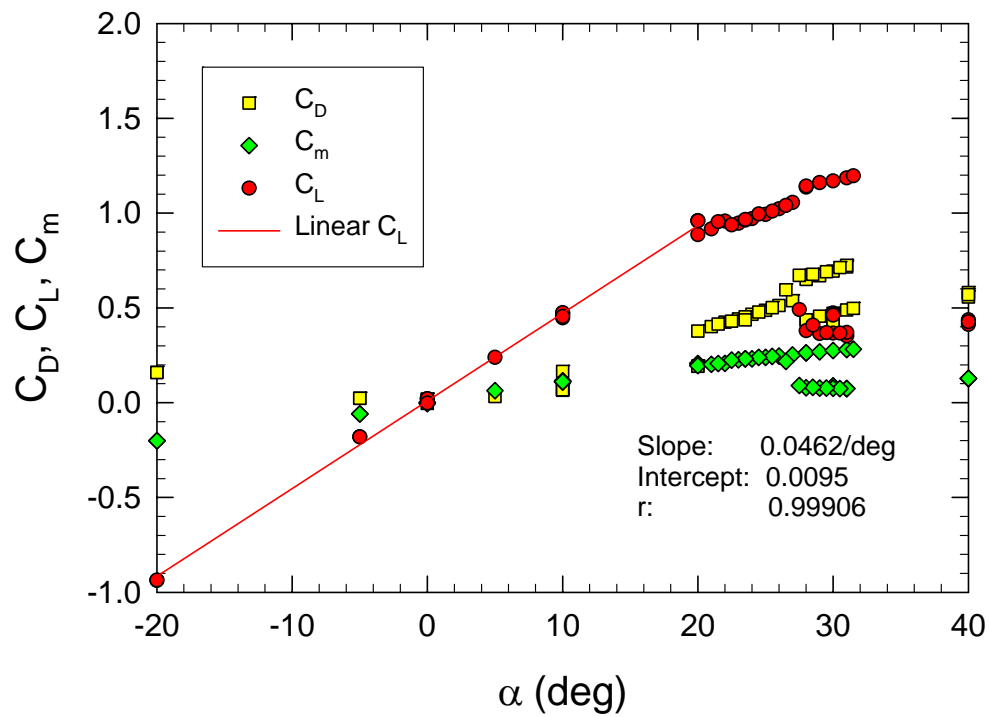


Figure 25. Force Coefficients with No Slot Flow

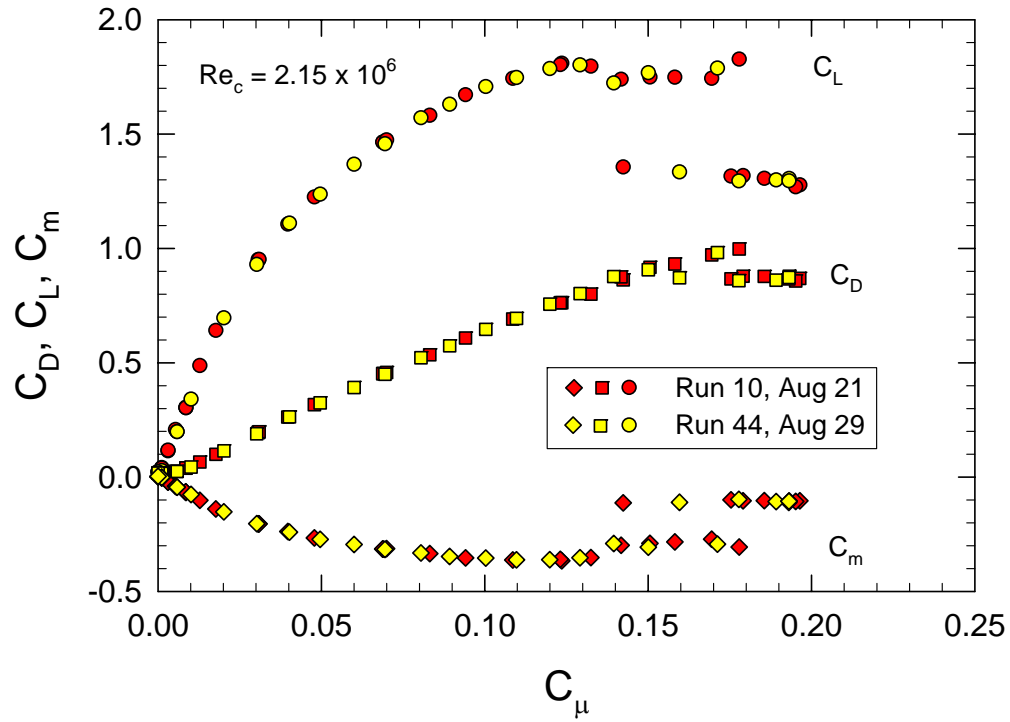


Figure 26. Force Coefficients with Upper Slot Flow at $\alpha = 0^\circ$

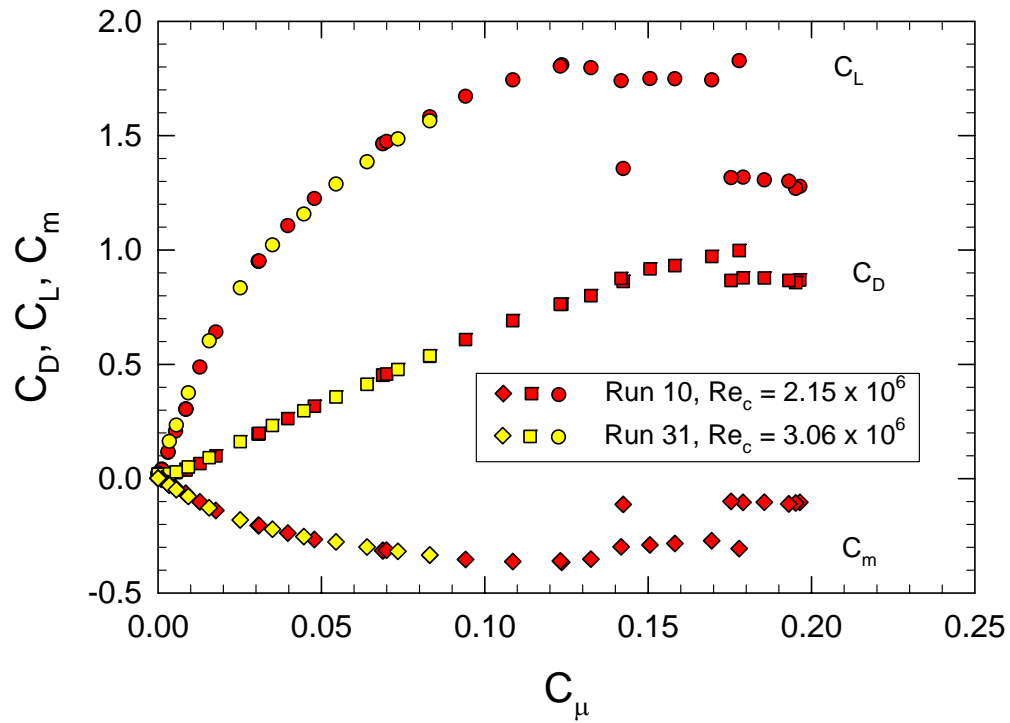


Figure 27. Force Coefficients with Upper Slot Flow at $\alpha = 0^\circ$ and $2 Re$

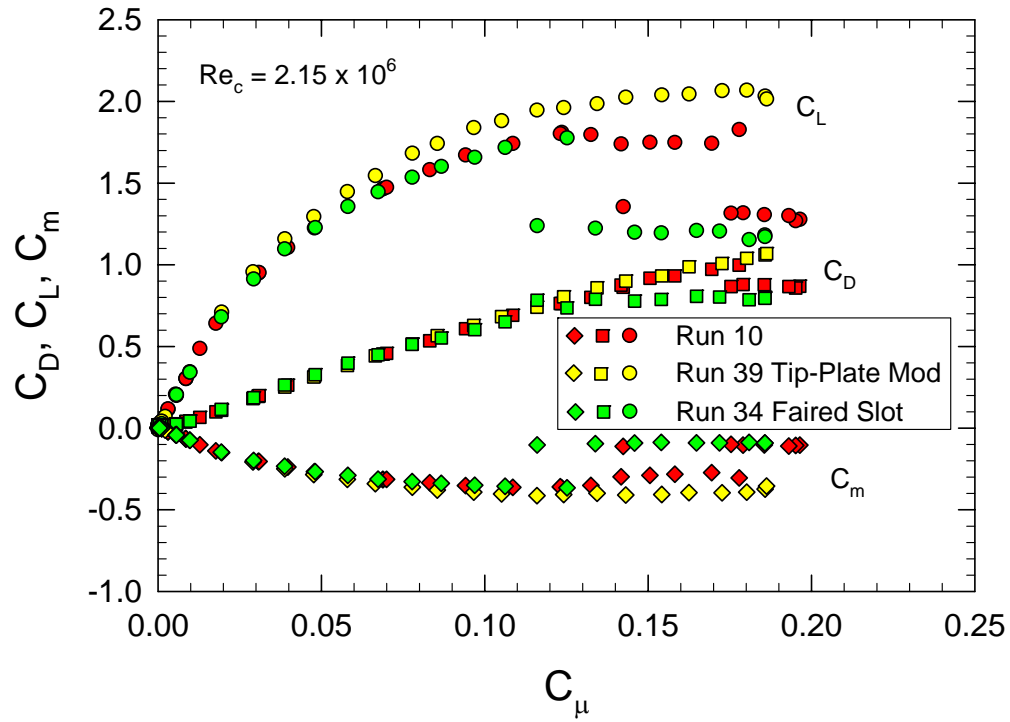


Figure 28. Force Coefficients for Faired Slot and Modified Tip-Plate at $\alpha = 0^\circ$

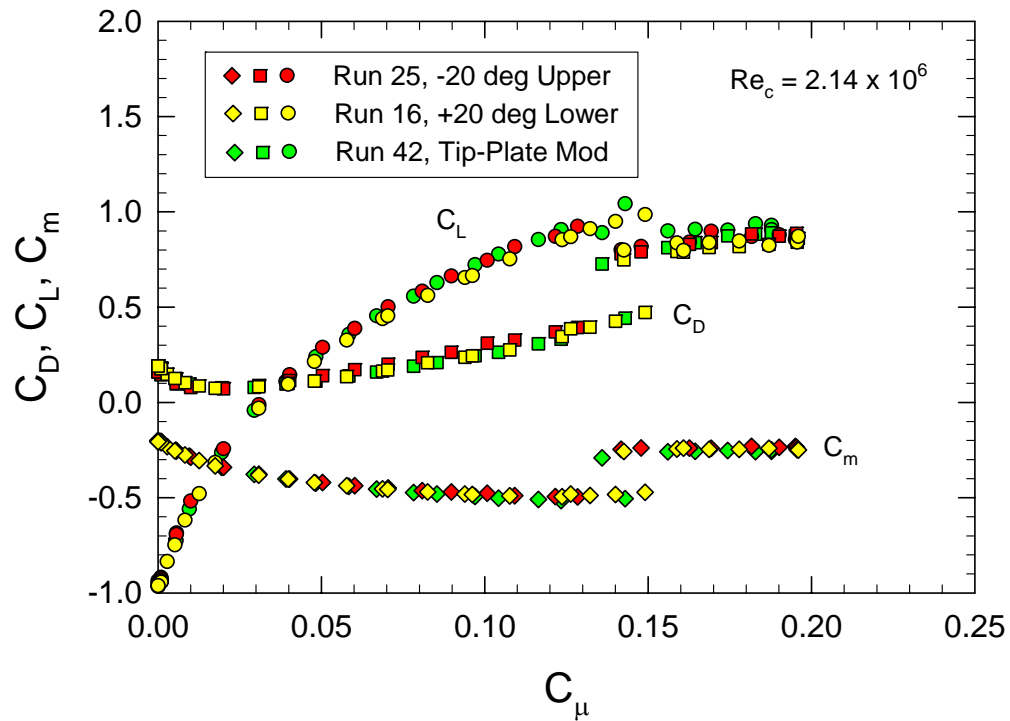


Figure 29. Force Coefficients with Upper Slot Flow at $\alpha = -20^\circ$

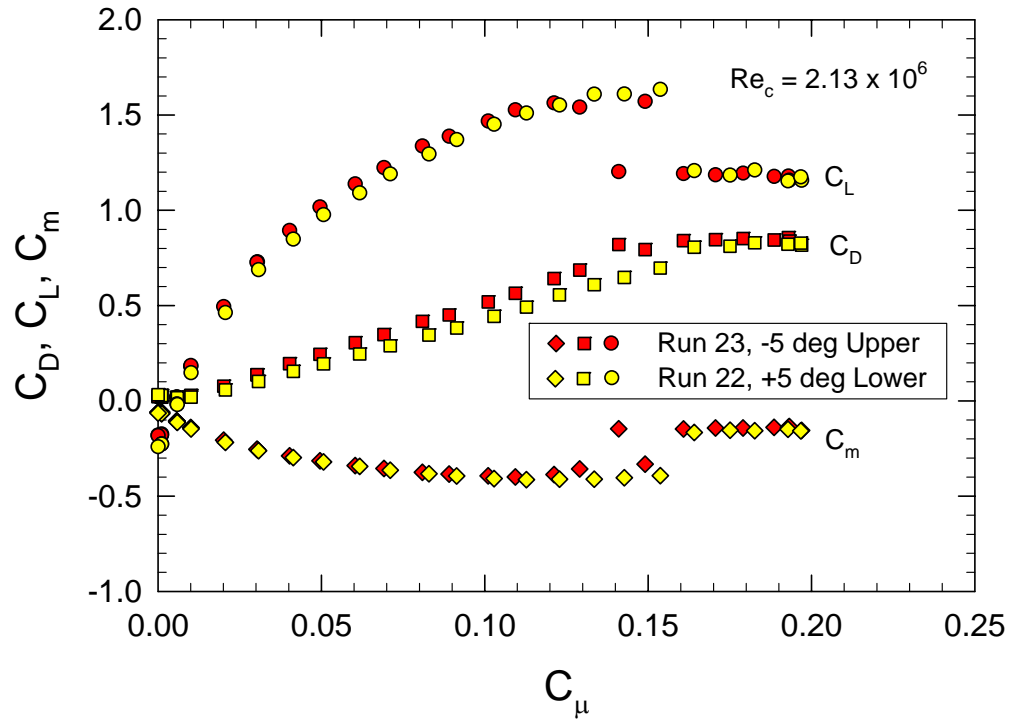


Figure 30. Force Coefficients with Upper Slot Flow at $\alpha = -5^\circ$

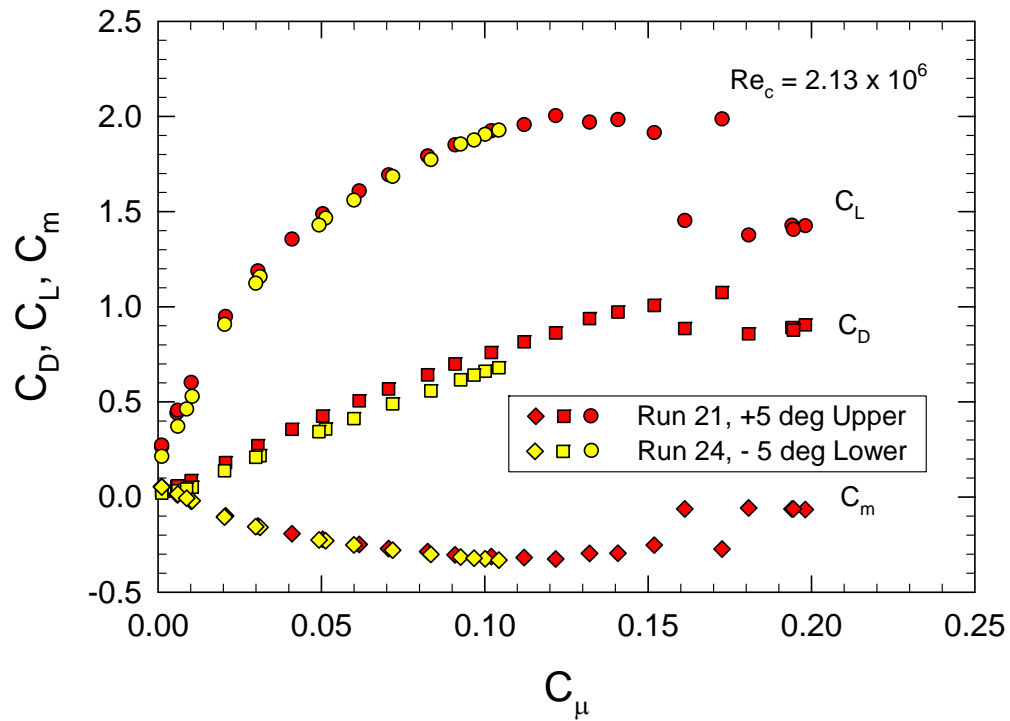


Figure 31. Force Coefficients with Upper Slot Flow at $\alpha = +5^\circ$

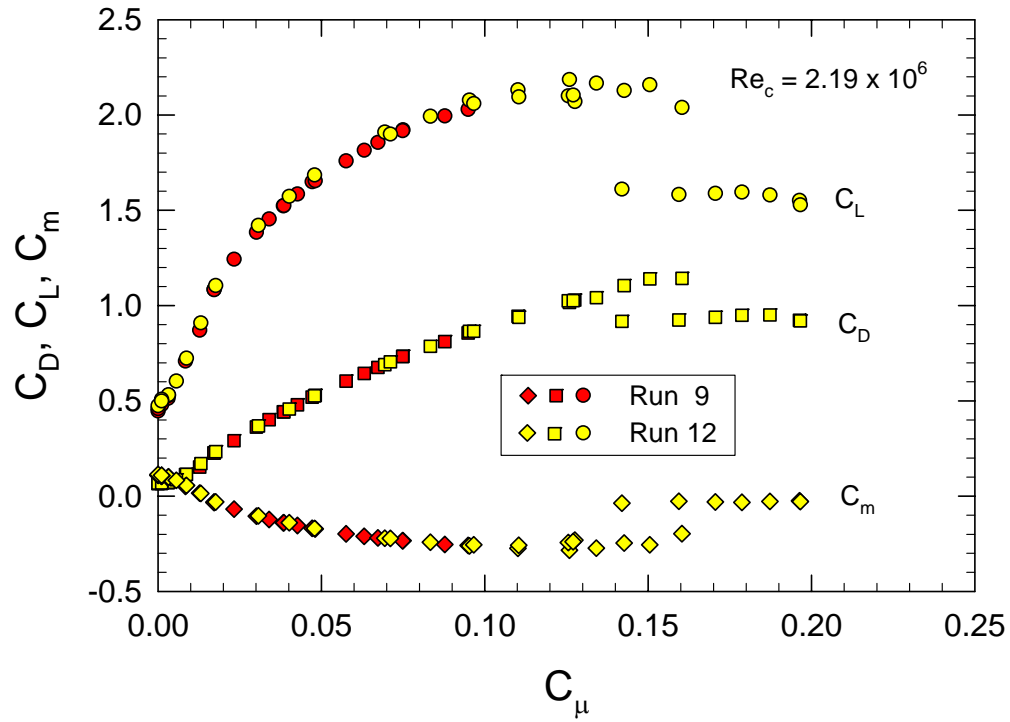


Figure 32. Force Coefficients with Upper Slot Flow at $\alpha = +10^\circ$ with Repeat Run

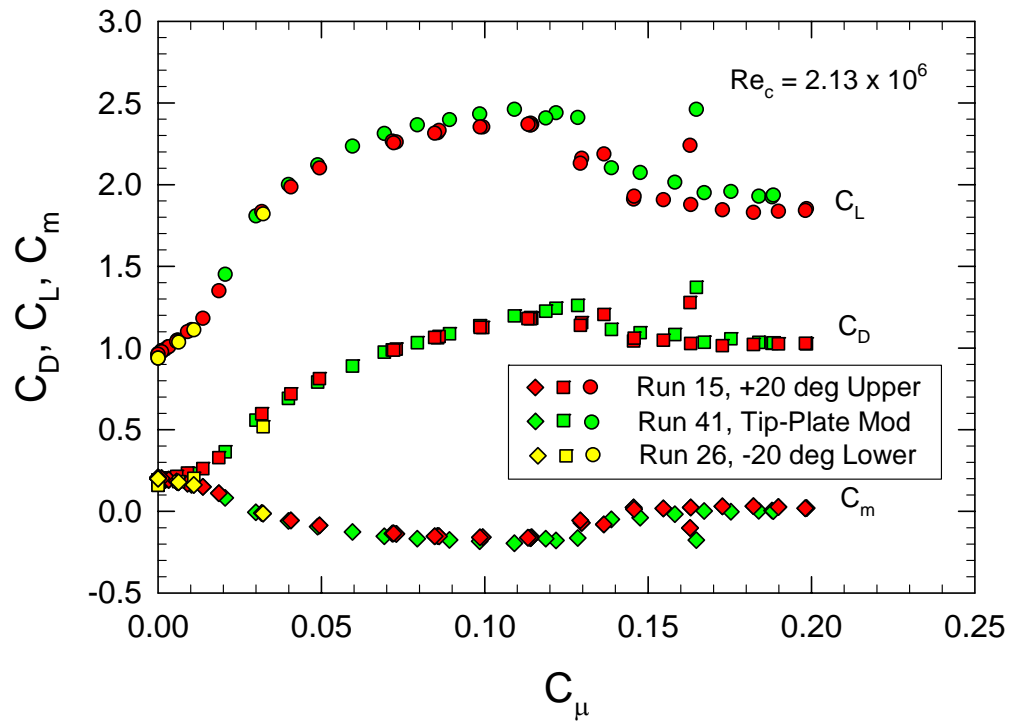


Figure 33. Force Coefficients with Upper Slot Flow at $\alpha = +20^\circ$

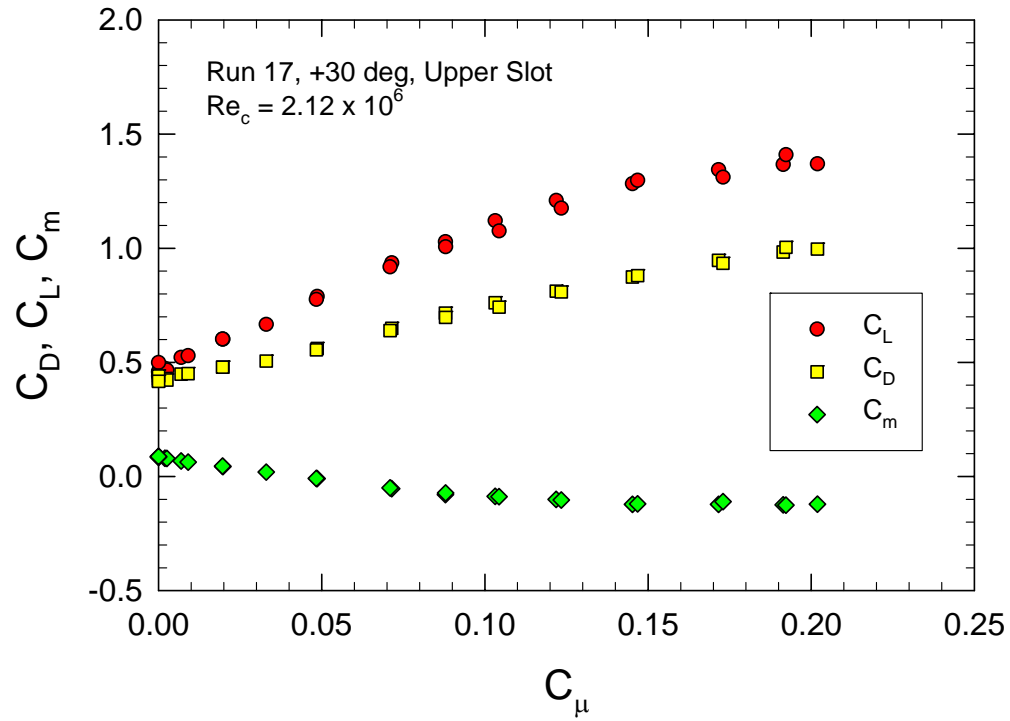


Figure 34. Force Coefficients with Upper Slot Flow at $\alpha = +30^\circ$

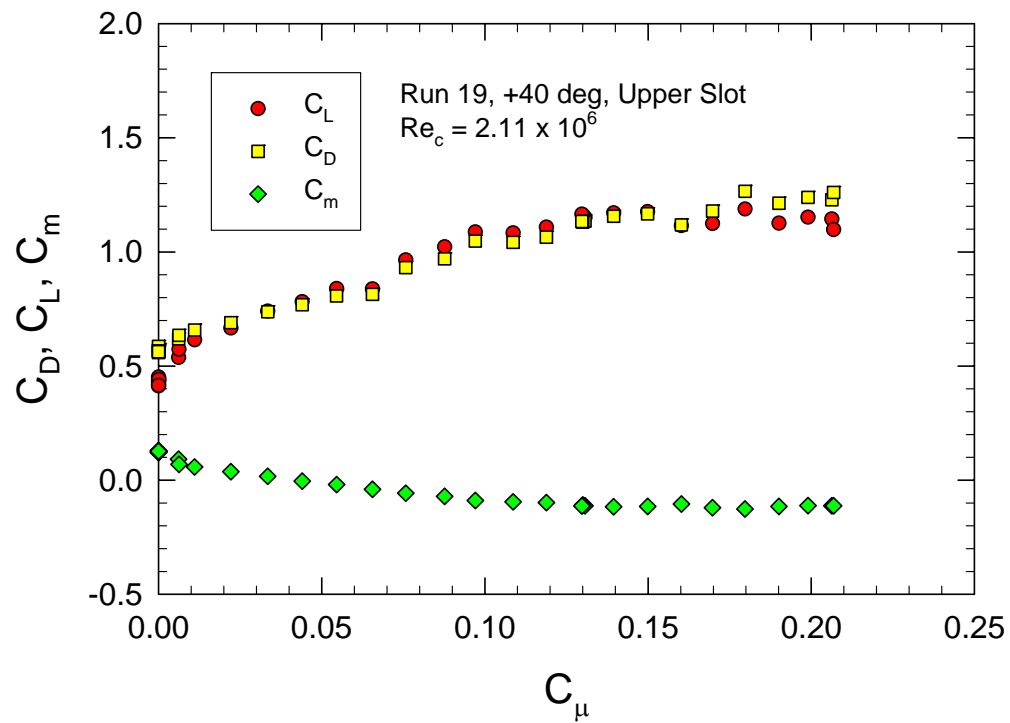


Figure 35. Force Coefficients with Upper Slot Flow at $\alpha = +40^\circ$

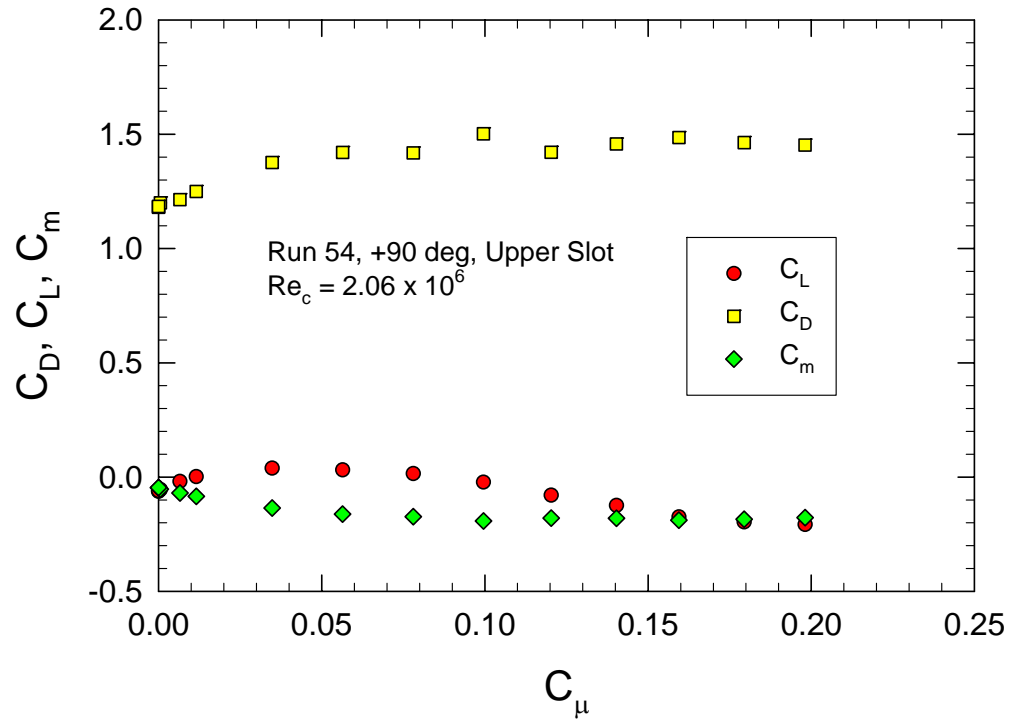


Figure 36. Force Coefficients with Upper Slot Flow at $\alpha = +90^\circ$

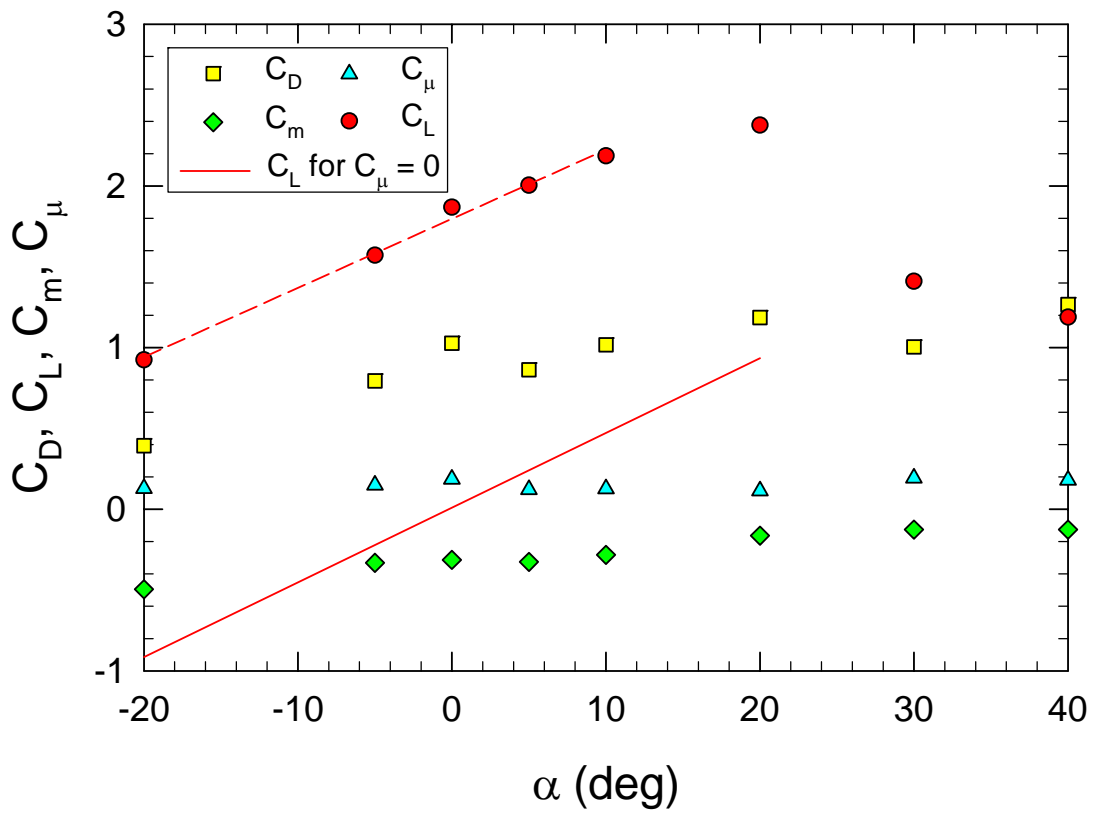
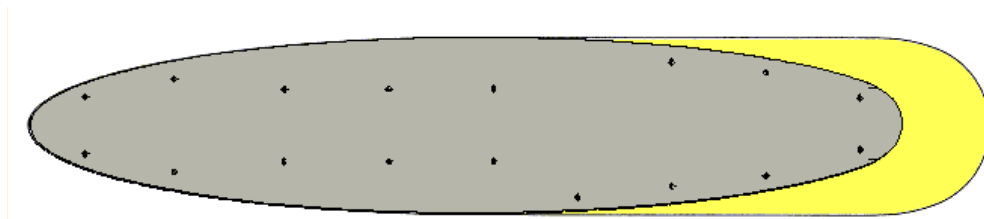


Figure 37. Force Coefficients with Upper Slot Flow at Maximum Lift



Extension of the baseline tip plate shown in yellow.

Figure 38. Modified Tip-Plate as Trailing Edge Flow Fence

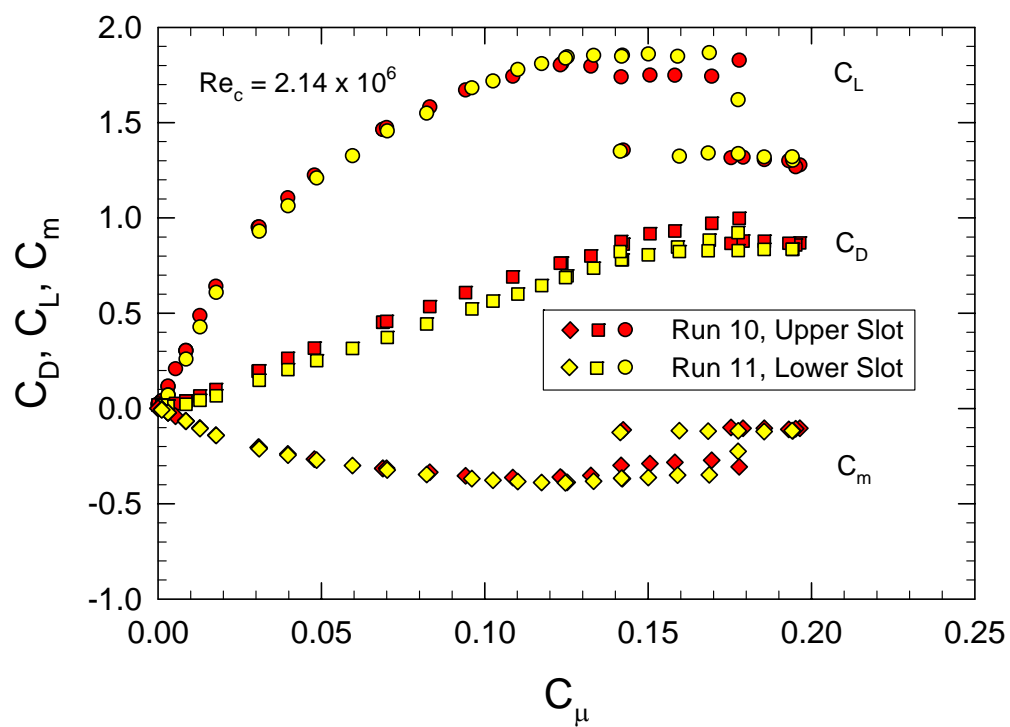


Figure 39. Force Coefficients with Lower Slot Flow at $\alpha = 0^\circ$

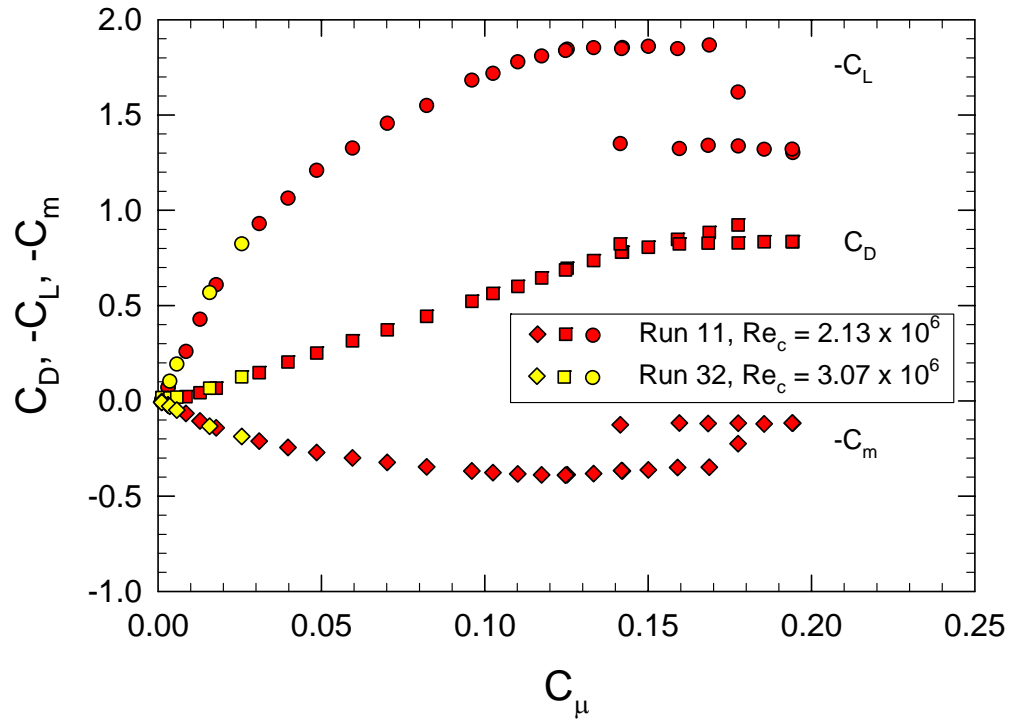


Figure 40. Force Coefficients with Lower Slot Flow at $\alpha = 0^\circ$ and 2 Re

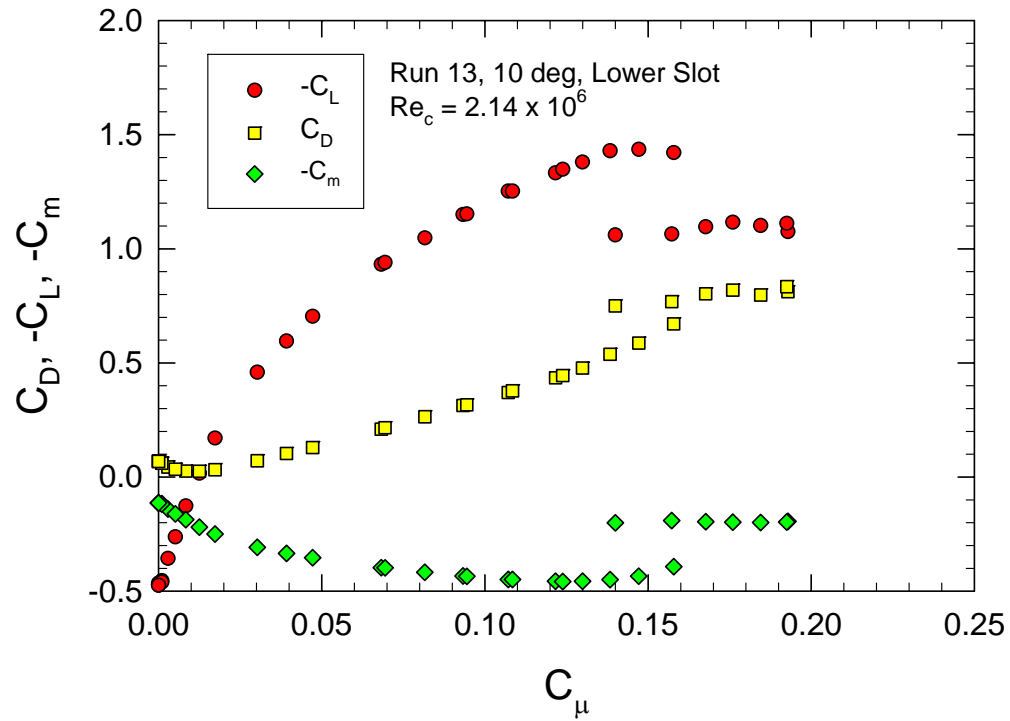


Figure 41. Force Coefficients with Lower Slot Flow at $\alpha = +10^\circ$

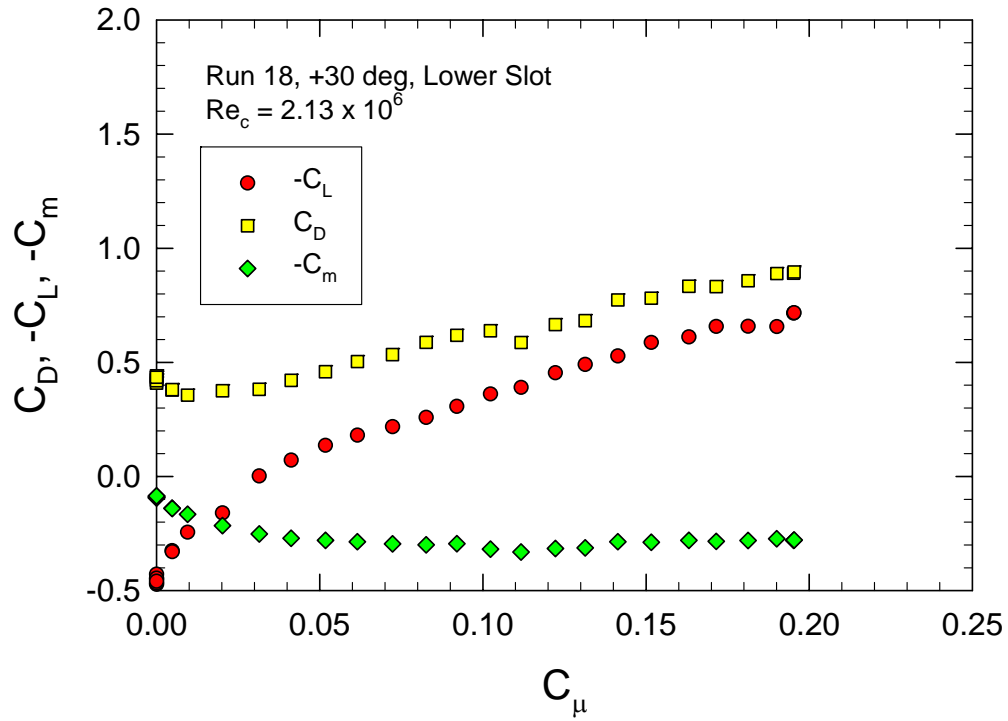


Figure 42. Force Coefficients with Lower Slot Flow at $\alpha = +30^\circ$

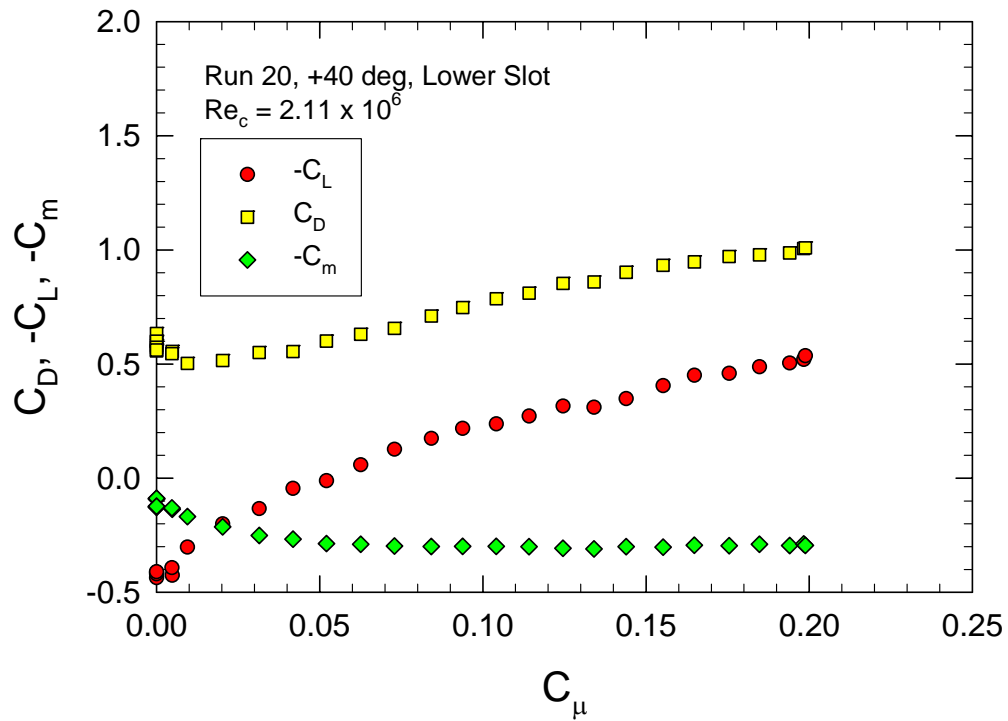


Figure 43. Force Coefficients with Lower Slot Flow at $\alpha = +40^\circ$

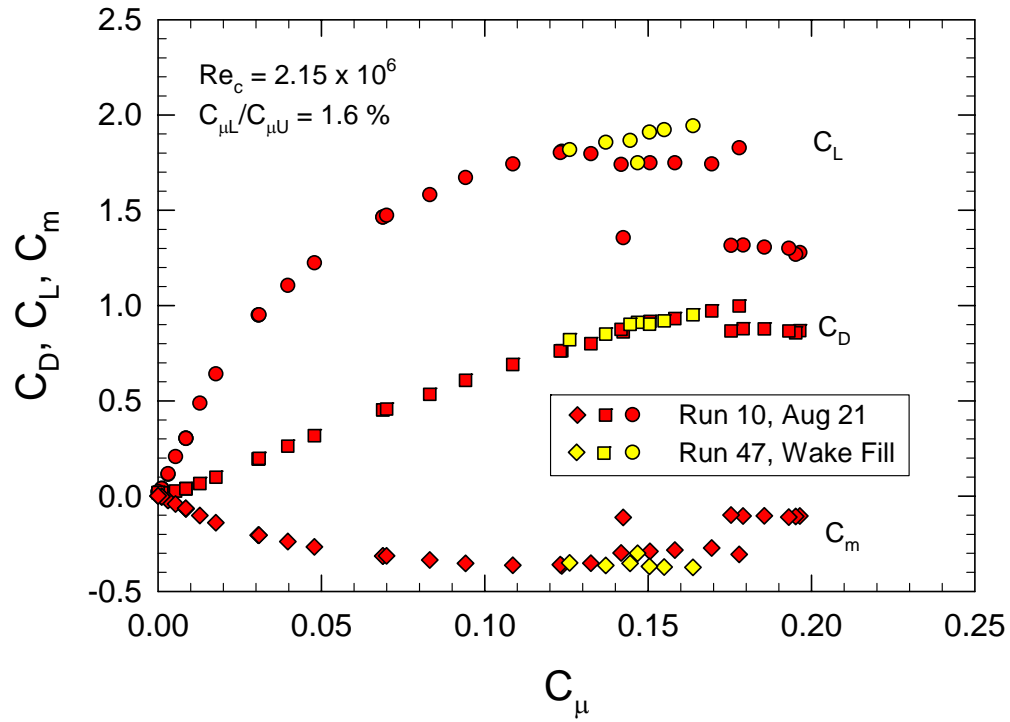


Figure 44. Force Coefficients with Upper Slot Flow at $\alpha = 0^\circ$ with Wake Fill

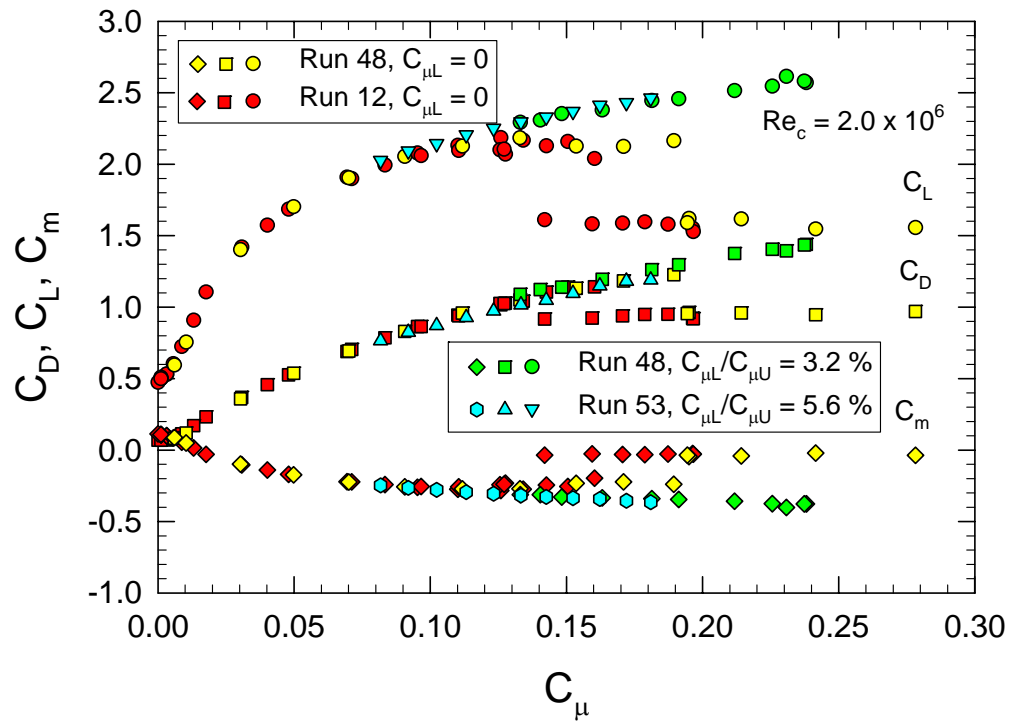


Figure 45. Force Coefficients with Upper Slot Flow at $\alpha = 10^\circ$ with 2 Wake Fills

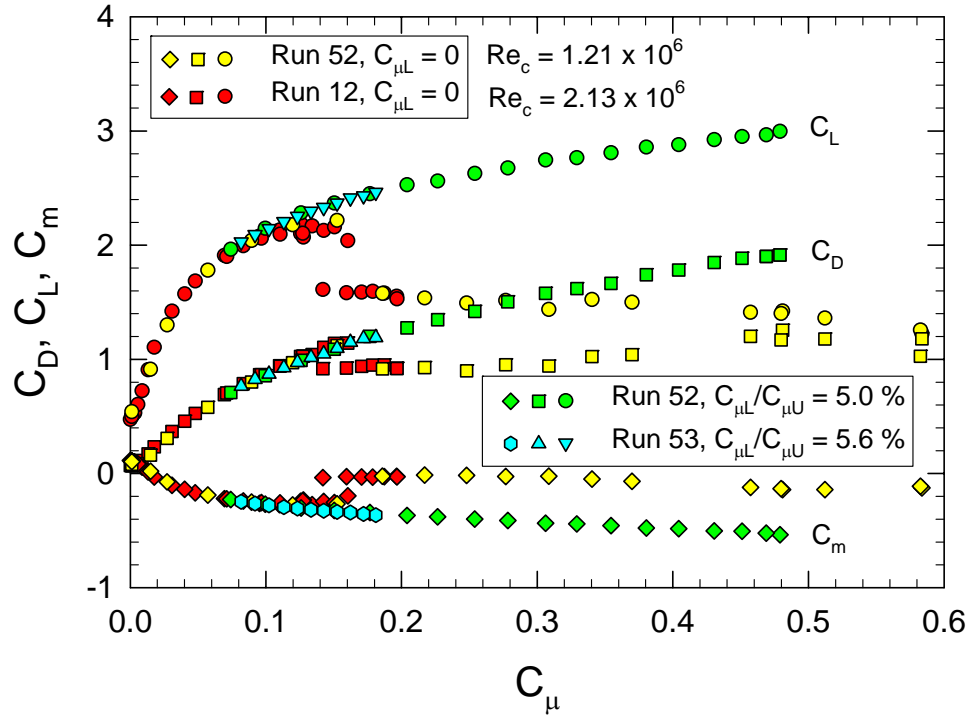


Figure 46. Force Coefficients with Upper Slot Flow, $\alpha = 10^\circ$, Wake Fill, and 2 Re

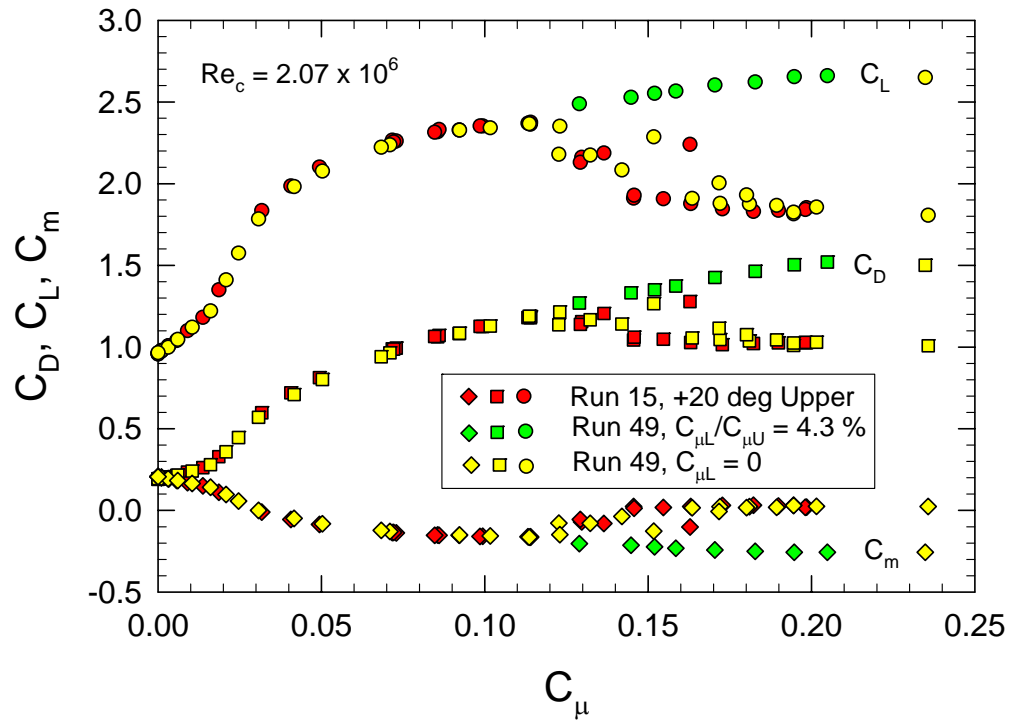


Figure 47. Force Coefficients with Upper Slot Flow at $\alpha = 20^\circ$ with Wake Fill

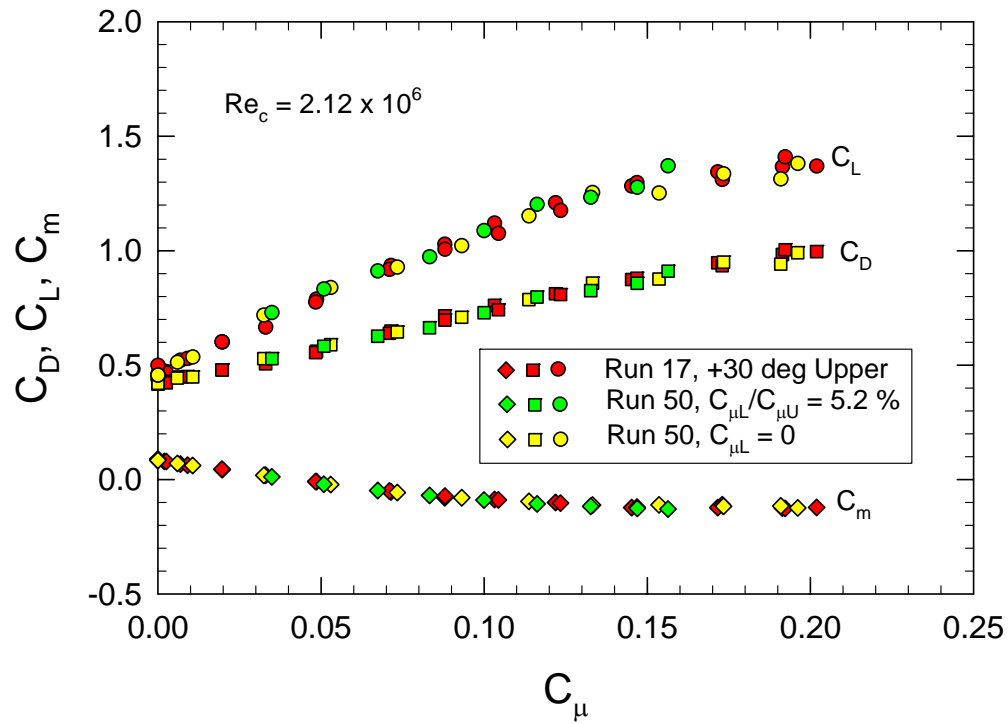


Figure 48. Force Coefficients with Upper Slot Flow at $\alpha = 30^\circ$ with Wake Fill

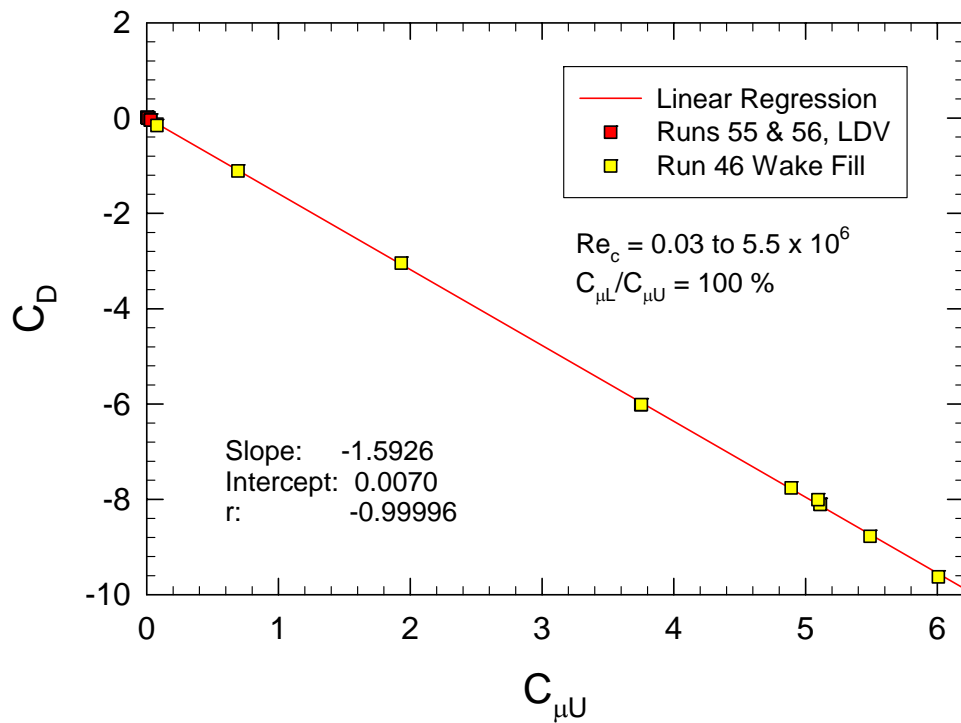


Figure 49. Drag Coefficient at $\alpha = 0^\circ$ with Equal Slot Flows

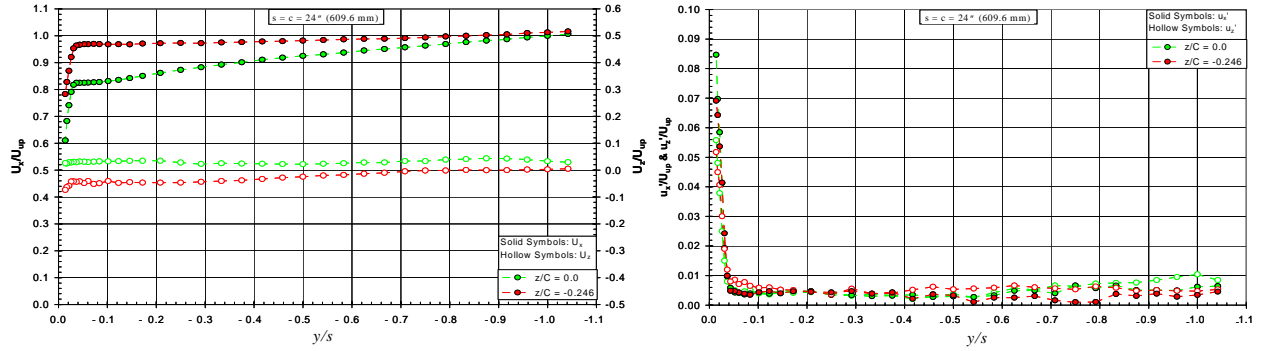


Figure 50. Spanwise Velocity Profile $x/c = -0.083$ Upstream of CC Foil

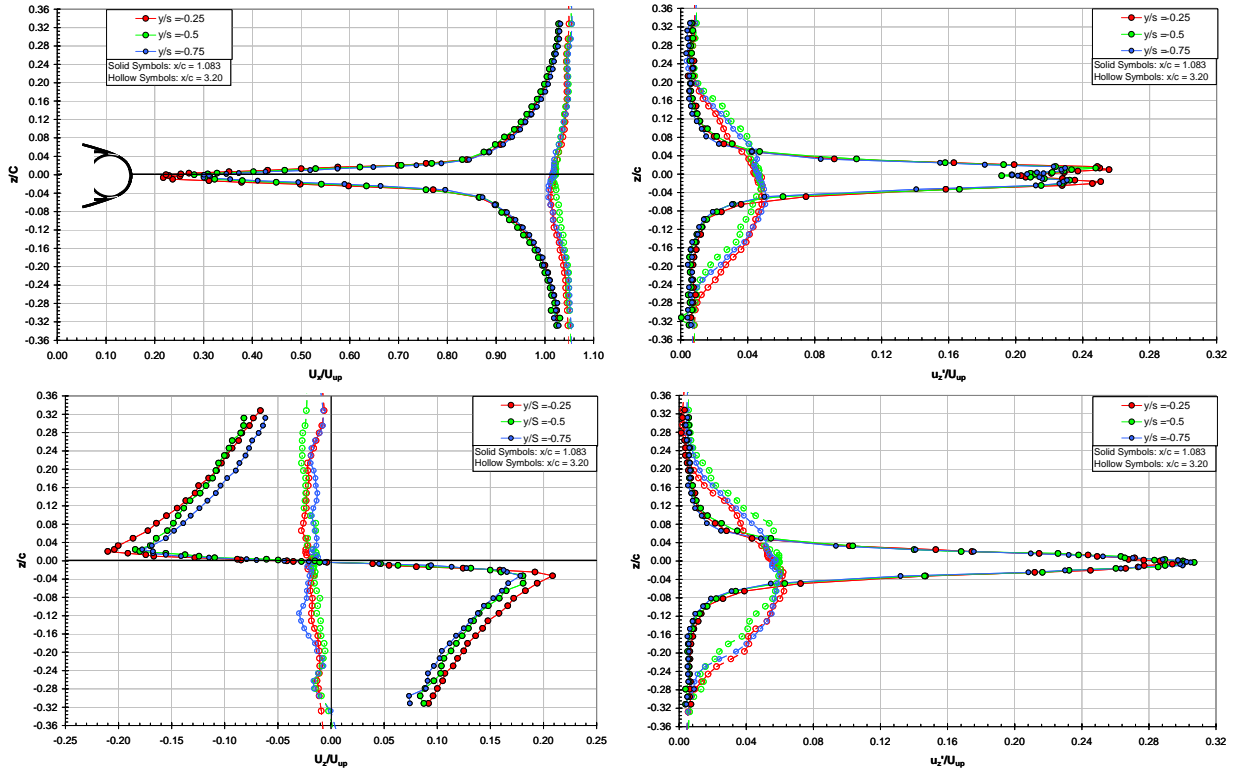


Figure 51. Wake Velocity Profiles with No Slot Flow and $Re = 2.2 \times 10^6$

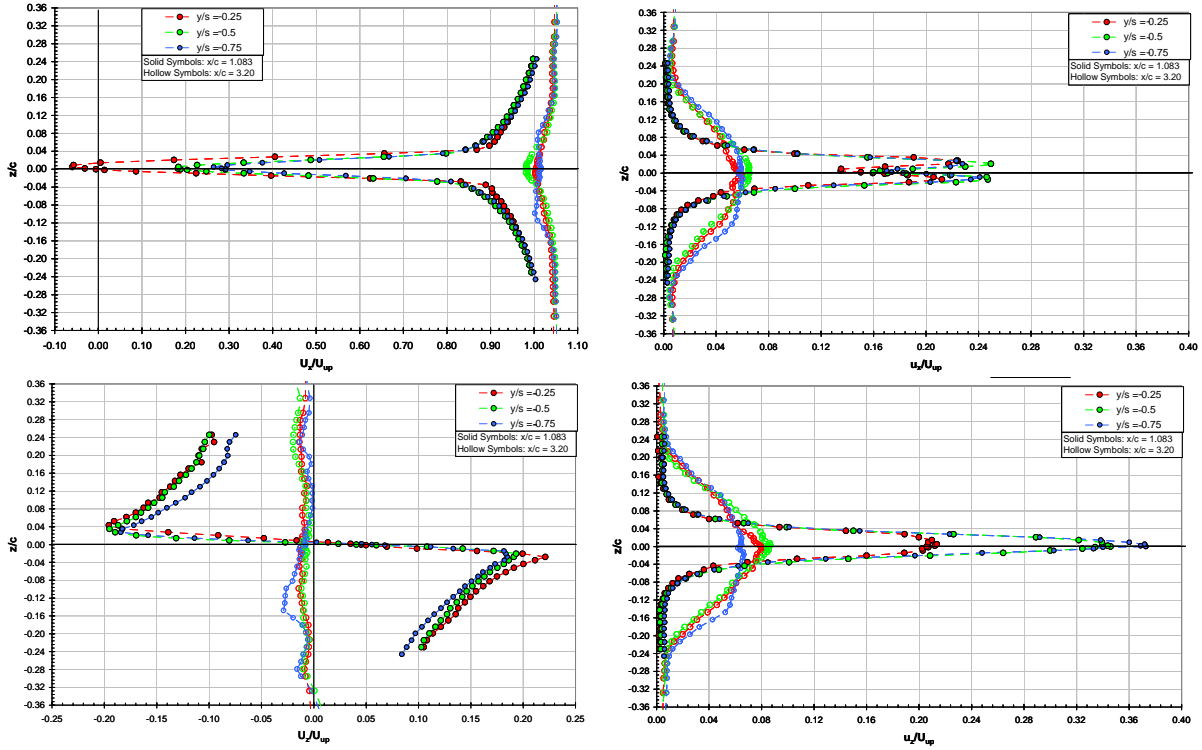


Figure 52. Wake Velocity Profiles with No Slot Flow and $Re = 5.5 \times 10^6$

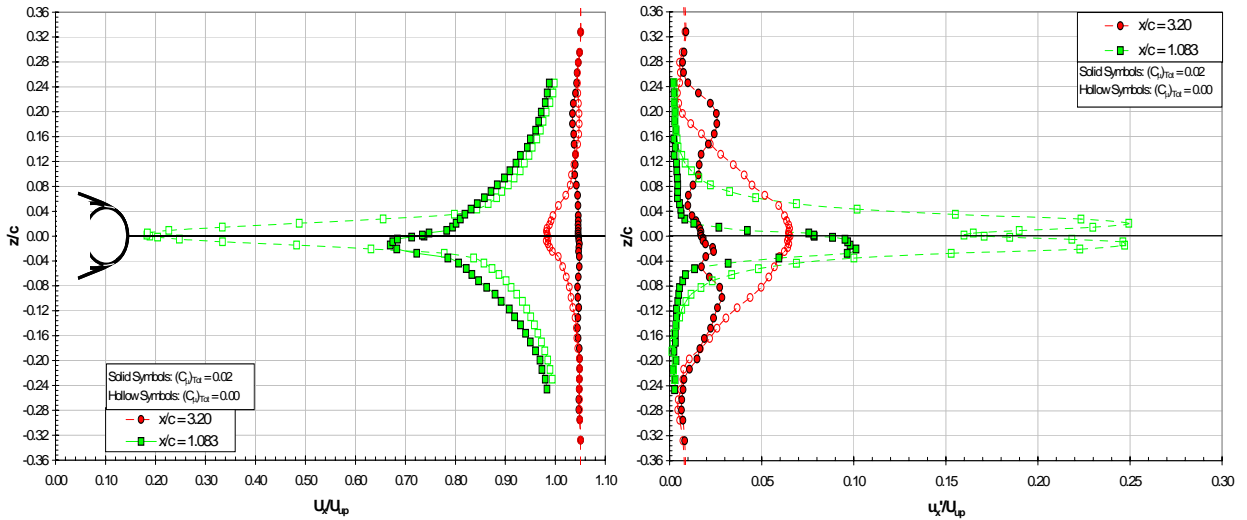


Figure 53. Wake Filling for "Zero Thrust" at $y/s = -0.5$ at $Re = 2.2 \times 10^6$

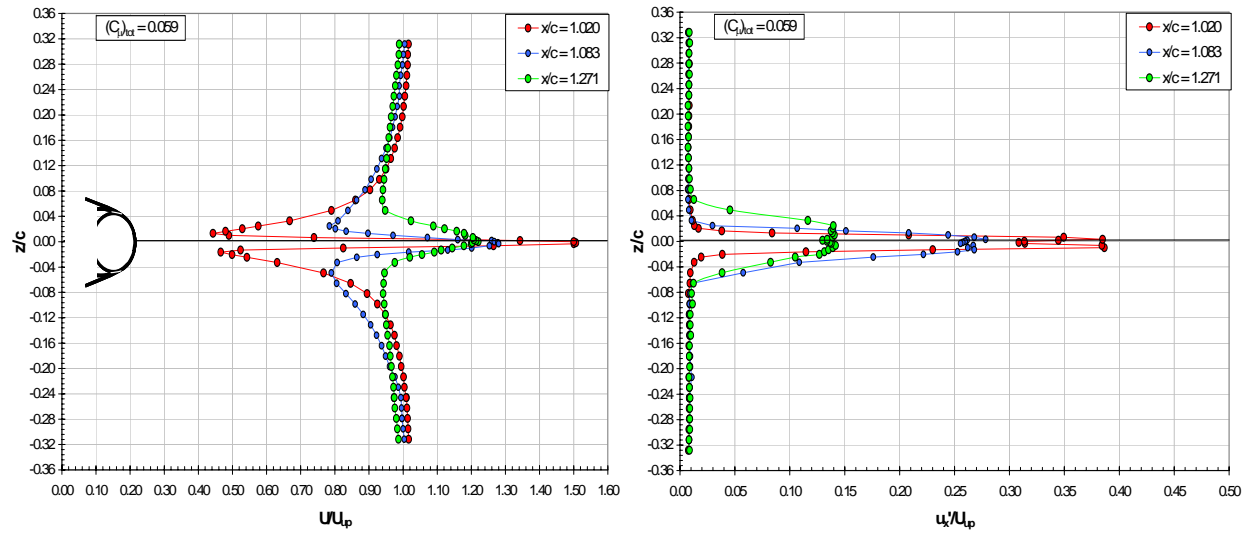


Figure 54. Axial Variation of Wake Profiles for "Positive Thrust" at $y/s = -0.25$

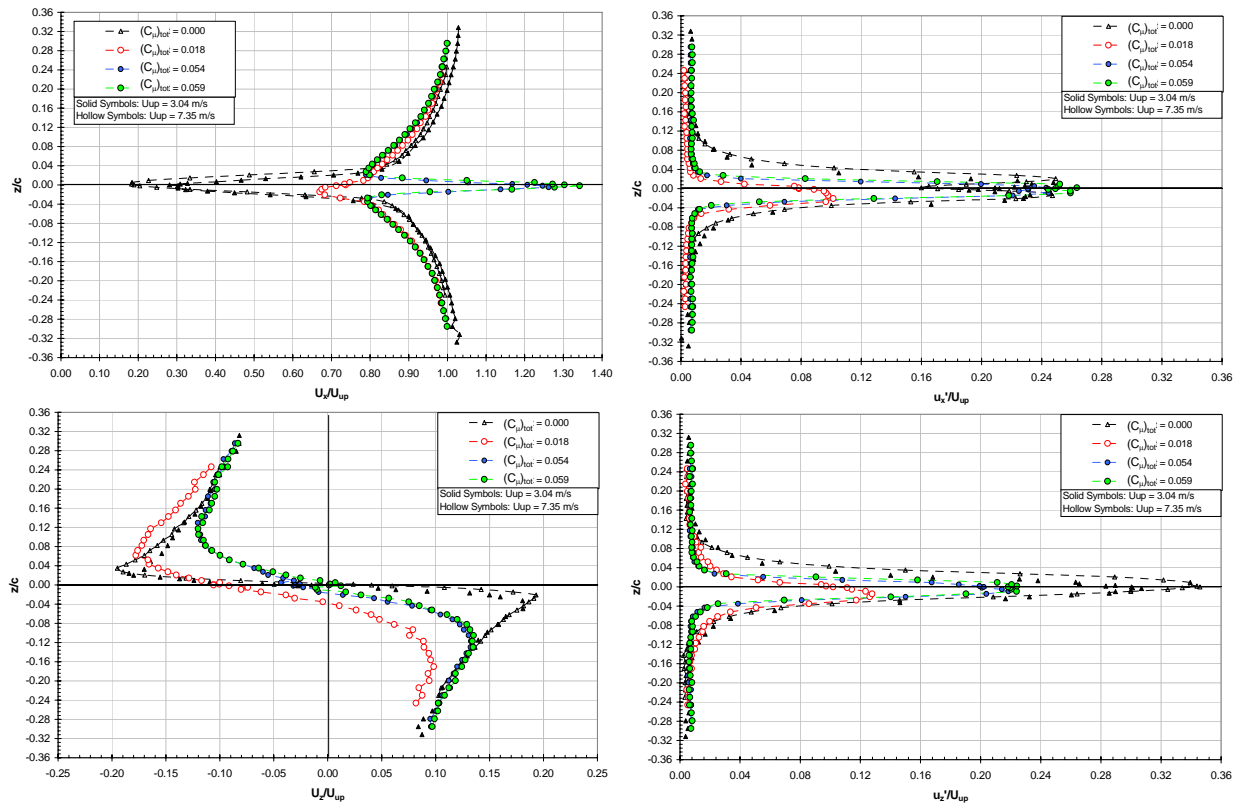


Figure 55. Wake Profiles for Various Slot Flows at $x/c = 1.083$ and $y/s = -0.5$

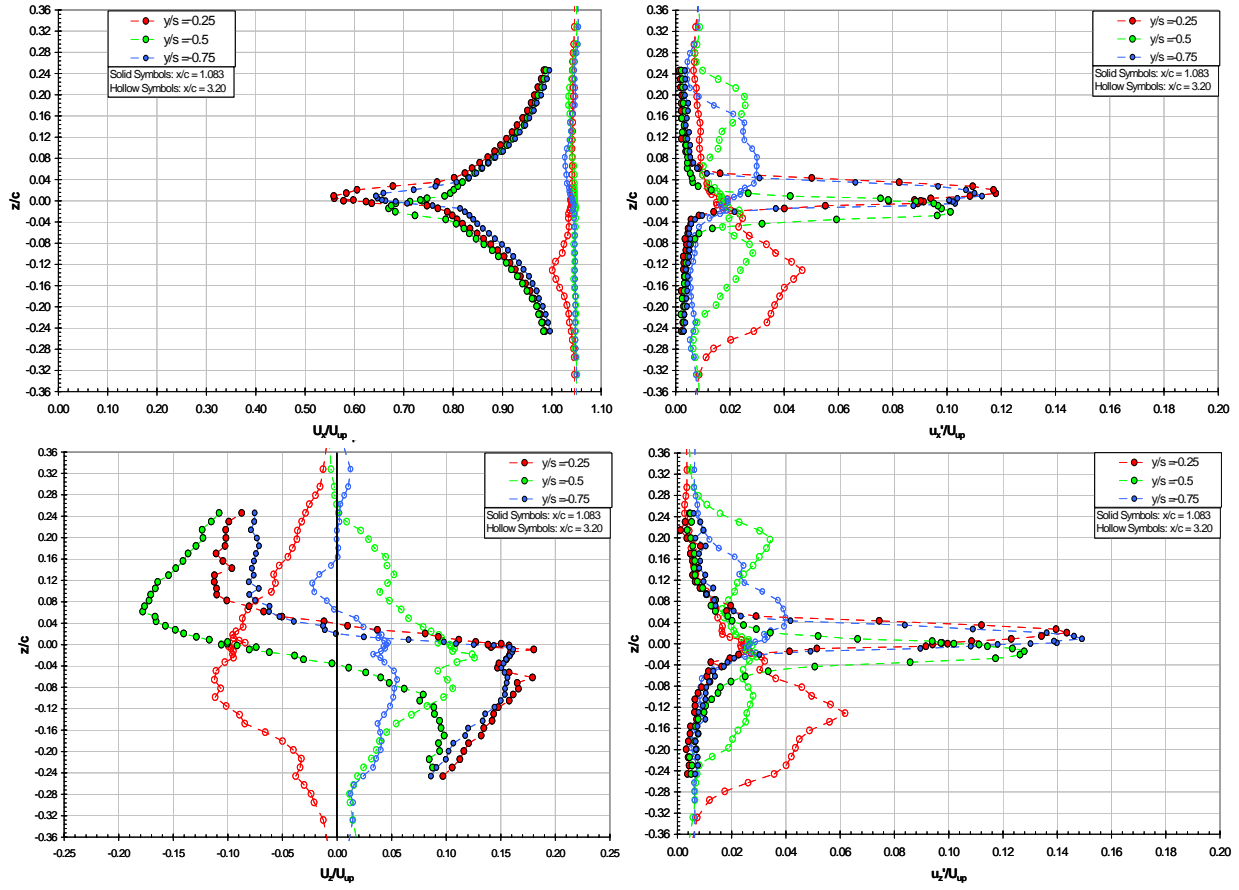


Figure 56. Spanwise Uniformity of Wake Profiles for Zero Thrust, $Re = 5.5 \times 10^6$

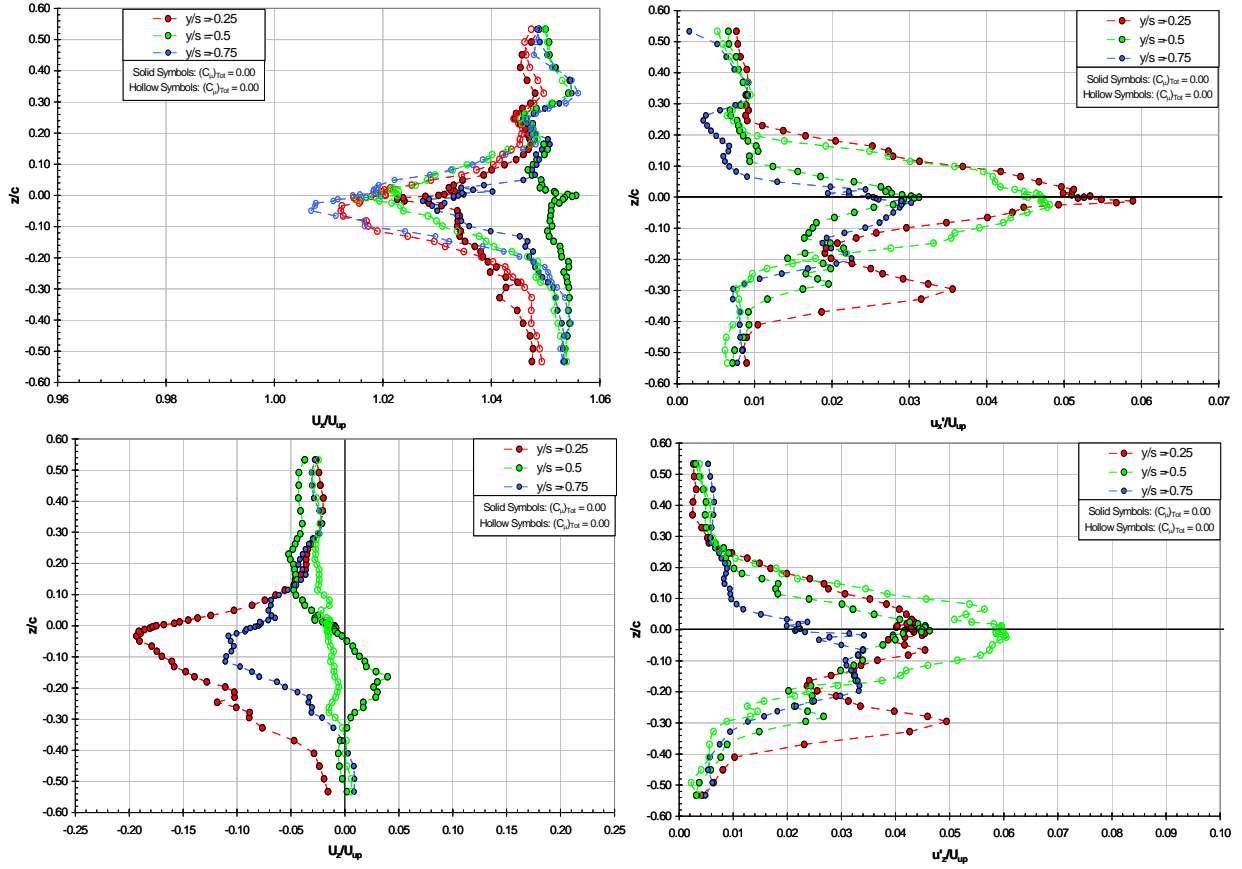


Figure 57. Spanwise Uniformity of Wake Profiles, $C_{\mu Tot} = 0.059$, $Re = 2.2 \times 10^6$

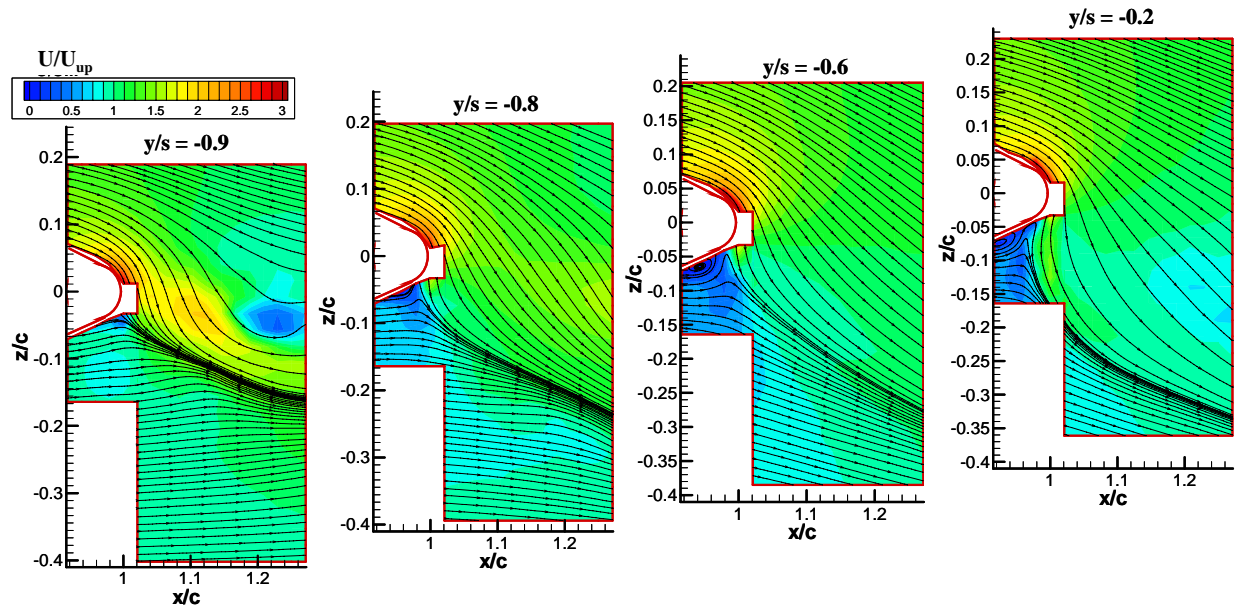


Figure 58. Velocity Contours at Various Spanwise Locations for $C_{\mu U} = 0.07$ and $C_{\mu L} = 0.00$ at $Re = 2.2 \times 10^6$

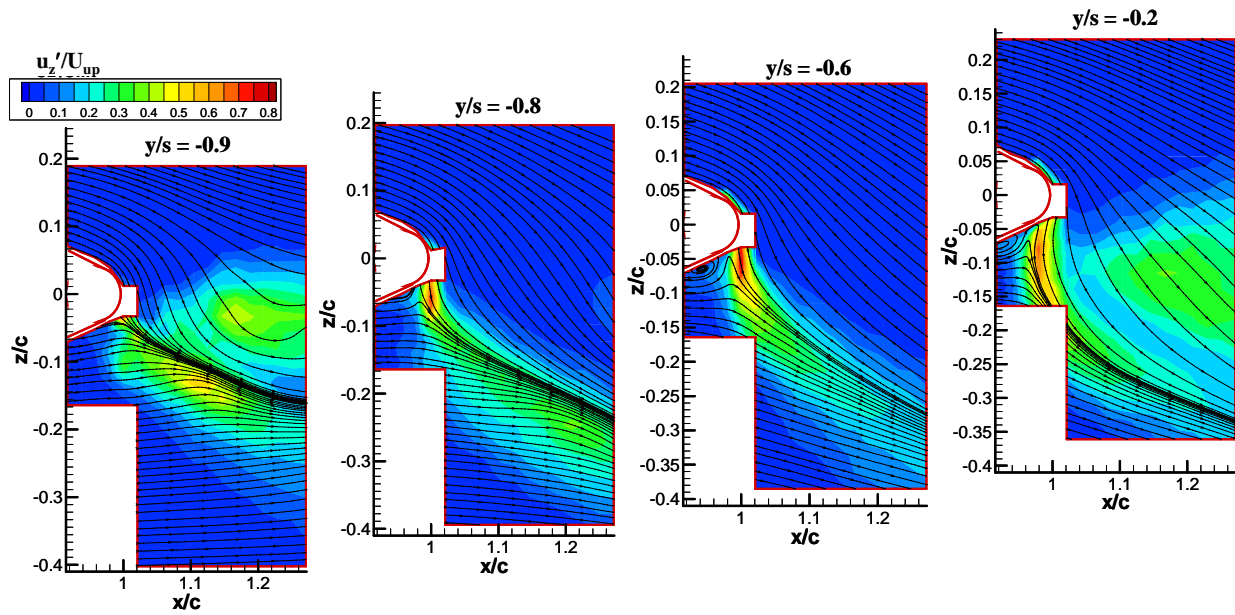


Figure 59. Relative Turbulence Contours Indicating Jet Location at various Spanwise Locations for $C_{\mu U} = 0.07$ and $C_{\mu L} = 0.00$ at $Re = 2.2 \times 10^6$

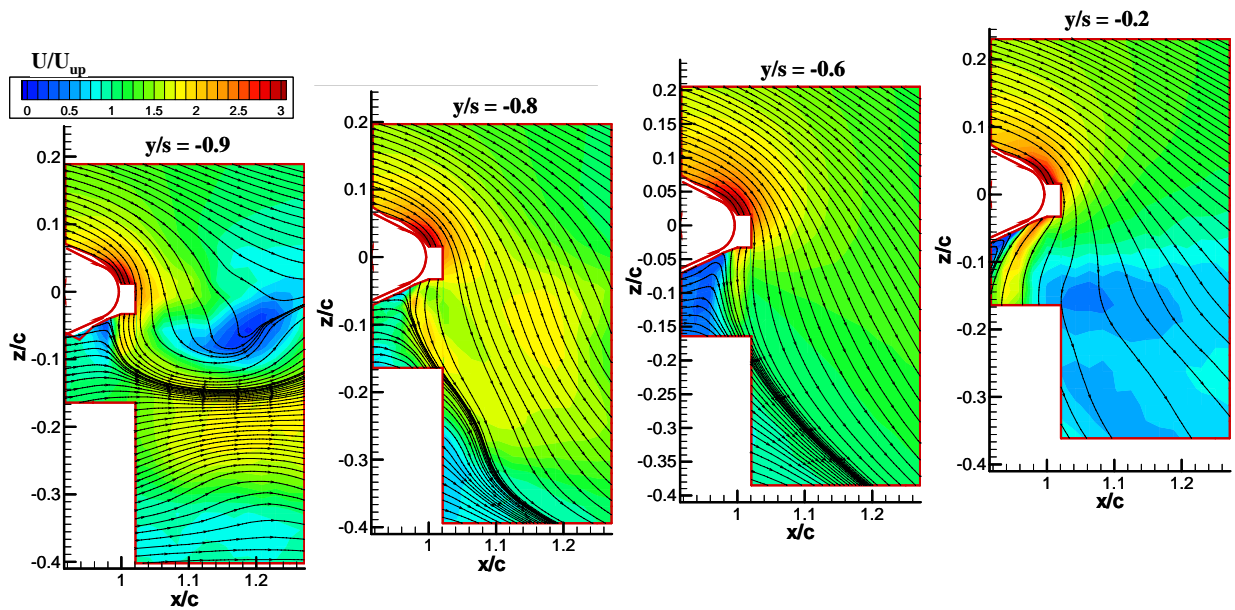


Figure 60. Velocity Contours at Various Spanwise Locations for $C_{\mu U} = 0.15$ and $C_{\mu L} = 0.0035$ at $Re = 2.1 \times 10^6$

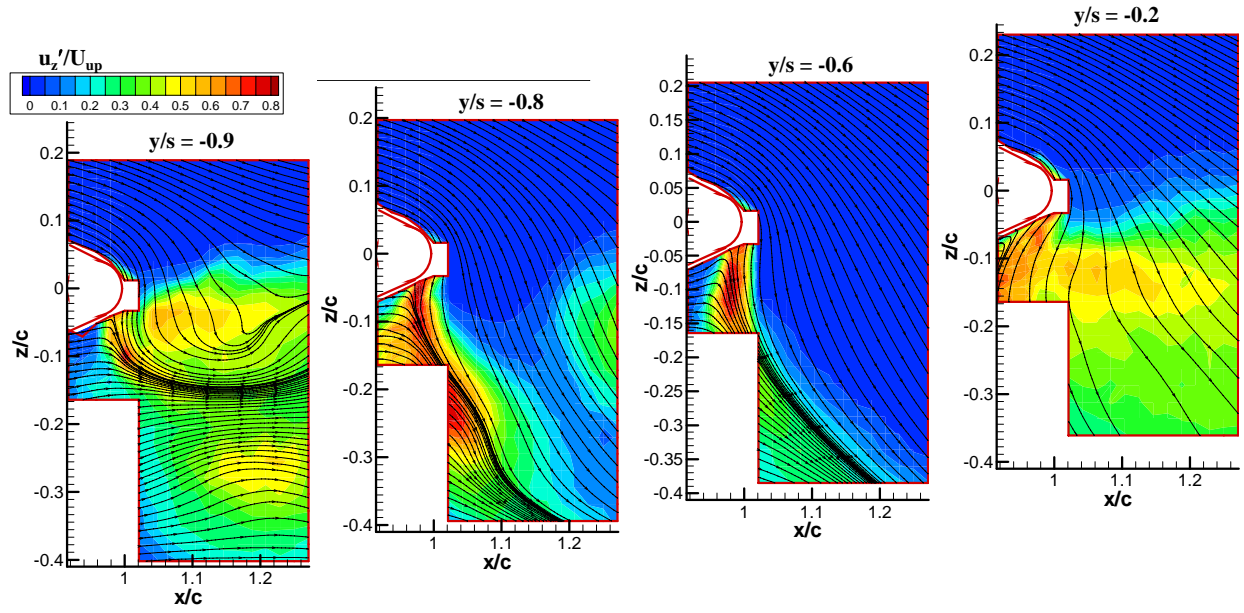


Figure 61. Relative Turbulence Contours Indicating Jet Location at Various Spanwise Locations for $C_{\mu U} = 0.15$ and $C_{\mu L} = 0.0035$ at $Re = 2.1 \times 10^6$

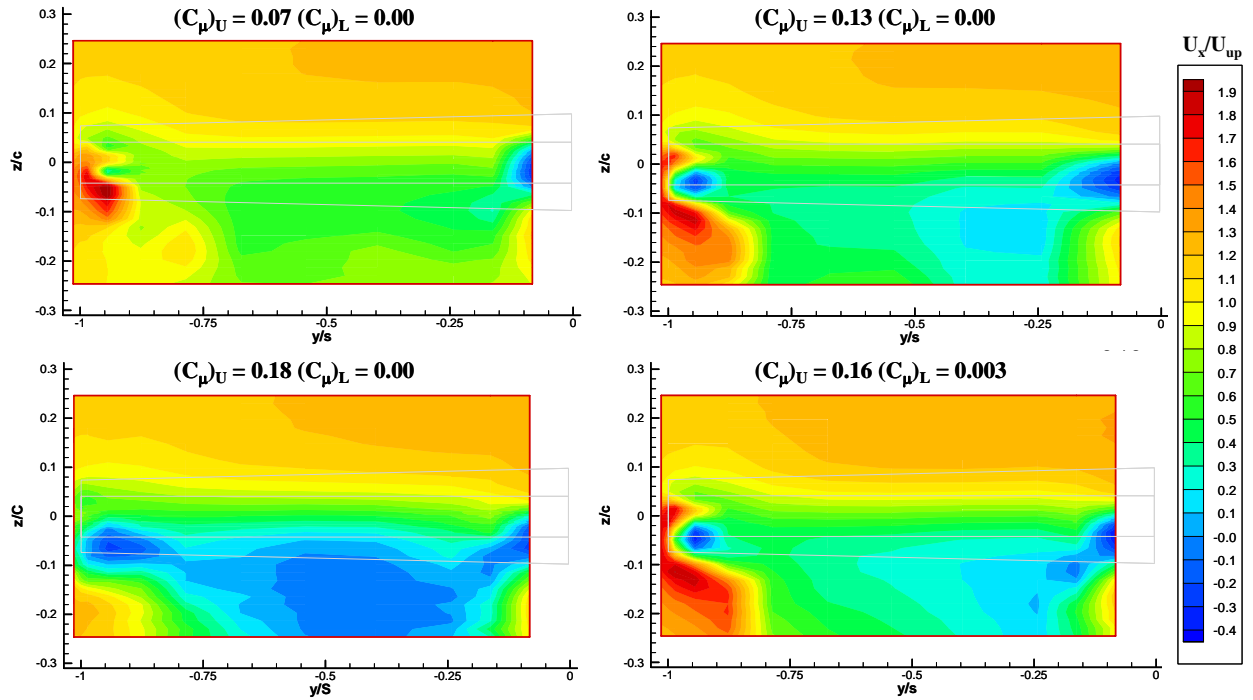


Figure 62. Axial Velocity Contours for Various Slot Flows at $x/c = 1.083$ and $Re = 2.2 \times 10^6$

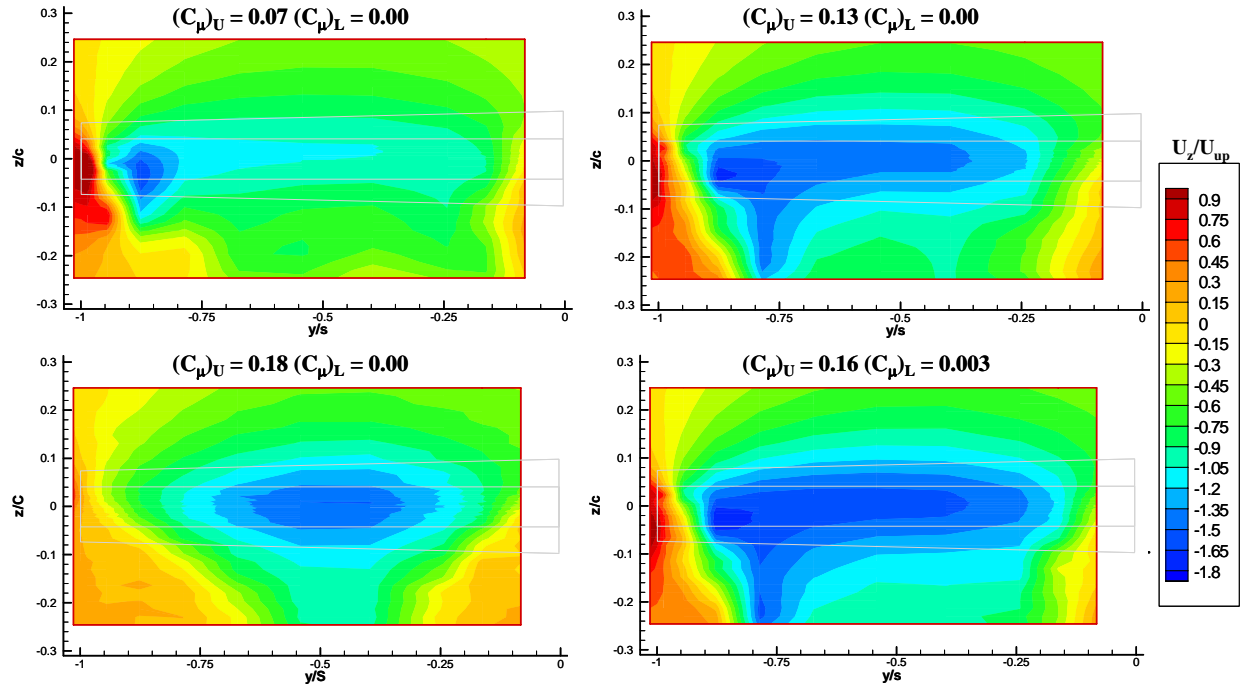


Figure 63. Vertical Velocity Contours for Various Slot Flows at $x/c = 1.083$ and $Re = 2.2 \times 10^6$

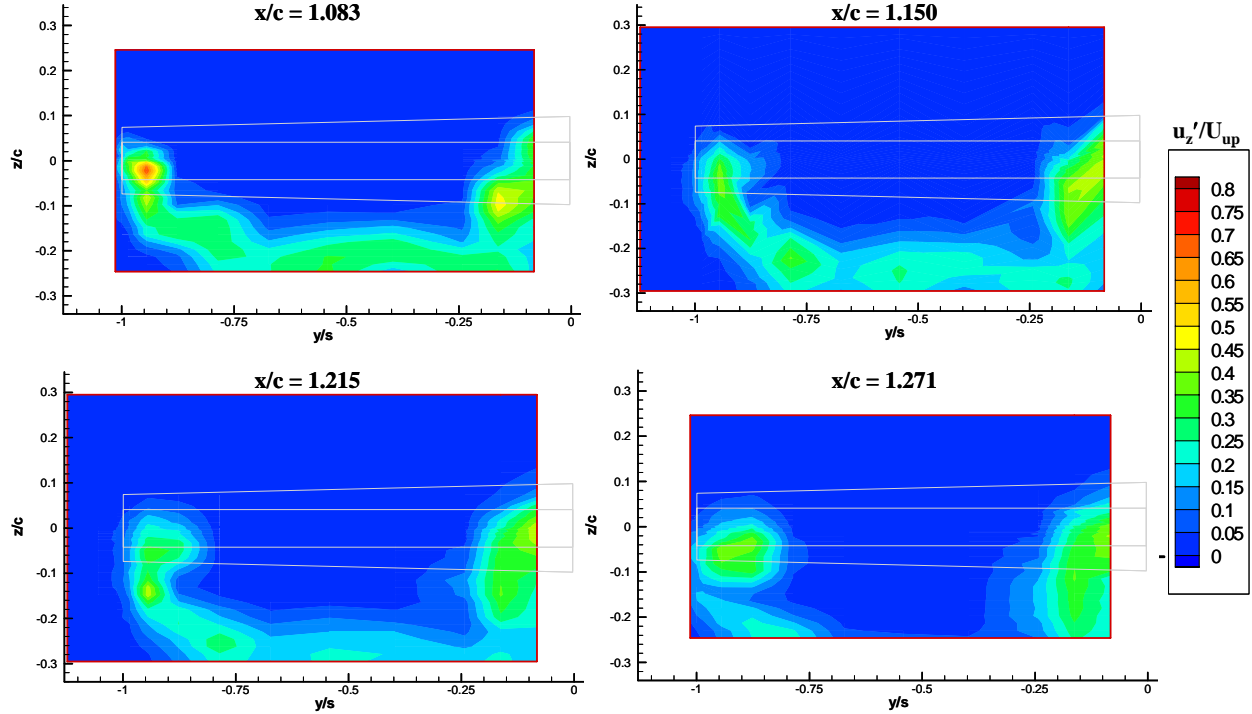


Figure 64. Relative Turbulence Levels at Various Axial Locations for $C_{\mu U} = 0.07$ and $C_{\mu L} = 0.00$ with $Re = 2.2 \times 10^6$

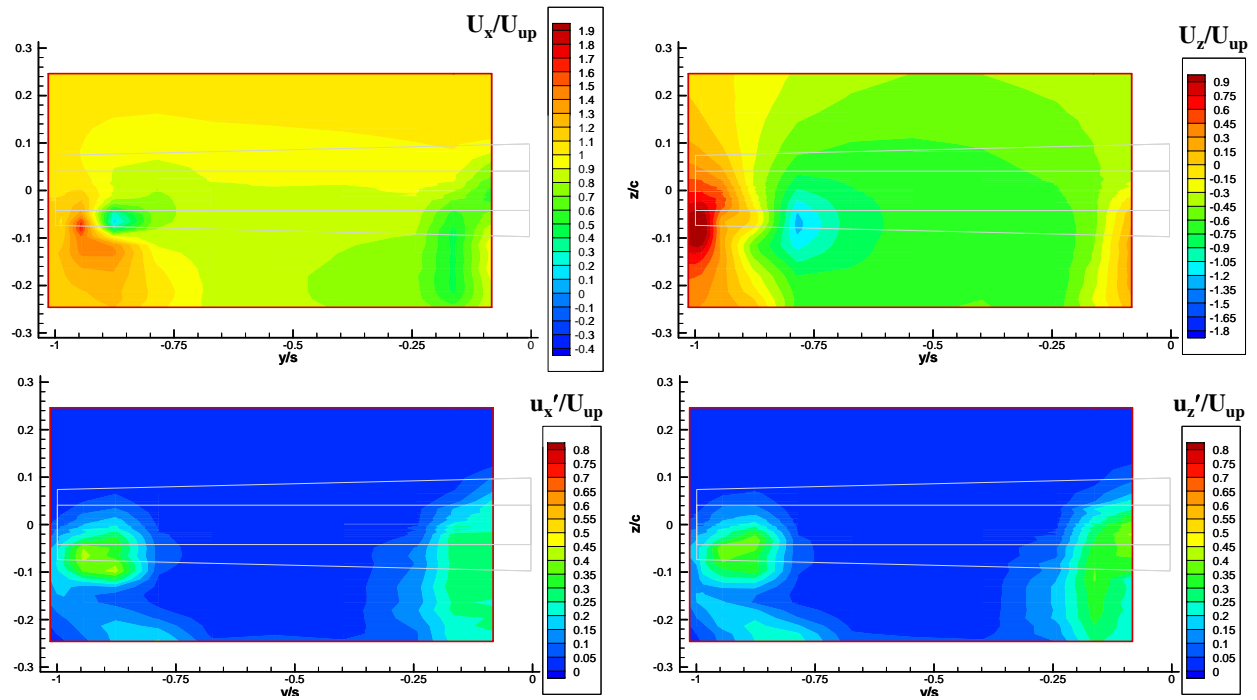


Figure 65. Velocity and Turbulence Contours at $x/c = 1.271$ for $C_{\mu U} = 0.07$ and $C_{\mu L} = 0.00$ with $Re = 2.2 \times 10^6$

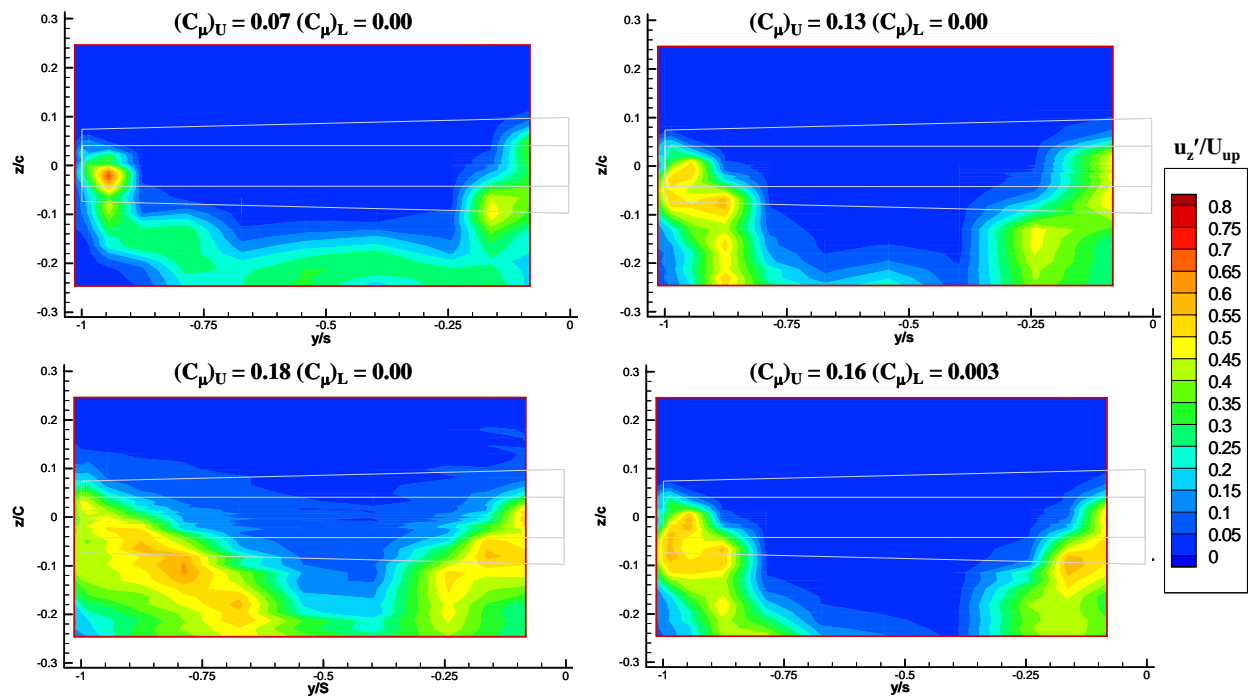


Figure 66. Relative Turbulence Levels for Various Slot Flows at $x/c = 1.083$ and $Re = 2.2 \times 10^6$

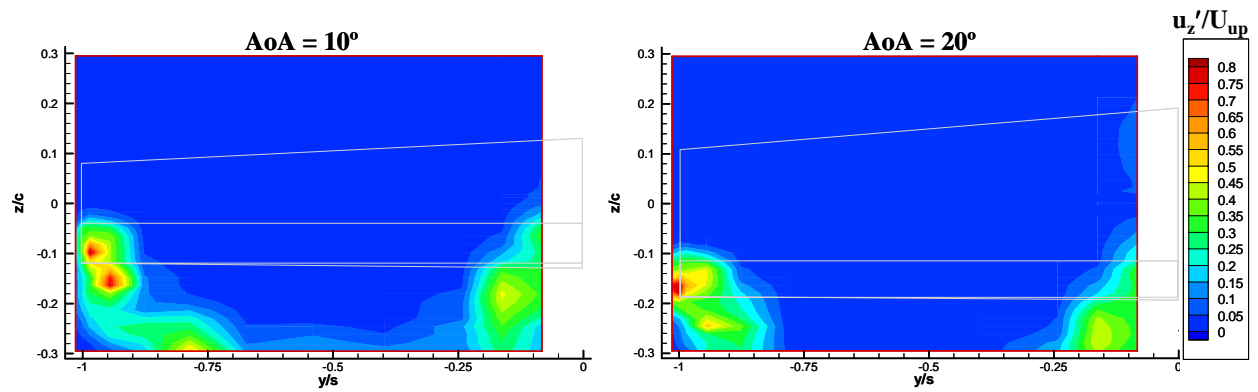


Figure 67. Relative Turbulence Levels for Various Angles of Attack at $x/c = 1.083$ for $C_{\mu U} = 0.07$ and $C_{\mu L} = 0.00$ with $Re = 2.2 \times 10^6$

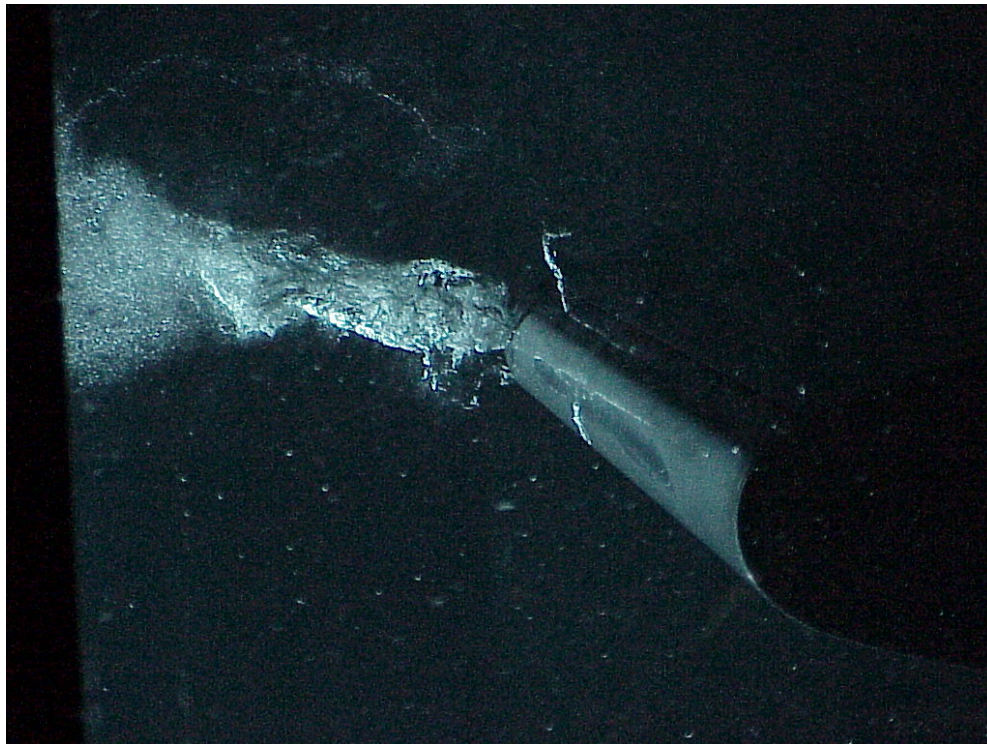


Figure 68. Vortex cavitation, tip and lightning vortex at 80% span

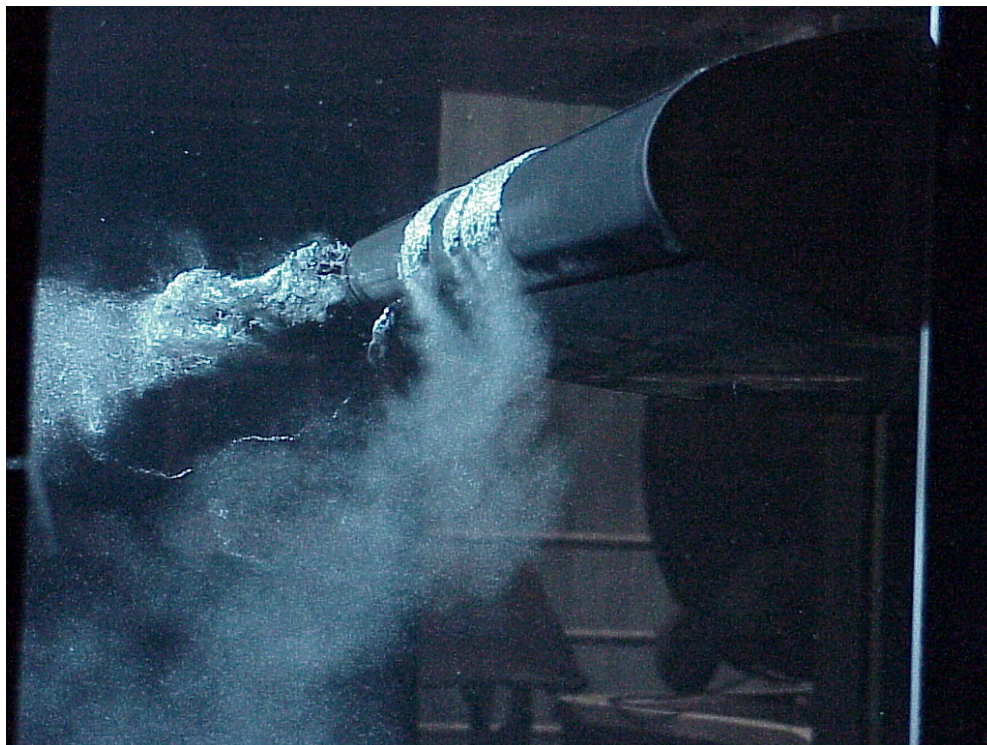


Figure 69. Cavitation on CCfoil, upper slot blowing, Coanda surface, tip vortex, and lightning vortex at 80% span shown.

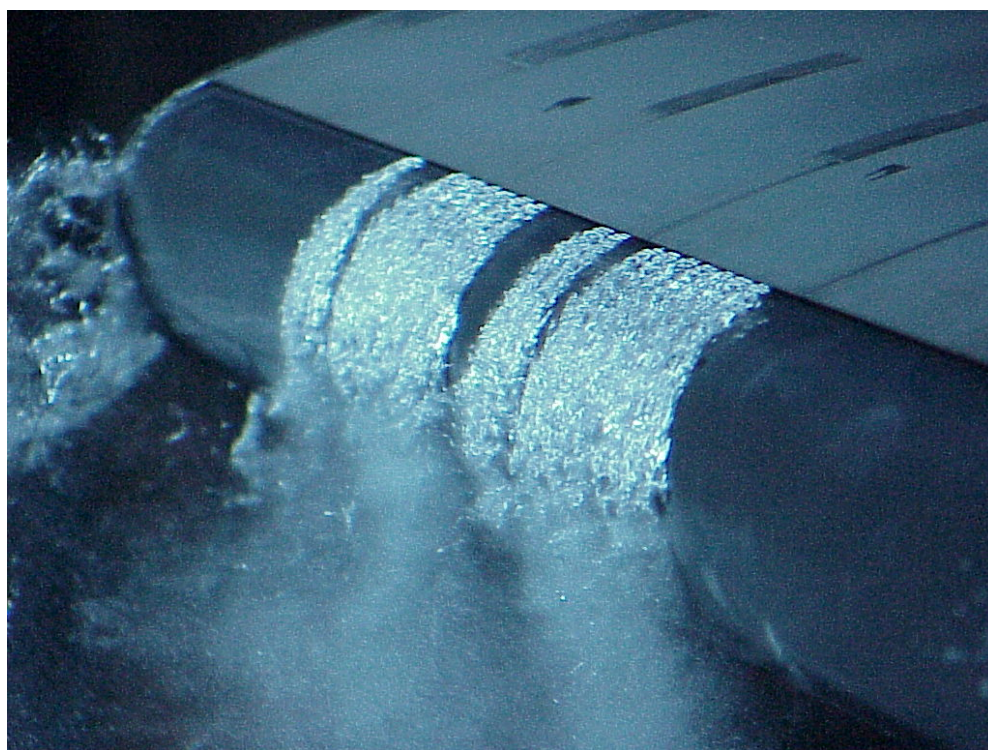


Figure 70. Surface cavitation on Coanda Surface, close-up of the slot flow, inception behind slot lip face.

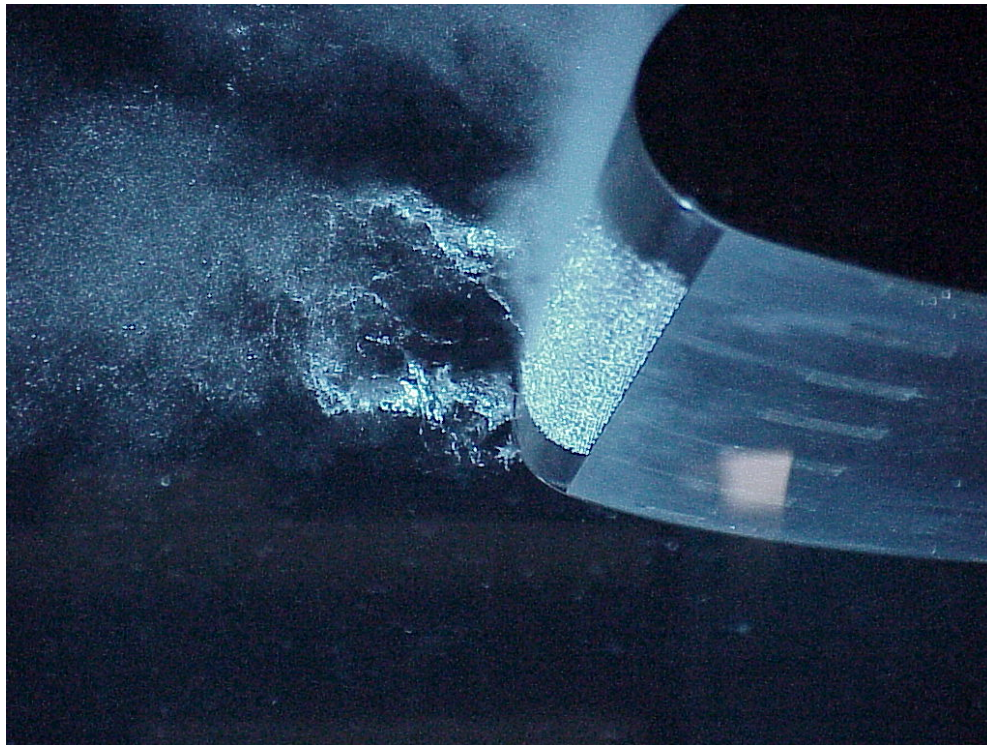


Figure 71. Surface Cavitation on Coanda Surface, lower slot blowing.

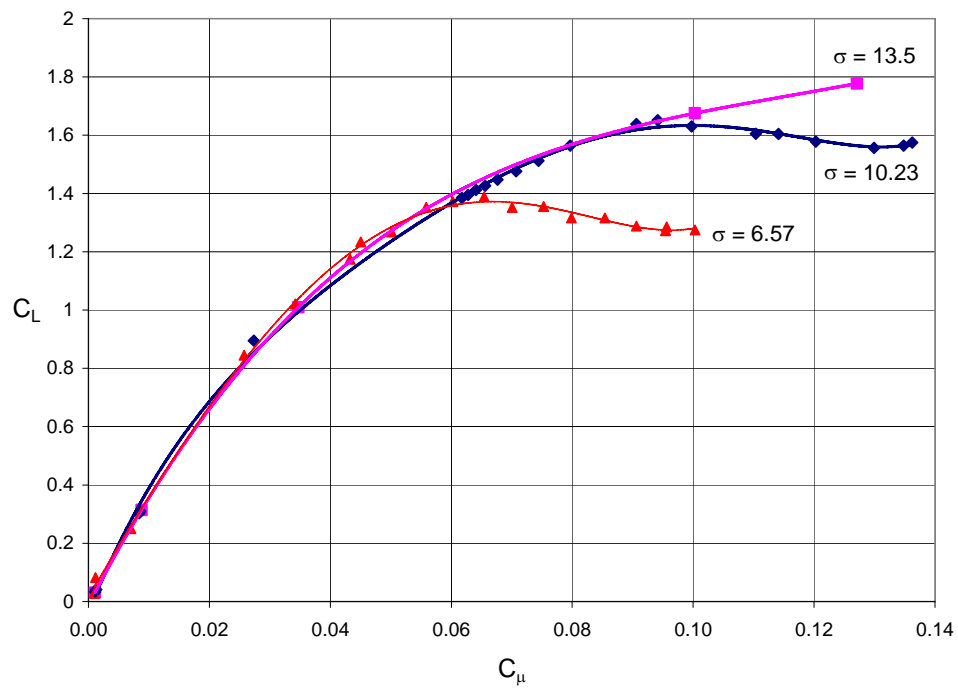


Figure 72. Lift response to cavitation development on the Coanda surface

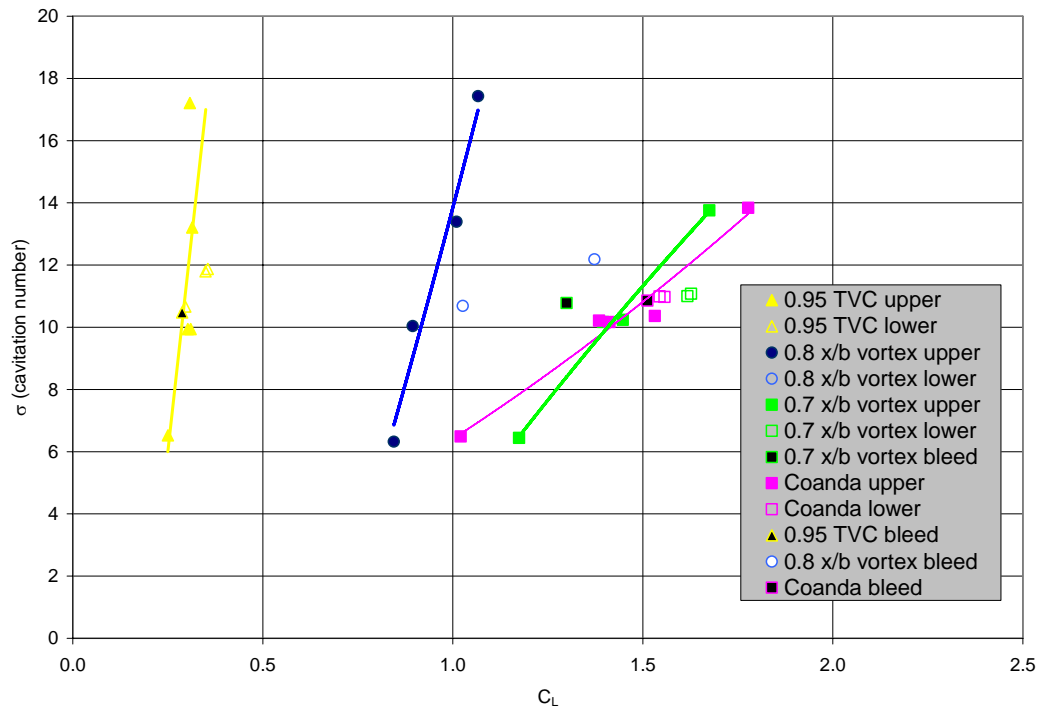


Figure 73. Cavitation inception diagram at 0 degrees AOA

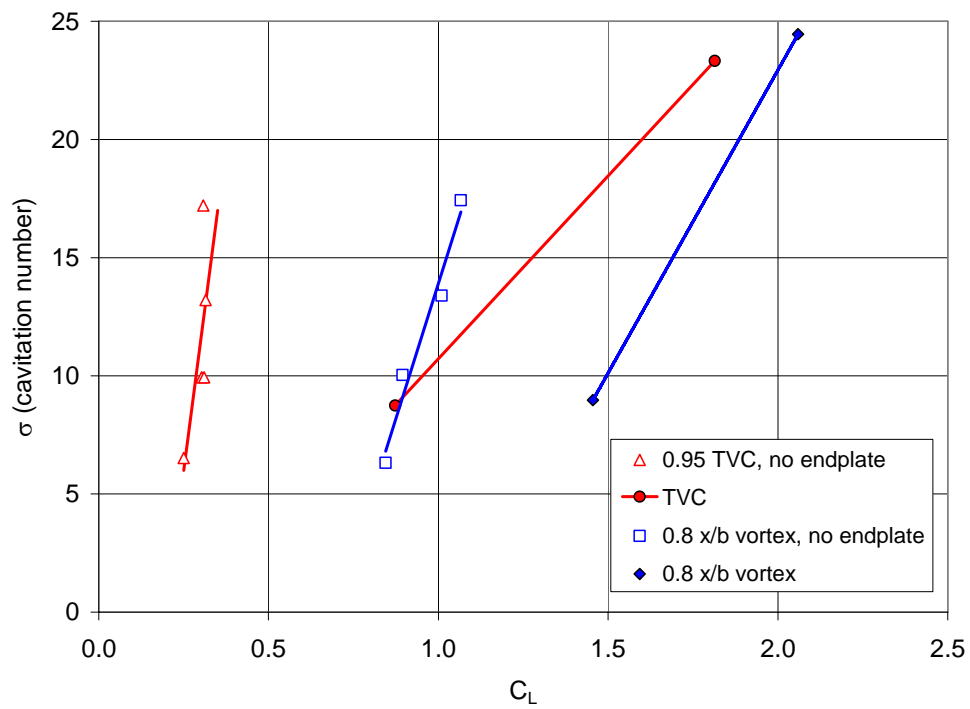


Figure 74. Impact of endplate on vortex cavitation inception.

Table 1. Channel List for Data Acquisition System

Chan. No.	Name	Manufac.	Model	Serial #	Range	U _B	Units
41	PSIA	Viatran	274	215597	60	0.046	psi
42	PSID	Viatran	274	213205	40	0.033	psi
43	Temperature						°F
16	FX (Drag)	AMTI	ZMC5-6-10K-SSUDW	M3891	5000	8.0	lbf
17	FY (Lift)	AMTI			5000	7.6	lbf
18	FZ	AMTI			10000	58	lbf
19	MX (Roll)	AMTI			20000	33	in-lb
20	MY	AMTI			20000	85	in-lb
21	MZ (Pitch)	AMTI			10000	12	in-lb
6	Flowmeter	Hoffer Flow	HO2X2-5-275-T	95419	275		gpm
22	PU 5 psi	Sensotec	060-4624-01	481444	5	0.010	psi
24	PU 10 psi	Viatran	223	3680452	10	0.010	psi
25	PU 25 psi	Viatran	225	2844422	25	0.014	psi
26	PU 100 psi	Viatran	274	319800	100	0.029	psi
23	PL 5 psi	Sensotec	4624-01	560534	5	0.016	psi
27	PL 10 psi	Viatran	223	2844322	10	0.021	psi
28	PL 25 psi	Viatran	274	299284	25	0.017	psi
29	PL 100 psi	Viatran	274	319801	100	0.089	psi
4	RTD	Omega	RTD-NPT-72-E				°F
31	Kiel Probe	Viatran	274	216616	30	0.11	psi
32	DP 5 psi	Sensotec	P-30-P/4624-01	173152	5	0.012	psi
30	DP 10 psi	Viatran	223	9728068	10	0.016	psi
5	Motor	Reliance	SP600				V

Table 2. Completed Test Matrix of LDV Measurements

MEASUREMENT TYPE	SLOT FLOW CONDITION		ANGLE OF ATTACK	TUNNEL VELOCITY	CHORDWISE SURVEY	SPANWISE SURVEY
	C μ_u	C μ_L	(deg.)	U _{up} (m/s)	y/s	X/c
“Slight Flow” Upper Slot	0.07	0.0	0	3.0	-0.2, -0.6, -0.8, -0.9	1.083, 1.150, 1.215, 1.271
			10	3.0		1.083, 1.271
	0.05	0.0	20	3.0		1.083
“Moderate Flow” Upper Slot	0.13	0.0	0	3.0		1.083, 1.271
“Maximum Flow” Upper Slot	0.18	0.0	0, 10	3.0		1.083
“Assisted Lift” Flow	0.16	0.003	0	3.0	-0.2, -0.6, -0.8, -0.9	1.083, 1.271
			10	3.0		1.083

MEASUREMENT TYPE	FLOW CONDITION		ANGLE OF ATTACK	TUNNEL VELOCITY	SINGLE LINE SURVEYS	
	C μ_u	C μ_L	(deg)	U _{up} (m/s)	y/s	x/c
“No Slot Flow”	0.0	0.0	-0.6	7.67	-0.25, -0.5, -0.75	1.083
			0.0	7.35	-0.25, -0.5, -0.75	3.20
			0.0	3.04	-0.25, -0.5, -0.75	1.083, 1.271, 3.20
“Zero Drag”	0.009	0.009	0.0	7.44	-0.25, -0.5, -0.75	1.083
	0.010	0.010	0.0	7.35	-0.25, -0.5, -0.75	3.20
	0.013	0.013	0.0	3.04	-0.25, -0.5, -0.75	3.20
“Positive Thrust” Wake Filling	0.027	0.027	0.0	3.06	-0.5	1.083
	0.0297	0.0297	0.0	3.06	-0.25	1.020, 1.083, 1.271
					-0.5	1.083

Table 3. Optical Parameters for CCfoil Tests

DESIGNATOR		FIBER OPTIC PROBE			FOCUSING LENS		LDV PROBE VOLUME			CALIBRATION COEFFICIENTS	
Head ¹	Wavelength	Beam Diameter	Expansion Ratio	Beam Spacing	Focal Length	Beam Angle	Diameter	Length (H ₂ O)	Fringe Spacing	Slope	Intercept
#	λ (nm)	D_{e-2} (mm)	M	d_{LDV} (mm)	f_L (mm)	α (degrees)	d_M (mm)	l_M (mm)	d_f (μ m)	m	b (m/s)
1-1D	476.5	1.35	2.775	115	800	8.22	0.13	2.40	3.32	0.9951	0.0045
2-2D	488.0	4.1	1.5	112	1600	4.00	0.16	6.14	6.98	0.9783	0.0001
2-2D	514.5	4.1	1.5	112	1600	4.00	0.17	6.48	7.35	0.9916	0.0019

¹Head numbers, x – yD, nomenclature is as follows: x is the Fiber optic system (1 denotes 85 mm system, 2 denotes 112 mm system); y is the maximum number of beam pairs.

Table 4. Uncertainty Estimates of Elemental Variables

ELEMENT	U _B	U _A	TOTAL U	UNIT	DESCRIPTION
V ⁺	0.16 – 0.80	0.04 – 0.06	0.17 – 0.80	%	LDV velocity measurement
σ_x	-	3.9 – 5.1	3.9 – 5.1	%	Velocity measurement standard deviation
x	0.09	-	0.09	mm	Axial coordinate
y	3.2	-	3.2	mm	Transverse Coordinate
z	0.09	-	0.09	mm	Vertical Coordinate
s	0.39	-	0.39	mm	CCfoil Span
c	0.39	-	0.39	mm	CCfoil Cord at Root

⁺The listed uncertainties are for the velocity ranges reported in this report

Table 5. Uncertainty Estimates of CCfoil Test Parameters

ITEM	FUNCTION	U _B	U _A	TOTAL U	REFERENCE	DESCRIPTION
VR	$f(V)$	0.003 – 0.011	0.0006 – 0.027	0.003 – 0.029	-	All velocity ratios (e.g. U_x/U_m)
U_{up}	$f(V)$	0.002 – 0.008	0.0006	0.002 – 0.008	U_{up}	Model Reference Velocity
Tu	$f(V)$	0.002 – 0.008	0.039– 0.059	0.039 – 0.060	Tu	Relative Turbulence Intensity (e.g. u_x/U_m)
x/c	$f(C, d_m)$	0.0007	-	0.0007	-	Relative axial location
y/s	$f(S, l_m)$	0.0053	-	0.0053	-	Relative transverse location
z/c	$f(C, d_m)$	0.0007	-	0.0007	-	Relative vertical location

Table 6. Force Measurements Coincident with LDV Measurements

α (deg)	N	$C_{\mu U}$	$C_{\mu L}$	C_D	C_L	C_m	$Re/10^6$
-0.6	4	0	0	0.0167 ± 0.0002	-0.0048 ± 0.0058	-0.0029 ± 0.0018	5.4838 ± 0.0034
0	1	0	0	0.0183	0.0269	0.0061	2.1257
0	3	0	0	0.0165 ± 0.0008	0.0187 ± 0.0059	0.0024 ± 0.0017	2.1869 ± 0.0095
0	1	0	0	0.0192	0.0331	0.0033	2.1227
0	3	0	0	0.0182 ± 0.0003	0.0203 ± 0.0040	0.0036 ± 0.0012	5.1069 ± 0.0114
0	10	0.06969 ± 0.00013	0	0.4279 ± 0.0046	1.4084 ± 0.0056	-0.3017 ± 0.0012	2.1581 ± 0.0016
0	10	0.06997 ± 0.00016	0	0.4020 ± 0.0017	1.3804 ± 0.0034	-0.2960 ± 0.0007	2.1110 ± 0.0020
0	19	0.06969 ± 0.00017	0	0.3803 ± 0.0027	1.3601 ± 0.0052	-0.2932 ± 0.0008	2.1010 ± 0.0024
0	16	0.06980 ± 0.00009	0	0.3892 ± 0.0040	1.3653 ± 0.0070	-0.2928 ± 0.0015	2.1214 ± 0.0022
0	6	0.12980 ± 0.00022	0	0.7785 ± 0.0070	1.7400 ± 0.0084	-0.3331 ± 0.0060	2.1280 ± 0.0022
10	10	0.06983 ± 0.00033	0	0.6585 ± 0.0101	1.8392 ± 0.0115	-0.2113 ± 0.0024	2.0831 ± 0.0037
10	7	0.17143 ± 0.00093	0	1.1294 ± 0.0051	2.1255 ± 0.0151	-0.2477 ± 0.0065	2.0627 ± 0.0027
20	2	0.04932	0	0.7733	1.9974	-0.0809	2.0754
0	10	0.15255 ± 0.00421	0.00350 ± 0.00013	0.8702 ± 0.0365	1.9040 ± 0.0168	-0.3747 ± 0.0053	2.0860 ± 0.0065
0	12	0.15694 ± 0.00180	0.00355 ± 0.00002	0.7848 ± 0.0025	1.9046 ± 0.0054	-0.3993 ± 0.0015	2.0884 ± 0.0030
0	7	0.15912 ± 0.00014	0.00399 ± 0.00003	0.8036 ± 0.0028	1.9335 ± 0.0025	-0.4056 ± 0.0017	2.0768 ± 0.0043
0	5	0.00914 ± 0.00012	0.00926 ± 0.00013	0.0000 ± 0.0004	0.0100 ± 0.0028	0.0074 ± 0.0014	5.2681 ± 0.0024
0	5	0.00969 ± 0.00046	0.00980 ± 0.00044	0.0007 ± 0.0008	-0.0136 ± 0.0035	0.0131 ± 0.0022	5.1078 ± 0.0028
0	4	0.02823 ± 0.00241	0.02896 ± 0.00250	-0.0409 ± 0.0042	0.0216 ± 0.0051	0.0035 ± 0.0024	2.2159 ± 0.0030

References

- [1] Rogers, Ernest O. and Donnelly, Martin J., 2004. "Characteristics of a Dual-Slotted Circulation Control Wing of Low Aspect Ratio Intended for Naval Hydrodynamics Applications," AIAA Paper 2004-1244, American Institute of Aeronautics and Astronautics 42nd Aerospace Sciences Meeting, Reno, NV.
- [2] Duvvuri, Tirumalesa and Park, Joel T., 1975. "Analysis of Coanda Reattachment on Curved Surfaces," ARL TR 75-0101, Technical Report, Aerospace Research Laboratories, Wright-Patterson Air Force Base, OH.
- [3] Englar, Robert J. and Applegate, Constance A., 1983. "Circulation Control – Bibliography DTNSRDC Research and Outside Selected References (January 1969 through December 1983)," David Taylor Naval Ship and Development Center, Bethesda, MD.
- [4] Chang, Peter A.; Slomski, Joseph; Marino, Thomas; and Ebert, Michael P., 2005. "Numerical Simulation of Two- and Three-Dimensional Circulation Control Problems," AIAA Paper 2005-0080, American Institute of Aeronautics and Astronautics 43rd Aerospace Sciences Meeting, Reno, Nevada.
- [5] Park, Joel T.; Cutbirth, J. Michael; and Brewer, Wesley H., 2002. "Hydrodynamic Performance of the Large Cavitation Channel (LCC)," NSWCCD-50-TR—2002/068, Technical Report, Naval Surface Warfare Center Carderock Division, West Bethesda, MD.
- [6] Park, Joel T.; Cutbirth, J. Michael; and Brewer, Wesley H., 2005. "Experimental Methods for Characterization of a Very Large Water Tunnel," *Journal of Fluids Engineering*, Vol. 127, No. 6, pp. 1210-1214.
- [7] Laws, E. M. and Livesey, J. L., 1978. "Flow Through Screens," *Annual Review of Fluid Mechanics*, Vol 10, pp. 247-266, Palo Alto, California, Annual Reviews, Inc.
- [8] Guide to the Expression of Uncertainty in Measurement, 1995. International Organization for Standardization (ISO), Geneva, Switzerland.
- [9] Baker, Roger C., 2000. *Flow Measurement Handbook*, Cambridge, Cambridge University Press.
- [10] ASTM E74-02, 2002, "Standard Practice of Calibration of Force-Measuring Instruments for Verifying the Force Indication of Testing Machines," American Society for Testing and Materials, West Conshohocken, PA.
- [11] Coleman, H. W. and Steele, W. G., 1999. *Experimentation and Uncertainty Analysis for Engineers*, Second Edition, New York, John Wiley & Sons.
- [12] Scheffe, H., 1973. "A Statistical Theory of Calibration," *The Annals of Statistics*, Vol. 1, No. 1, pp. 1-37.
- [13] Carroll, R. J., Spiegelman, C. H., and Sacks, J., 1988. "A Quick and Easy Multiple-Use Calibration-Curve Procedure," *Technometrics*, Vol. 30, No. 2, pp. 137-141.

Distribution

	<i>Copies</i>		<i>Copies</i>
Dr. J. Michael Cutbirth xxxxx Melbourne, FL USA	3	NSWC, CARDEROCK DIVISION INTERNAL DISTRIBUTION	
		Code Name	
Mr. Ernest O. Rogers 12131 Holly Knoll Circle Great Falls, VA 22066-1227 USA	3	5000 I. Y. Koh	1
		5010 w/o enclosure	1
		5060 D. A. Walden	1
Dr. Ron Joslin Office of Naval Research 875 North Randolph Street Arlington, VA 22203-1995 USA	3	5080 J. F. Brown	1
		5100 M. J. Davis	1
		5102 D. M. Foster	1
		5200 W. G. Day, Jr.	1
		5300 J. W. Johnston	1
Dr. Ki-Han Kim Office of Naval Research 875 North Randolph Street Arlington, VA 22203-1995 USA	3	5400 P. A. Chang	1
		M. J. Donnelly	3
		M. P. Ebert	1
		R. J. Etter	1
		J. J. Gorski	1
Dr. L. Patrick Purtell Office of Naval Research 875 North Randolph Street Arlington, VA 22203-1995 USA	3	S. D. Jessup	3
		T. A. Marino	1
		J. R. Slomski	1
		R. P. Szwerc	1
		5500 T. R. Applebee	1
DTIC	1	J. T. Park	3
		5600 E. S. Ammeen	1
		Library	2

